2-1-2003

Scattering of ultra wide band X-wave pulses by a sphere

Maged Fayez Moawad
The American University in Cairo AUC

Recommended Citation

APA Citation
Moawad, M. (2003).*Scattering of ultra wide band X-wave pulses by a sphere* [Thesis, the American University in Cairo]. AUC Knowledge Fountain.
https://fount.aucegypt.edu/retro_etds/1643
MLA Citation
Moawad, Maged Fayez. *Scattering of ultra wide band X-wave pulses by a sphere*. 2003. American University in Cairo, Thesis. *AUC Knowledge Fountain*.
https://fount.aucegypt.edu/retro_etds/1643

The American University in Cairo

SCHOOL OF SCIENCES AND ENGINEERING

SCATTERING OF ULTRA WIDE BAND X-WAVE

PULSES BY A SPHERE

A Thesis Submitted to

Department of Physics

in partial fulfillment of the requirements for

THE DEGREE OF MASTER OF SCIENCE

BY

MAGED FAYEZ ZAKI MOAWAD

BACHELOR OF SCIENCE IN PHYSICS

(Under the Supervision of Dr. Amr Shaarawi)

SEPTEMBER, 2002

i

The American University in Cairo

Scattering of Ultra-Wideband X-Wave Pulses

by a Sphere

by

Maged Fayez Zaki Moawad

A Thesis Submitted to Department of Physics

September, 2002

in partial fulfillment of the requirements for
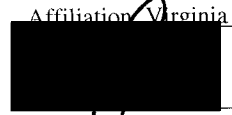
The degree of Master of Science

has been approved by

Dr. Amr M. Shaarawi

Thesis Committee Chair / Adviser

Affiliation: The American University in Cairo

Dr. Ashraf H. Elfiqi

Thesis Committee Reader / Examiner

Affiliation: The American University in Cairo

Dr. Sedki M. Riad

Thesis Committee Reader / Examiner

Affiliation: Virginia Polytechnic Institute and State University

Department Chair   Date   Dean   Date

Program Director

Scattering of Ultra Wide Band X-Wave Pulses
by a Sphere

by

Maged Fayez Zaki Moawad

A THESIS SUBMITTED TO DEPARTMENT OF PHYSICS

September, 2002
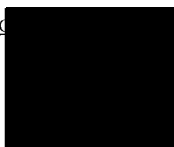
ABSTRACT

In this thesis, a study of the scattering of ultra-wideband X-wave pulses by a sphere is provided. We start by considering the scattering of acoustic X-wave pulses by a rigid sphere and exame the effect of different parameters on the backscattered spectrum. Moreover, we show how to determine the sphere size from the spectrum of the backscattered signal and demonstrate that this approach is useful for the scattered fields due to both on-center and off-center incidences. Then we extend our study to include the scattering of acoustic X-wave pulses by a soft sphere and show that we can identify the size and material of the sphere from the backscattered spectrum. As a result, we outline a procedure by which we can characterize and identify unknown spheres from their backscatterd spectra. Finally, we use a Mie series approach to establish the tranverse electric electromagnetic X-wave scattered fields by a perfectly conducting sphere.

TABLE OF CONTENTS

FIGURES

TABLES

CHAPTER 1

INTRODUCTION

Localized waves are one class of ultra-wideband pulses that attracted considerable attention in the past twenty years. The first localized wave to appear in literature was known as the Focus Wave Mode (FWM) and it was introduced by Brittingham in 1983 when he suggested a mathematical non-separable electromagnetic solution to the homogeneous Maxwell's equations [1]. FWM had a three-dimensional pulse structure that propagates with the velocity of light in straight line, and it was shown to be continuous, nonsingular and nondispersive for all time. Nevertheless, this solution was found to have infinite energy content [2,3]. Because of the pioneering work of Brittingham, researchers began to look for other slow decaying solutions. Examples of such solutions include: Wu's electromagnetic missiles [4-15], Durnin's Bessel Beams [16-18], Moses and Prosser's electromagnetic bullets [19-22], Ziolkowski's directed energy pulse trains (DEPTs) [23-25], Heyman and Felsen's pulsed beams [26-31], Overfelt's Bessel-Gauss pulses [32,33], Lu and Greenleaf's X-waves and Saari's Bessel X-pulses [34-36]. In order to understand the unusual decay properties of Brittingham's solution, Sezginer [37], Ziolkowski [38], and Belanger [39,40] explained that FWM could be represented by a product of an envelope function and an exponential modulation moving in opposite directions. Moreover, it was verified that the envelope function could be denoted by a solution to a complex parabolic Schrödinger like equation. Sezginer [37] and Belanger [39] proved also that FWM

1

solution could be represented in terms of Gaussian-Laguerre and Gaussian-Hermite packet like solutions. Likewise, solutions to the homogeneous spinor wave equation and the massless Dirac equation were discovered by Hillion [41,42] using Brittingham's modes.

To obtain finite energy localized waves, one can use a superposition of the source free solutions, or otherwise use the infinite energy source free solutions as excitations to finite size sources. The first approach was used by Ziolkowski who argued that finite energy localized wave (LW) solutions could be obtained as a superposition of FWMs [38], and he called these solutions " Directed Energy Pulse Trains" DEPT [24,25]. The splash and Modified Power Spectrum (MPS) pulses are two examples of DEPTs. Ziolkowski claimed that FWM could offer more suitable basis for the synthesis of ultra-short time-limited pulses than the usual time-harmonic plane waves and studied both acoustical as well as electromagnetic MPS pulses. He suggested that finite energy MPS pulses could be reproduced using a source consisting of a finite planar array of dipoles [23-25,38]. To establish the feasibility of the generation of these LW pulses, Ziolkowski *et al.* [43,44] carried out an experiment demonstrating the possibility of launching acoustical DEPT in a water tank. They used a linear array of acoustical source elements driven by independent generators. The second approach uses the infinite-energy LW solution to excite an aperture of a finite size. Shaarawi *et al.* [45-51] suggested that a Gaussian dynamic aperture could be used to produce a good approximation to the source-free FWM solution. Detailed investigations of the decay patterns of several LW pulses produced by finite time dynamic apertures illustrated that their spectral decay patterns are completely different from those of

2

quasi-monochromatic signals, as well as other broadband pulses [47-51]. These investigations demonstrated that large dynamic apertures could produce narrow pulses capable of traveling long distances with minimal decay [46-50]. It has also been shown that the slow decay is due to the fact that the spectral depletion of LW pulses is different from that of CWs. In applications that need continuous variable adjustments of the field depth and beam waist, one could control the temporal focusing by changing the time evolution of the waveforms exciting the various parts of the aperture plane. By comparing the temporal and spatial focusing, it was found that the former depends on the initial excitations of the various elements of the source while the latter results from the geometrical shape of the source. As such, temporal focusing is advantageous if the range and width of the focused field vary frequently.

Because LWs were characterized by a highly focused depth, and an ultra-wide bandwidth, it was essential to develop new means to assess their propagation characteristics. Traditionally, Rayleigh length, which is the carrier frequency multiplied by the square of the width of the aperture, was used to measure the bandwidth of a quasi-monochromatic signal that is generated by a finite aperture. This method could no be applied to LWs since they do not have fixed carrier frequency [23-25]; thus Ziolkowski suggested new methods to measure the decay patterns of the LWs, and he pointed out that the characteristics of LWs, unlike the quasi monochromatic continuous waves (CW), depends on the type of transmitter-receiver system [23-25]. Ziolkowski considered the problem of electromagnetic pulses generated by an array of electrically short and thin, center-fed, linear dipole antennas. By measuring the radiated field in the far field [23,25] it was shown that a new type of

array was required to generate such LW pulses; particularly, one that had independent elements each excited by a specific broadband time-dependent signal. Afterward it was verified that by manipulating the driving function of the source elements of an array, a specific field representation at some predefined point in space could be established [52].

Brittingham's FWM solution can be perceived as a weighted superposition over Bessel beams. Durnin [16-18] introduced the diffraction-free "Bessel beams" that are excited from an infinite aperture. In contrast, with FWM pulses, an aperture used to generate Bessel beam pulses require infinite power. To obtain a finite-size source, Durnin [17,53-56] recommended cutting off the Bessel beam at a certain radial distance on the generating aperture. Subsequently, he compared the finite Bessel beams with the Gaussian beams and demonstrated that although both have central spots with equal radii, the former had larger field depth. Durnin *et al.* verified that the differences in energy distribution over similar apertures increase the depth of the generated beam on the expense of the power used. The spectral structure of FWM-like pulses shows explicitly that they are weighted superpositions of Bessel beams. However, one should always recall that the former are ultra-wideband pulses while the latter are monochromatic fields.

In spite of the different nature of Bessel beams and LWs, some methods for generating Bessel beams provide clues to the development of optical sources for LW pulses. Several experiments were done to develop optical sources of Bessel beams depending on the fact that an annular ring is a zero-order Bessel function. For

4

example, Durnin excited an annular slit placed in the focal plane of a lens. Another way was illuminating a point source of a Fabry-Perot interferometer and using a lens behind the interferometer with an aperture that was designed to allow the Passage of the ring only [57,58]. A further experiment was done by Armito *et al.* and Vahimaa *et al.* [59,60] in which they generated Bessel beams using a refractive axicon. Alternative approaches for the production of Bessel beams employed holographic techniques to construct diffractive axicons [61-63]. The acoustical Bessel beam generator was invented by Hsu *et al.* [64] by using a three-ring narrow-band solid piezoelectric (PZT) transducer to generate CW Bessel beams. Later, Lu and Greenleaf, who considered the use of ultrasonic Bessel beams in medical imaging applications, developed an improved acoustical transducer [65]. By comparing the diameter of the Gaussian beam with that of a Bessel beam outside the depth of the focal field, it was found that the former is larger. Consequently, Lu and Greenleaf illustrated that Bessel transducers would have better resolution power and focusing capabilities than traditional ultrasonic scanners and imaging instruments due to their large field depths and small widths of the center lobes.

In 1992, Lu and Greenleaf [66,67] introduced a second class of non-diffracting pulsed wave fields that are axially symmetric exact solutions for the scalar wave equation. This new class was called X-waves because of geometrical shape of their field distribution in a plane along their propagation axis, and they can travel in free space to infinite distances without diffraction if they are generated by an infinite aperture. Their space-time structure consists of a highly focused central part with the maximum amplitude surrounded by an extended lower intensity background field [68]. When X-

5

waves are generated from a finite aperture, they are usually referred to as "limited diffraction pulses". Lu and Greenleaf were able to develop an ultrasonic transducer consisting of multiple broadband circular piezoelectric PZT rings excited with distinct time-dependent waveforms in order to emit acoustical X-waves [65-67].

The extended focus depth of the X-wave makes them suitable for applications involving high resolution imaging, and detection of buried objects at varying depths [69]. Because they do not need continuous refocusing at different depths, the use of X-waves increases the repetition rate of the sent pulses in any practical imaging or detection scheme. This property together with adequate focusing of the incident pulse increases the level of the backscattered signals. Along such vein, Lu and Greenleaf studied analytically and experimentally the use of X-waves in pulse-echo imaging [70], and they compared the pros and cons of X-waves and Bessel beams as opposed to the traditional focused beams used in biomedical ultrasonic imaging [71].

Lu [72] studied the design and generation of Bowtie beams that are higher order derivatives of the X-wave with respect to one of its transverse spatial variables. He developed a synthetic array design that eliminated the cross talk between all elements because the side lobes are dramatically decreased. Besides, this design provided high flexibility because the size of the elements and the inter-element spacing can be easily changed. Lu et al. established a new approach for synthesizing LWs through utilizing X-waves of varying orders as transformation basis, and called it X-transform. In addition, similar to Hermandz et al. [52], Lu applied a least square method to design limited diffraction beams from Bessel beams and X-waves [73].

6

Most of the work done on the generation of LW pulses used acoustical techniques. For example, the experiments that were performed by Lu and Greenleaf were done on ultrasonic X-wave sources. Similarly, Ziolkowski *et al.* [43,44], and Power *et al.* [74] used linear acoustical array in their work. On the other hand, there were few attempts to generate optical LW pulses [34-36]. The approach used in these attempts uses pulsed illuminations of axicons or annular slits. As for microwave sources, the need for ultra-fast independent excitations of the aperture elements makes it hard to achieve sources. However, Mugani *et al.* used an approach analogous to the optical methods [75]. They illuminated an annular slit placed infront of a circular feed horn using a microwave pulse. The radiated field was then focused by a spherical reflector to form an X-wave pulse along the axis of the source [75].

It has been established that broadband pulses have appealing properties in relation to applications such as Impulse Radar (IR) and Ground Penetrating Radar (GPR) systems. This growing relevance is due to the high efficiency of broadband pulses in detecting and identifying objects. As discussed before, Lu and Greenleaf demonstrated that acoustic waves have higher resolution capabilities than typical systems used for pulse-echo imaging and tissue characterization. The close resemblance in the functions of GPR systems and those used for ultrasonic medical imaging urges us to investigate the capabilities of LW pulses in applications involving the detection and identification of scattering objects. Power *et al.* demonstrated the capability of using back scattered MPS pulses from an object to determine its size [74]. In addition, LW pulses do not need to be refocused several times at different

7

depths when used for detecting buried objects. Furthermore, they are be generated from very large apertures in spite of being very narrow pulses. Since the waist of the generated pulse can be controlled by the temporal excitation of the source elements, wide LW pulses can be initially generated with in order to scan and find buried objects buried in the ground. Once an object is found a narrower pulse would be generated to identify the size, material and location of the scattering object. To develop such a system one has to be able to design an adequate source and, as discussed earlier, this path has been studied thoroughly. Furthermore, one has to study the propagation of LW pulses through surfaces of discontinuity and in different types of media [69,76-79]. Finally, comprehensive investigations of the scattering of LW pulses from various objects are necessary. In a recent study, the scattering of X-waves from a circular disk has been carried out using a high frequency approach [69]. A method employing correlation measurements of the back-scattered signals taken from four detectors demonstrates a significant improvement in resolution over typical arrangements [69].

In the present work, we shall study the scattering of ultra-wideband X-waves by a sphere. In Chapter 2, we review some of the properties of the acoustic X-wave. Subsequently, we derive a series solution for the scattered X-wave field. This is done for an X-wave incident with it peak passing through the center of the sphere and off-center. We shall consider the scattered spectrum for different angles starting from the backscattering angle $\theta = \pi$, to the forward scattering angle $\theta = 0$ in multiples of $(\pi/6)$. Then we shall study the effect of different parameters, characterizing the incident pulse and the scatterer, on the backscattered spectrum. These parameters are

8

the focused pulse width and frequency bandwidth, the spectral apex angle, and the radius of the scattering sphere. We shall demonstrate how we can extract the sphere size, using simulations of the backscattered spectra of spheres with different radii. Finally, we shall demonstrate that, even if the pulse is incident off center, one can obtain decent estimates for the radii of the scattering spheres.

In Chapter 3, we include the scattering of acoustic X-waves by soft spheres. Again we shall derive expressions for the scattered fields due to both on-center and off-center incidence. The deduced expressions are different from those of the rigid sphere, but reduce to the rigid sphere case when the product of the density of the material and the speed of propagation inside the sphere is much larger than the product of those of the surrounding medium. We shall also investigate the effect of varying the scattering angle on the spectrum of the scattered pulses. Then, we shall test the effect of changing the surrounding medium, radius of the sphere, density of the sphere, and the speed of wave propagation inside it. In addition, we shall illustrate how we can determine the radius of the sphere, as well as, the speed of wave propagation inside it from the back-scattered spectrum. This means that from the frequency content of the backscattered signal, one can determine both the size and the material of the scatterer. We shall demonstrate that the accuracy of our results is still acceptable even for the case of off-center incidence.

In Chapter 4, we derive expressions for the scattered field due to an incident electromagnetic X-wave on a perfectly conducting sphere. The aim of this chapter is to describe an approach for deducing a X-wave scattered fields using a Mie series

9

approach [80,81]. The extension of this approach to the case of a dielectric sphere is straightforward. The solutions obtained for the scattered electromagnetic pulses can then be used to characterize the size and the material of the scattering object. The details of this effort will be deferred to later work. In Chapter 5, concluding remarks on this work are provided and future developments are discussed.

CHAPTER 2

SCATTERING OF ACOUSTIC X-WAVES BY RIGID SPHERE

2.1 INTRODUCTION

The scattering of acoustic ultra-wideband pulses from spheres has important applications in fields such as high-resolution imaging, remote sensing, material characterization, and detection of buried objects. Localized waves are one class of ultra-wideband pulses that have distinct advantages when it comes to situations involving the detection of buried objects [69]. Studies along these lines dealt with the scattering of X-waves from a circular disc placed in free space and buried in the ground [69]. The analysis used in this investigation was based on the high frequency techniques in combination with the pulsed plane wave representation of the X-wave solution [77]. In spite of the effectiveness of the methods used in the aforementioned study, it has not been directed towards the possibility of using the scattered signal to identify or characterize the scattering object. An important study of the possibility of using LWs for identification purposes has been undertaken by Power *et al.* [74], where they demonstrated the possibility of identifying the radii of various spheres from the spectrum of the backscattered signal due to an incident MPS pulse. Their analysis considered both the case of hard and soft spheres, although the method they employed was applicable only to the identification of the radii of hard spheres, and could not be used to find the speed or the density of the scattering material.

Furthermore, they demonstrated experimentally the effectiveness of their identification technique.

The objective of this chapter is to study the scattering of an acoustic X-wave (AXW) by a rigid sphere. We start by providing expressions for the incident AXW field, and use such expressions to calculate the scattered AXW field. We follow essentially the analysis employed by Power *et al.* to calculate the scattered field due to an AXW incident on the center of the sphere. We extend the analysis to the case when the axis of propagation of the incident AXW field is off-center. In such a case, one can consider the two situations when the focused region of the AXW field is off-center but hits the body of the sphere or passes outside the sphere. Our main objective in this chapter is to provide a thorough investigation of the effects of changing the AXW pulse width and axicon angle, the scattering angle and the radius of the scattering sphere, as well as, the distance of the observation point from the sphere. Following a technique similar to that used by Power *et al.*, we show how to extract information regarding the sphere size from the backscattered spectrum. The usefulness of this approach is demonstrated for the scattered fields due to both on-center and off-center incidences.

2.2 SOURCE FREE AXW SOLUTION

A spectral approach will be used to obtain the scattered field due to an incident AXW. Thus, it is important to be able to choose the spectral representation most suitable to the adopted analysis. As mentioned earlier, the AXW can be represented as a Fourier superposition over plane waves having their wave vectors forming a conic surface as

shown in Fig. (2.1). The series solution of a plane wave scattered from a sphere [82] can then be integrated over the Fourier spectrum of the X-wave solution to obtain the AXW scattered field. To determine the AXW Fourier representation consider the 3-D scalar wave equation

$$\left(\nabla^2 - \frac{1}{c^2}\frac{\partial^2}{\partial t^2}\right)\Psi(r,t) = 0. \tag{2.2.1}$$

The AXW solution can be represented as the Fourier superposition

$$\Psi^i_{AXW}(r,t) = \int_{R^3} d^3k \int_0^\infty d(\omega/c) e^{-ik\cdot r} e^{i\omega t} \hat{\psi}(k,\omega)\delta(\omega - |k|c), \tag{2.2.2}$$

where the AXW spectrum has the following [76]

$$\hat{\psi}(k,\omega) = e^{-(\omega/c)a}\frac{2\pi}{\sin\xi}k^{q-2}\delta(\theta_k - \xi) \tag{2.2.3}$$

and $k = \sqrt{\left(k_x^2 + k_y^2 + k_z^2\right)}$. The parameter ξ defines the apex angle of the spectral cone shown in Fig. (2.1) and is usually referred to as the axicon angle. The constant a determines the frequency bandwidth of the AXW field, as well as the width of its focused region [69,83]. Fig. (2.2) shows how the lateral and axial widths of the X-wave pulse are determined from the two parameters a and ξ.

The Substitution of $\hat{\psi}(k,\omega)$ in Eq. (2.2.2) gives

$$\Psi^i_{AXW}(r,\theta,\phi,t) = \int_0^\infty dk \int_0^\pi d\theta_k \int_0^{2\pi} d\phi_k k^2 \sin\theta_k \frac{2\pi}{\sin\xi}k^{q-2}\delta(\theta_k - \xi)e^{-ka}e^{-ik\cdot r}e^{ikct}. \tag{2.2.4}$$

13

The spatial part of this plane-waves superposition depends on $k \cdot r$, which can be expressed as

$$
\begin{aligned}
k \cdot r &= k_x x + k_y y + k_z z \\
&= kr \left(\sin \theta_k \cos \phi_k \sin \theta \cos \phi + \sin \theta_k \sin \phi_k \sin \theta \sin \phi + \cos \theta_k \cos \theta \right) \\
&= kr \left(\cos \theta_k \cos \theta + \sin \theta_k \sin \theta \cos(\phi_k - \phi) \right).
\end{aligned}
$$

The spectrum given in Eq. (2.2.3) restricts θ_k to the value $\theta_k = \xi$. Consequently, we can define the angle γ_k as follows:

$$
\cos \gamma_k = \cos \theta_k \cos \xi + \sin \theta_k \sin \xi \cos(\phi_k - \phi). \tag{2.2.5}
$$

Thus, it follows that

$$
k \cdot r = kr \cos \gamma_k . \tag{2.2.6}
$$

Using Eqs. (2.2.6) and (2.2.5) in Eq. (2.2.4) and performing the integration over θ_k, we obtain

$$
\Psi_{AXW}^i (r, \theta, \phi, t) = \int_0^\infty dk \int_0^{2\pi} d\phi_k k^q \sin \xi \frac{2\pi}{\sin \xi} e^{-ka} e^{ikct} e^{-ikr(\cos\theta\cos\xi + \sin\theta\sin\xi\cos(\phi_k - \phi))} .
$$

Rearranging terms, the expression for the incident wave becomes

$$
\Psi_{AXW}^i (r, \theta, \phi, t) = \int_0^\infty dk \int_0^{2\pi} d\phi_k k^q e^{-ka} e^{-ikr(\cos\theta\cos\xi + \sin\theta\sin\xi\cos(\phi_k - \phi))} e^{ikct} . \tag{2.2.7}
$$

Let $x = kr \sin \theta \sin \xi$, and using the definition of the zeroth order Bessel function [84]

$$
J_0(x) = \frac{1}{2\pi} \int_0^{2\pi} d\phi_k e^{-ix\cos(\phi_k - \phi)} \tag{2.2.8}
$$

the incident AXW pulse can be written as

14

$$\Psi_{AXW}^{i}(\rho,z,t) = 2\pi \int_{0}^{\infty} dk\, k^{q} J_{0}\left(kr\sin\theta\sin\xi\right) e^{-k[a+i(r\cos\theta\cos\xi - ct)]}$$

$$= 2\pi \int_{0}^{\infty} dk\, k^{q} J_{0}\left(k\rho\sin\xi\right) e^{-k[a+i(z\cos\xi - ct)]}. \tag{2.2.9}$$

The integration over k yields [85]

$$\Psi_{AXW}^{i} = 2\pi \frac{\partial^{q}}{\partial a^{q}} \left[\rho^{2}\sin^{2}\xi + \left(a + i(z\cos\xi - ct)\right)^{2}\right]^{-1/2}. \tag{2.2.10}$$

The order of the derivative with respect to q determines the order of the X-wave. A 3-D plot of this field is provided in Fig. (2.3) for $q = 0$, $a = 1\,\mu\mathrm{m}$ and $\xi = 2$. The lateral and axial waists of the highly focused central part of the AXW field depend on the values of the parameters a and ξ, as illustrated in Fig. (2.2).

2.3 SCATTERED AXW FIELD DUE TO ON-CENTER INCIDENCE

To calculate the scattered AXW pulse, we shall consider a general expression for a plane wave incident in a direction specified by a propagation vector k whose direction is defined by the angular variables θ_{k} and ϕ_{k}. Assuming a harmonic time dependence of the form $\exp(i\omega t)$, the spatial part of the plane wave solution

$$\Phi^{i}(r,\phi,\theta) = e^{-ik\cdot r} = e^{-ikr\cos\gamma} \tag{2.3.1}$$

represents the velocity potential of an acoustic field. Here, γ is the angle between $k \equiv (k,\theta_{k},\phi_{k})$ and $r \equiv (r,\theta,\phi)$. The specific choice $\theta_{k} = \xi$ yields $\gamma = \gamma_{k}$ as defined in Eq. (2.2.5).

15

Following the standard series solution technique used in calculating the scattering of plane waves from spheres, the incident plane wave is expanded in terms of Legendre Polynomials and spherical Bessel functions, viz. [84],

$$e^{-ikr\cos\gamma_k} = \sum_{n=0}^{\infty} a_n P_n(\cos\gamma_k) j_n(kr). \tag{2.3.2}$$

The θ, ξ and $(\phi - \phi_k)$ dependences in the argument of the function $P_n(\cos\gamma_k)$ can be separated according to the following expression:

$$P_n(\cos\gamma_k) = \sum_{m=0}^{n} \varepsilon_m \frac{(n-m)!}{(n+m)!} P_n^m(\cos\theta) P_n^m(\cos\xi) \cos(m(\phi_k - \phi)), \tag{2.3.3}$$

where $\varepsilon_m = 1$ for $m = 0$, and $\varepsilon_m = 2$ for $m \neq 0$.

The coefficient a_n in Eq. (2.3.2) can be determined using the orthogonality relation of the Legendre Polynomials as follows:

$$\int_0^\pi e^{(-ikr\cos\gamma_k)} P_m(\cos\gamma_k) \sin\gamma_k d\gamma_k = \int_0^\pi \left(\sum_{n=0}^{\infty} a_n j_n(kr) P_n(\cos\gamma_k) P_m(\cos\gamma_k) \sin\gamma_k \right) d\gamma_k .$$

The orthogonality condition of the Legendre Polynomials yields [84]

$$\int_0^\pi e^{(-ikr\cos\gamma_k)} P_m(\cos\gamma_k) \sin\gamma_k d\gamma_k = \frac{2a_m}{2m+1} j_m(kr). \tag{2.3.4}$$

The integration on the left hand side of Eq. (2.3.4) gives

$$\int_0^\pi e^{(-ikr\cos\gamma_k)} P_m(\cos\gamma_k) \sin\gamma_k d\gamma_k = 2(-i)^m j_m(kr) \tag{2.3.5}$$

From Eqs. (2.3.4) and (2.3.5), we obtain

16

$$a_m = (-i)^m (2m+1).$$

(2.3.6)

The incident plane wave can thus be represented as a summation over functions of the spherical coordinate variables (r,θ,ϕ); specifically,

$$\Phi^i(r,\theta,\phi) = e^{-ikr\cos\gamma_k} = \sum_{n=0}^{\infty} (-i)^n (2n+1) P_n(\cos\gamma_k) j_n(kr).$$

(2.3.7)

The scattered field is usually represented as a series of concentric spherical waves diverging from the scatterer via the following mathematical expression:

$$\Phi^s(r,\theta,\phi) = \sum_{n=0}^{\infty} A_n P_n(\cos\gamma_k) h_n^{(2)}(kr).$$

(2.3.8)

Here, the spherical Bessel functions appearing in the expression for the incident plane wave has been replaced by the spherical Hankel functions. The parameter A_n is determined from the boundary conditions.

To find the expression for the scattered AXW pulse due to incidence on the center of the sphere, we integrate the scattered field due to an incident plane wave over the spectrum of the AXW field given in equation (2.2.3), viz.,

$$\Psi_{AXW}^s = \int_0^{\infty} dk \int_0^{\pi} d\theta_k \int_0^{2\pi} d\phi_k k^2 \sin\theta_k \frac{2\pi}{\sin\xi} k^{q-2} \delta(\theta_k - \xi) e^{-ka} e^{ikct}$$

$$\times \sum_{n=0}^{\infty} A_n h_n^{(2)}(kr) P_n(\cos\gamma).$$

(2.3.9)

The integration over θ_k gives

17

$$\Psi^s_{AXW} = \int\limits_0^\infty dk \int\limits_0^\pi d\Theta_k \int\limits_0^{2\pi} d\phi_k \, 2\pi k^q e^{-ka} e^{ikct} \sum_{n=0}^\infty A_n h_n^{(2)}(kr) P_n(\cos\gamma_k).$$

Using Eq. (2.3.3), the above expression can be written as

$$\Psi^s_{AXW}(r,\theta,\phi,t) = \int\limits_0^\infty dk \int\limits_0^{2\pi} d\phi_k \, 2\pi k^q e^{-ka} e^{ikct} \sum_{n=0}^\infty A_n h_n^{(2)}(kr) \sum_{m=0}^n \varepsilon_m \frac{(n-m)!}{(n+m)!}$$
$$\times P_n^m(\cos\theta) P_n^m(\cos\xi) \cos(m(\phi_k - \phi)). \qquad (2.3.10)$$

The integration over ϕ_k yields zero contributions to all terms having $m \neq 0$. Therefore, the scattered AXW reduces to

$$\Psi^s_{AXW}(r,\theta,\phi,t) = (2\pi)^2 \int\limits_0^\infty dk \, k^q e^{-ka} e^{ikct} \sum_{n=0}^\infty A_n h_n^{(2)}(kr) P_n(\cos\theta) P_n(\cos\xi). \qquad (2.3.11)$$

In order to determine the coefficient A_n, the appropriate boundary condition should be applied. For a rigid sphere, the incident and scattered fields should satisfy the condition that at the surface the gradient of the velocity potential should be continuous. Specifically,

$$\frac{\partial\Phi^i}{\partial r} + \frac{\partial\Phi^s}{\partial r} = 0 \text{ at } r = R. \qquad (2.3.12)$$

At this point one should realize that the pressure amplitude is related to the potential Φ through the relationship $P(\vec{r},t) = -\rho_0(\partial\Phi/\partial t)$, where ρ_0 is the density of the medium surrounding the sphere.

Differentiating Eqs. (2.3.7) and (2.3.8) with respect to the radial position and substituting with $r = R$, we obtain

18

$$(-i)^n (2n+1) P_n(\cos \gamma_k) k j_n'(kR) = -A_n k h_n^{(2)'}(kR) P_n(\cos \gamma_k)$$

Therefore, A_n acquires the following form:

$$A_n = -(-i)^n (2n+1) \frac{j_n'(kR)}{h_n^{(2)'}(kR)} \tag{2.3.13}$$

Substituting Eq. (2.3.13) back in Eq. (2.3.8), we obtain the following scattered potential:

$$\Phi^s(r,\theta,\phi) = -(-i)^n (2n+1) \frac{j_n'(kR)}{h_n^{(2)'}(kR)} h_n^{(2)}(kr) P_n(\cos \gamma_k). \tag{2.3.14}$$

Consequently, the expression for the scattered AXW pulse due to on-center incidence becomes

$$\Psi_{AXW}^s(r,\theta,\phi,t) = (2\pi)^2 \int_0^\infty dk k^q e^{-ka} e^{ikct} \sum_{n=0}^\infty -(-i)^n (2n+1) \frac{j_n'(kR)}{h_n^{(2)'}(kR)} h_n^{(2)}(kr)$$
$$\times P_n(\cos \theta) P_n(\cos \xi). \tag{2.3.15}$$

This expression can be used to calculate the scattered AXW field in configuration space in various directions specified by the angle θ. In later sections, we demonstrate how the information included in the spectrum of the scattered AXW field can be used to determine the radii of various spherical scatterers. This type of information is extracted from a study of several numerical examples illustrating the changes of the shape of the scattered spectrum due to the variation of the values of the parameter a, the axicon angle ξ and the radius of the sphere R. In addition, a study of the alterations in the spectrum of the scattered field with the different observation points (r,θ) is also undertaken. Before such a goal is fulfilled, we calculate the AXW field scattered due to an AXW pulse incident with its axis of propagation shifted away

19

from the center of the sphere. This calculation is important for determining the reliability of the suggested technique when the incident AXW pulse is not passing right though the center of the scattering sphere.

2.4 SCATTERED AXW FIELD DUE TO OFF-CENTER INCIDENCE

An X-wave moving in the z-direction with its axis of propagation shifted to a line parallel to the z-axis and passing through $x = x_0$ can be represented in terms of the following superposition:

$$\Psi_{AXW}^{i}(\vec{r},t) = \int_{R^3} d^3\vec{k} \int_0^\infty d(\omega/c) e^{-i(k_x(x-x_0)+k_y y+k_z z)} e^{i\omega t} \hat{\psi}(\vec{k},\omega) \delta(\omega - |\vec{k}|c), \tag{2.4.1}$$

where $\hat{\psi}(\vec{k},\omega)$ is given in Eq. (2.2.3). The incident pulse can be perceived as a superposition over plane waves having the following spatial dependence:

$$\begin{aligned}
\Phi^i(\vec{r},t) &= \hat{\psi} e^{-i(k_x(x-x_0)+k_y y+k_z z)} e^{i\omega t} \\
&= \hat{\psi} e^{ikx_0 \cos\phi_k \sin\theta_k} e^{-ikr\cos\gamma} e^{i\omega t}.
\end{aligned} \tag{2.4.2}$$

Using the same procedure described for the case of the on-center incidence, we can write the scattered field as

$$\Phi^s(\vec{r},t) = \hat{\psi} e^{ikx_0 \sin\xi \cos\phi_k} e^{i\omega t} \sum_{n=0}^\infty A_n h_n^{(2)}(kr) P_n(\cos\gamma_k). \tag{2.4.3}$$

In the above expression we have taken into consideration that for X-waves $\theta_k = \xi$. We can substitute Eq. (2.3.3), to rewrite Eq. (2.4.3) in the following form:

$$\Phi^s(\vec{r},t) = e^{\pm ikx_0 \sin\xi \cos\phi_k} \sum_{n=0}^\infty A_n h_n^{(2)}(kr) \sum_{m=0}^n \varepsilon_m \frac{(n-m)!}{(n+m)!} P_n^m(\cos\tilde{\theta}) P_n^m(\cos\xi) \cos(m(\phi_k - \phi))$$

$$\tag{2.4.4}$$

20

The backscattered angle $\widetilde{\theta} = \theta = \pi$ if the source is placed off-center, while the detector is located in front of the sphere on the z-axis. However, in practical situations the detector of backscattered signals is attached to the source. The backscattered angle, according to Fig. (2.4.a), would be given by

$$\widetilde{\theta} = \frac{\pi}{2} + \cos^{-1}\left(\frac{x_0}{r}\right). \tag{2.4.5}$$

Similarly, the forward scattered angle according to Fig. (2.4.b) would be:

$$\widetilde{\theta} = \frac{\pi}{2} - \cos^{-1}\left(\frac{x_0}{r}\right). \tag{2.4.6}$$

Multiplying the scattered potential by the AXW spectrum and integrating over the momentum space yields

$$\Psi_{AXW}^{S}(r,\theta,\phi,t) = 2\pi \int_0^{2\pi} d\phi_k \int_0^{\infty} dk\, k^q e^{ikct} e^{-ka} e^{ikx_0 \sin\xi \cos(\phi_k - \phi)} \sum_{n=0}^{\infty} A_n h_n^{(2)}(kr)$$

$$\times \sum_{m=0}^{n} \varepsilon_m \frac{(n-m)!}{(n+m)!} P_n^m(\cos\widetilde{\theta}) P_n^m(\cos\xi) \cos(m(\phi_k - \phi)). \tag{2.4.7}$$

Notice that for the detection scheme illustrated in Fig. (2.4.a) x_0 is positive for $\phi = 0$ and is negative for $\phi = \pi$. According to the symmetry of the problem, we expect that both cases will give the same result. We shall try to simplify the expression given in Eq. (2.4.7) using one of these two possibilities; namely, that x_0 is positive and $\phi = 0$. For this case, Eq. (2.4.7) can be written as

$$\Psi_{AXW}^{S}(r,\theta,\phi,t) = 2\pi \int_{0}^{2\pi} d\phi_k \int_{0}^{\infty} dk \, k^q \, e^{ikct} e^{-ka} e^{ikx_0 \sin\xi \cos\phi_k} \sum_{n=0}^{\infty} A_n h_n^{(2)}(kr)$$

$$\times \sum_{m=0}^{n} \varepsilon_m \frac{(n-m)!}{(n+m)!} P_n^m \left(\cos\tilde{\theta}\right) P_n^m (\cos\xi) \cos(m\phi_k). \qquad (2.4.8)$$

Let $u = kx_0 \sin\xi$, and replace $\cos m\phi_k$ by its definition

$$\cos m\phi_k = \frac{1}{2}\left(e^{im\phi_k} + e^{-im\phi_k}\right).$$

The integration over ϕ_k will have the following form:

$$\frac{1}{2}\int_{0}^{2\pi} d\phi_k e^{iu\cos\phi_k}\left(e^{im\phi_k} + e^{-im\phi_k}\right) = \frac{1}{2}\left(\int_{0}^{2\pi} d\phi_k e^{i(u\cos\phi_k + m\phi_k)} + \int_{0}^{2\pi} d\phi_k e^{i(u\cos\phi_k - m\phi_k)}\right)$$

Using the following definition of the Bessel function

$$J_{\pm n}(x) = \frac{(\pm i)^{\mu n}}{2\pi} \int_{0}^{2\pi} e^{\pm i(x\cos\theta + n\theta)} d\theta,$$

the integration over ϕ_k yields

$$\frac{1}{2}\int_{0}^{2\pi} d\phi_k e^{iu\cos\phi_k}\left(e^{im\phi_k} + e^{-im\phi_k}\right) = \frac{1}{2}\left((i)^m 2\pi J_m(u) + (i)^{-m} 2\pi J_{-m}(u)\right).$$

The negative orders of the Bessel function are related to the positive ones through the relationship $J_{-m}(u) = (-1)^m J_m(u)$. Therefore, the integration over ϕ_k reduces to

$$\frac{1}{2}\int_{0}^{2\pi} d\phi_k e^{iu\cos\phi_k}\left(e^{im\phi_k} + e^{-im\phi_k}\right) = \left((i)^m \pi J_m(u) + (i)^{-m}\pi(-1)^m J_m(u)\right)$$

$$= 2\pi i^m J_m(u).$$

Using this result in Eq. (2.4.8), we arrive at the expression

$$\Psi^{S}_{AXW}\left(r,\theta,\phi,t\right)=4\pi^{2}\int\limits_{0}^{\infty}dk\,k^{q}e^{ikct}e^{-ka}\sum\limits_{n=0}^{\infty}A_{n}h_{n}^{(2)}(kr)\sum\limits_{m=0}^{n}i^{n}\varepsilon_{m}\frac{(n-m)!}{(n+m)!}$$

$$\times P_{n}^{m}\left(\cos\tilde{\theta}\right)P_{n}^{m}\left(\cos\xi\right)J_{m}\left(kx_{0}\sin\xi\right). \qquad (2.4.9)$$

The AXW pulse scattered by a rigid sphere, due to incidence off-centered by a distance x_{0} or $-x_{0}$, can be written explicitly as

$$\Psi^{S}_{AXW}\left(r,\theta,\phi,t\right)=4\pi^{2}\int\limits_{0}^{\infty}dk\,k^{q}e^{ikct}e^{-ka}\sum\limits_{n=0}^{\infty}-(-i)^{n}(2n+1)h_{n}^{(2)}(kr)\frac{j_{n}'(kR)}{h_{n}^{(2)'}(kR)}$$

$$\times\sum\limits_{m=0}^{n}i^{n}\varepsilon_{m}\frac{(n-m)!}{(n+m)!}P_{n}^{m}\left(\cos\tilde{\theta}\right)P_{n}^{m}\left(\cos\xi\right)J_{m}\left(kx_{0}\sin\xi\right). \qquad (2.4.10)$$

2.5 NUMERICAL RESULTS FOR ON-CENTER INCIDENCE

In this section, we discuss the behavior of the scattered AXW pulse due to on-center incidence. Our primary aim is to study the effect of changing the parameters and variables appearing in the spectrum of the scattered pulse given in Eq. (2.3.15). The quantities of interest are θ, a, ξ, R and r determining the scattering angle, the pulse width, the apex angle of the spectral cone, the radius of the scattering sphere, and the observation distance, respectively.

2.5.1 Effect of Changing the Scattering Angle

We consider the spectrum of the scattered pulse at different scattering angles ranging from $\theta=0$ to $\theta=\pi$ in multiples of $\pi/6$. As shown in Fig. (2.5), $\theta=\pi$ determines the position of detection of the backscattered signals, while $\theta=0$ is the forward scattering angle. The plots shown in Figs. (2.6.a) to (2.6.g) give the absolute spectrum

23

of the scattered field at each one of the aforementioned angles. The incident AXW pulse is characterized by the parameters $a = 20\,\text{mm}$, $q = 1$ and $\xi = 2°$. The spectra are calculated at $r = 150\,\text{mm}$ for a scattering sphere having a radius $R = 30\,\text{mm}$. If we compare the backscattered spectrum of Fig. (2.6.a) with the forward scattered spectrum of Fig. (2.6.g), we find that the amplitude of the spectrum is higher in the case of the forward scattering. Another interesting observation is the smooth shape of the spectrum of the forward scattered field. In contradistinction, the backscattered spectrum contains a number of peaks and dips that carry specific information about the scattering sphere. This indicates that the backscattered field can be more useful for identification and characterization purposes. The details of how this is done are provided in Sec. 2.5.4.

2.5.2 Effect of Changing the Pulse Width

The temporal frequency content of the X-wave is determined by the parameters a and q. Specifically, the peak of the spectrum occurs at $\omega_{peak} = qc/a$. The maximum frequency corresponds to the point at which the temporal spectrum decays to $1/e^4$ of the peak value. This criterion yields the following expression $\omega_{max} = (q + 4)c/a$. The axial and lateral widths of the AXW pulse depend on the parameter a and are equal to $a/\cos\xi$ and $a/\sin\xi$, respectively [cf. Fig. (2.2)]. One should notice that the smaller the pulse width the larger the frequency bandwidth.

In Fig. (2.7), plots of the backscattered spectra calculated at $r = 150\,\text{mm}$ for $R = 30\,\text{mm}$, $q = 1$ and $\xi = 2°$ are displayed. The various plots correspond to having

24

$a = 20\,\text{mm}$, $30\,\text{mm}$, $40\,\text{mm}$, and $50\,\text{mm}$. According to Fig. (2.7), the smaller the value of a the more details we can get from the backscattered spectrum. This implies that we should use pulses with very small width compared to the scatterer or alternatively that ultra-wideband pulses are more effective for identification purposes. However, possible problems might arise because reducing the pulse width by more than five times the sphere radius causes the series solution to diverge. Therefore, it is recommended to optimize the frequency bandwidth and pulse width that could be chosen using a rough estimate of the size of the scattering sphere.

2.5.3 Effect of Changing the Apex Angle

The apex angle of the conic surface on which the pulsed plane waves are superimposed is related to the pulse width. According to Fig. (2.2), the width of the pulsed plane wave components that form the X-wave causes the lateral and axial waists to be equal to $a/\sin\xi$ and $a/\cos\xi$, respectively. Changing the apex angle affects the pulse width but does not influence the bandwidth of the AXW pulse.

In Fig. (2.8), we show the scattered spectra for different ξ angles. We started with an apex angle $\xi = 0°$, which corresponds to having an incident pulsed plane wave instead of an X-wave. We chose apex angles equal to $\xi = 20°$ and $40°$. For values of $\xi \leq 20°$ the backscattered spectra are almost the same; the only difference is a slight decrease in the amplitudes. This is due to the fact that for $\xi \leq 20°$, $\cos\xi \approx 1$. On the other hand, for $\xi = 40°$ the argument of the Legendre function in the series solution differs appreciably from 1 and the shape of the spectrum changes noticeably.

25

Physically, one can think of the condition $\xi \leq 20°$ to correspond to operating within a paraxial regime, where all plane wave spectral components are coming in at small angle relative to the axis of propagation.

2.5.4 Effect of Changing the Radius of the Sphere

In this subsection, we consider the variation in the shape of spectra of the backscattered fields as the radius of the scattering sphere is changed. In Fig. (2.9), the absolute spectra are plotted for $R = 30\,mm$, $40\,mm$, $50\,mm$ and $60\,mm$. The incident AXW pulse has $a = 20\,mm$, $q = 1$ and $\xi = 2°$. As the radius of the scattering sphere is increased, the amplitude of the backscattered spectrum increases and the average spacing of the dips decreases. This observation implies that we can extract information about the size of the spheres from the backscattered spectrum by doing a calibration curve between the radii of the spheres and the average spacing of the dips. Fig. (2.10) shows this kind of calibration curve which is constructed using the information taken from three known sphere sizes $R = 20\,mm$, $40\,mm$, and $60\,mm$. The calibration curve was drawn using MS Excel, where the best fit of the points suggested the relationship $R = 926.63\left(\Delta k_{av}\right)^{-0.908}$ between the radius of the sphere R in mm and the separation between the spectral dips Δk_{av} given in m^{-1}. To establish that the information included in the dips of the spectra can be used to determine the radii of the scattering spheres, we calculated the average separation between the dips of the spectra of the AXW fields scattered from spheres having radii $R = 30\,mm$, $50\,mm$, and $80\,mm$. Subsequently, we went back to the calibration curve and found estimates for these radii. A comparison between the estimated and actual radii is found in Table

26

2.1. The tabulated results show that the percentage errors in our estimates of the sizes of the spheres are minimal.

2.5.5 Effect of Changing the Observation Distance

Another issue we consider here is the relation between the decay of the scattered field and the distance traveled. In Figs. (2.11.a-c), we have the backscattered spectrum for an AXW pulse having $a = 20\,\text{mm}$, $q = 1$ and apex angle $\xi = 2°$. The pulse is scattered by a sphere of radius $R = 30\,\text{mm}$ at different distances of $r = 150\,\text{mm}$, $1500\,\text{mm}$, and $15000\,\text{mm}$, respectively. Comparing the amplitudes of the spectrum of the three figures shows that the pulse spectrum decays as $(1/r)$. This indicates that the scattered pulse is almost uniformly distributed in all directions.

2.6 NUMERICAL RESULTS FOR OFF-CENTER INCIDENCE

In practical situations, the source and detector may be sweeping behind or in front of the sphere. This means that the pulse incident on the sphere might not be directed towards the center of the sphere but shifted by a distance of $\pm x_0$. In this case, we cannot consider our problem azimuthally symmetric. Moreover, in such cases the back and forward scattered angles are not simply $\theta = \pi$ and $\theta = 0$ as previously mentioned in the case of on-center incidence. They have to be recalculated according to the new back- and forward-scattering schemes shown in Fig. (2.4). From this figure, the back and forward scattered angles $\tilde{\theta}$ are equal to $\left((\pi/2) + \cos^{-1}(x_0/r)\right)$ and $\left((\pi/2) - \cos^{-1}(x_0/r)\right)$, respectively.

27

Figs. (2.12.a-c) show the effect of changing the source and detection distance by a value of $\pm x_0$ from the center of the sphere. The incident AXW pulse is characterized by $a = 20\,\text{mm}$, $q = 1$ and $\xi = 2°$. We started with $x_0 = 0$ which corresponds to the case of on-center incidence and then increased the distance to $x_0 = \pm 15\,\text{mm}$. Subsequently, we doubled the value of x_0 until we reached a value of $120\,\text{mm}$. Referring to the backscattered spectrum, shown in Figs. (2.12.a-c), we have good results for distances that are less than $x_0 = \pm 60\,\text{mm}$ which is about 40% of the observation distance. For this range of off-center shifts, we only have a slight shift in the positions of the peaks with minimal decrease in the amplitudes. However, for $x_0 \geq 60\,\text{mm}$, the shift in peak positions is increased causing high percentage error in the calculated radii of the spheres as shown in Tables (2.2.a-c). Spectra resulting from forward scattering are shown in Fig. (2.13). It can be seen that such spectra have no dips and no information can be extracted from them.

2.7 CONCLUDING REMARKS

In this chapter, we studied the scattering of acoustic X-wave by a rigid sphere. We derived expressions for the scattered field due to an AXW pulse incident on the sphere. Two cases are considered, where the pulse is incident on and off center. We investigated the effect of changing the scattering angle on the spectrum of the scattered field. Furthermore, we studied the effect of changing the pulse width, apex angle, and the bandwidth of the incident AXW pulse. The influences of the radius of sphere, and observation distance on the scattered field were also considered. It has

been shown that backscattered fields exhibit spectra that contain more information about the scattering sphere than the forward scattered ones. When the parameters characterizing the incident pulse were considered, we have found that the axicon angle has very little effect when it acquires values lesser than $20°$. This is the case because the plane wave spectral components of the AXW become paraxial in nature. On the other hand, the parameter a, controlling the bandwidth of the AXW pulse, appears to have decisive influence on the shape of the scattered spectra. The dips appearing in the backscattered spectra become more pronounced as a gets smaller. Furthermore, we have shown how an unknown radius of a scattering sphere could be identified from the backscattered spectrum. This possibility can have important applications in areas such as remote sensing and target identification. Furthermore, we extended our study to off-center scattering where we recalculated the back and forward scattering angles. We proved that even in case of off-center incidence, we could still extract the sphere size. However, as the axis of propagation of the incident pulse moves farther away from the center of the sphere we start getting higher errors.
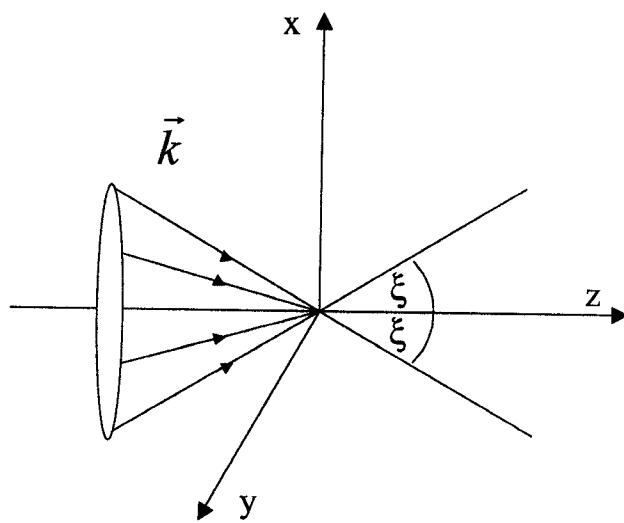
Figure 2.1 Wave vectors of the normally incident X-wave lying on a conic surface having an apex angle ξ.

Waist (lateral width)
of the XW

$a/\sin\xi$

Axial width
of the XW

$a/\cos\xi$

The width of the
pulsed plane wave

a
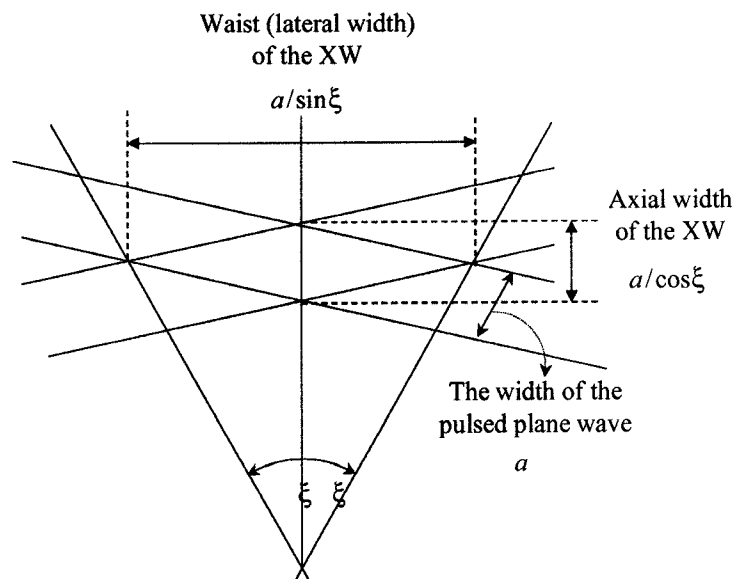
Figure 2.2   The axial and lateral widths of the X-wave and their relation to the width of the pulsed plane wave components.
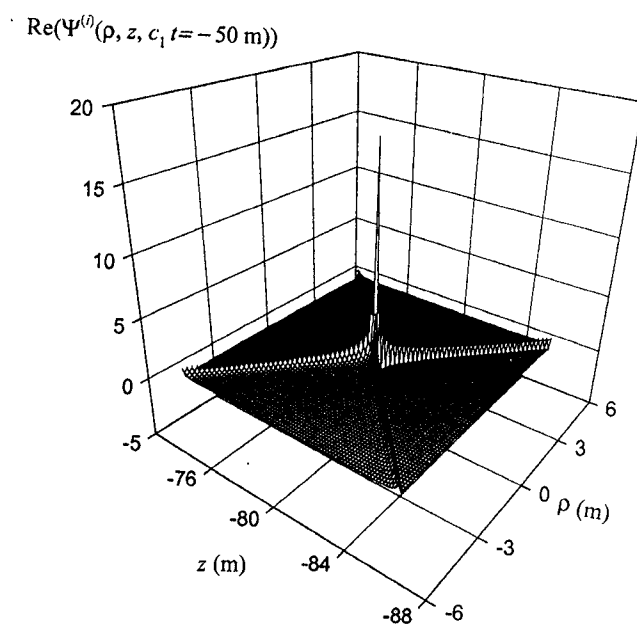
$\mathrm{Re}(\Psi^{(i)}(\rho, z, c_1 t = -50\ \mathrm{m}))$

Figure 2.3   Surface plot of the AXW pulse

$Re(\Psi^{(i)}(\rho, z, c_1 t = -50 \text{ m}))$

Figure 2.3   Surface plot of the AXW pulse

32
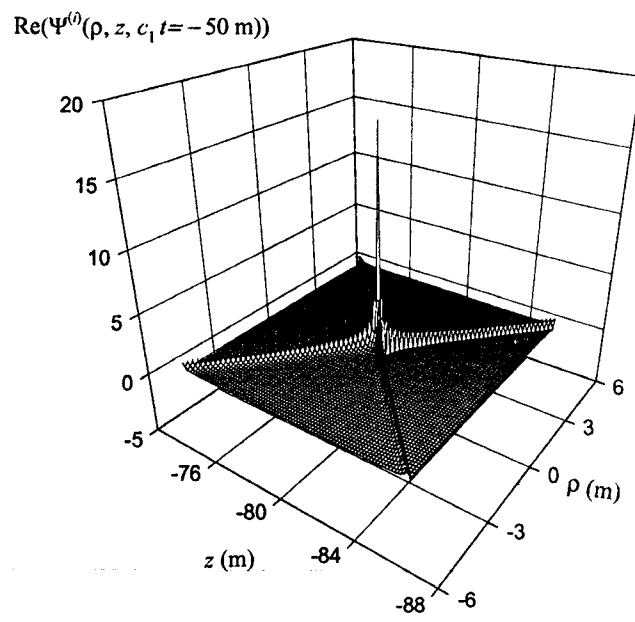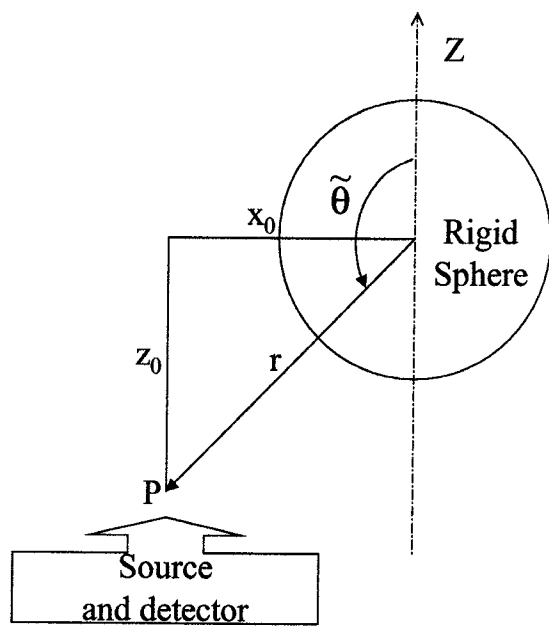
Figure 2.4.a Back scattered scheme due to pulse incident off center by distance $x = -x_0$.
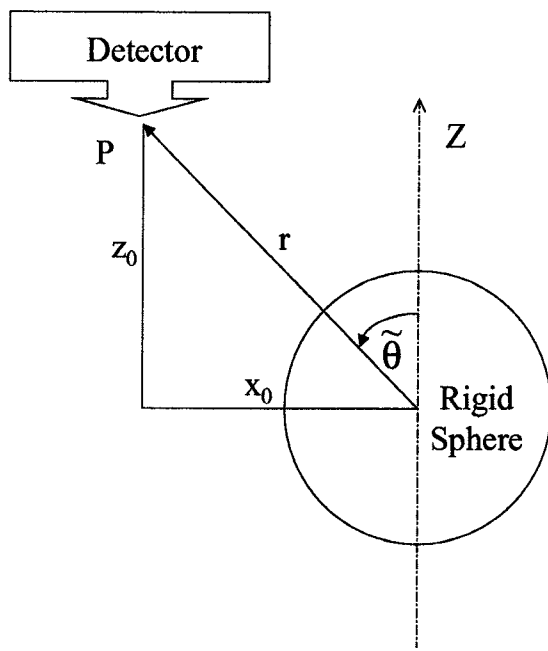
Figure 2.4.b Forward scattered scheme due to pulse incident off center by distance $x = -x_0$.
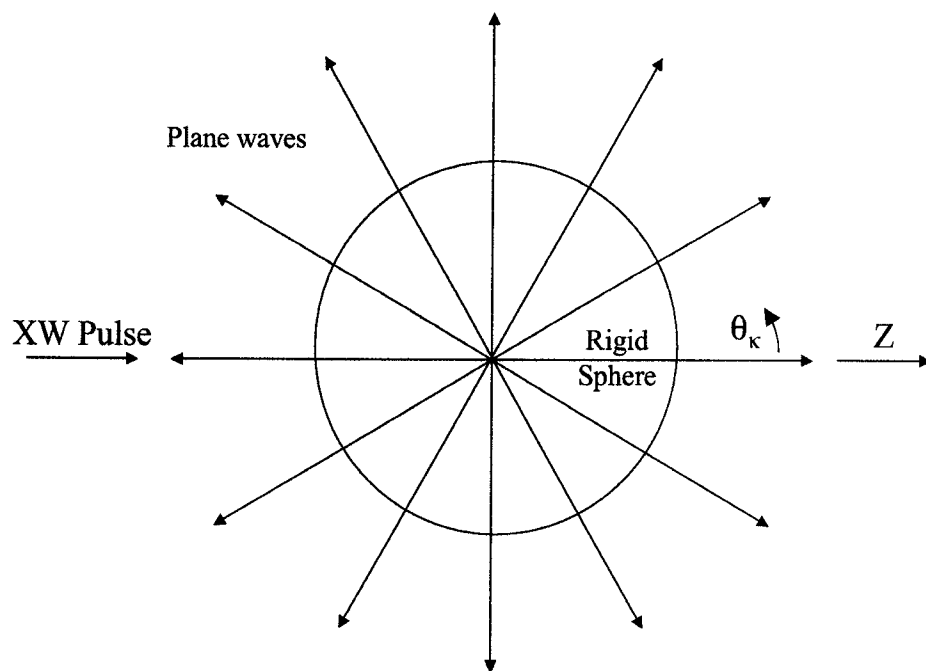
Figure 2.5 The equivalence between weighted plane waves incident on the rigid sphere from different directions and an AXW pulse.

35
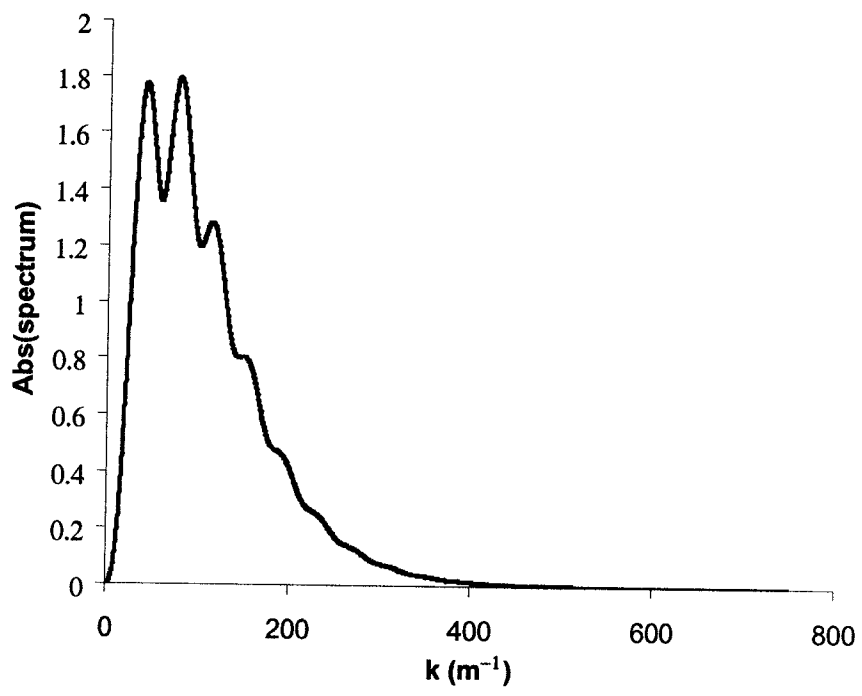
Figure 2.6.a Backscattered spectrum by a rigid sphere for $R = 30$ mm, $r = 150$ mm, $a = 20$ mm and $\theta = \pi$ due to an AXW pulse incident on center.
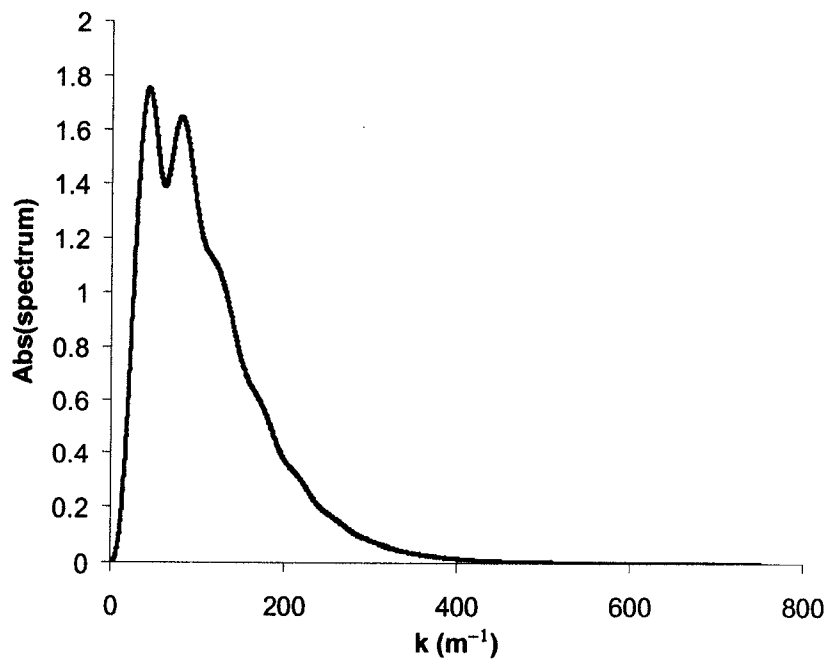
Figure 2.6.b   Scattered spectrum by a rigid sphere for $R = 30\,\text{mm}$, $r = 150\,\text{mm}$, $a = 20\,\text{mm}$, and $\theta = 5\pi/6$ due to an AXW pulse incident on center.
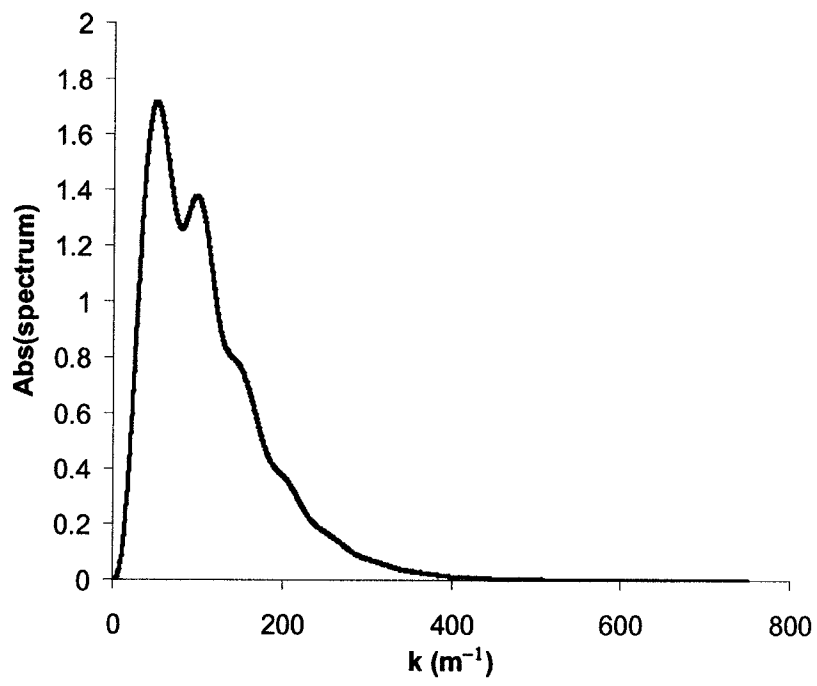
Figure 2.6.c Scattered spectrum by a rigid sphere for $R = 30\,\text{mm}$, $r = 150\,\text{mm}$, $a = 20\,\text{mm}$, and $\theta = 2\pi/3$ due to an AXW pulse incident on center.

38
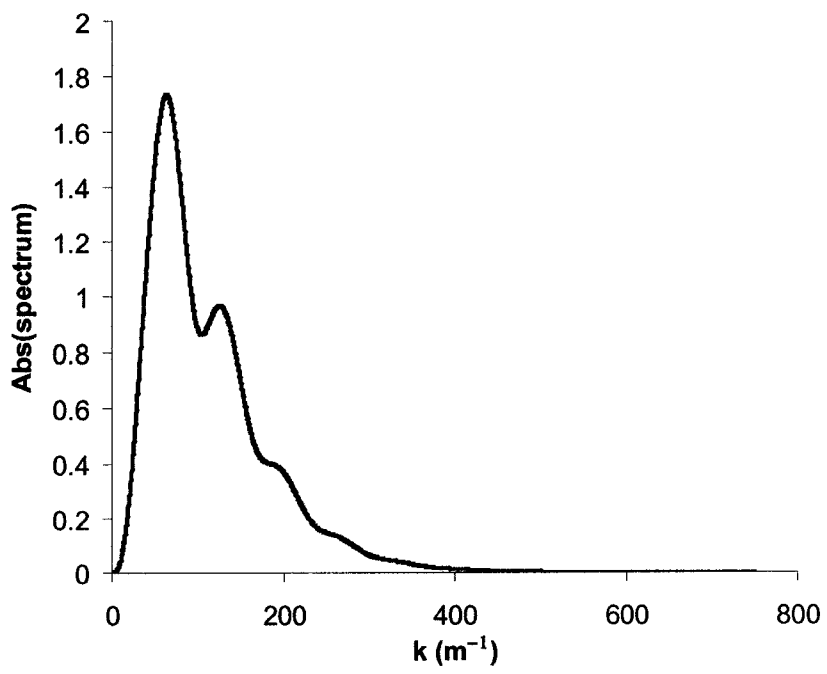
Figure 2.6.d Scattered spectrum by a rigid sphere for $R = 30\,\text{mm}$, $r = 150\,\text{mm}$, $a = 20\,\text{mm}$, and $\theta = \pi/2$ due to an AXW pulse incident on center.
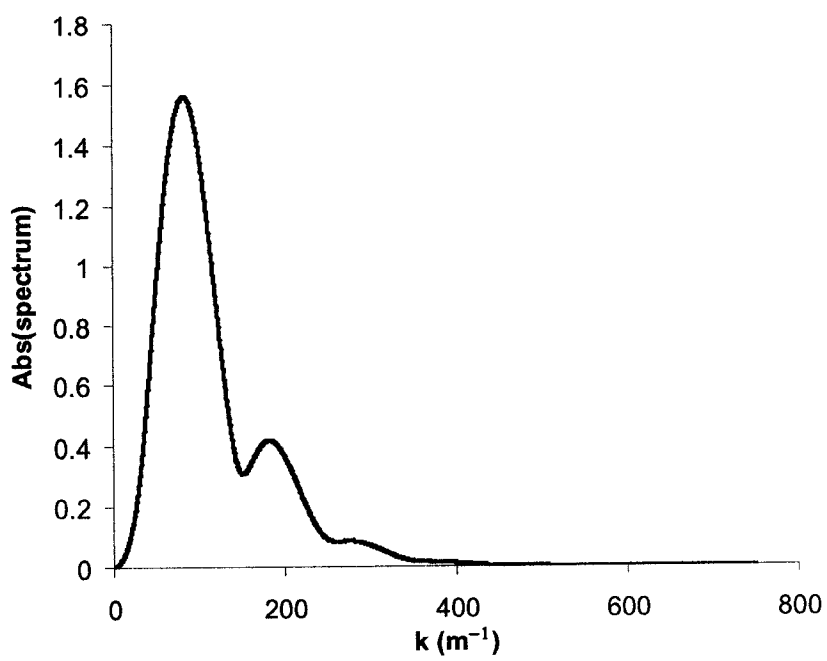
Figure 2.6.e Scattered spectrum by a rigid sphere for $R = 30\,\mathrm{mm}$, $r = 150\,\mathrm{mm}$, $a = 20\,\mathrm{mm}$, and $\theta = \pi/3$ due to an AXW pulse incident on center.
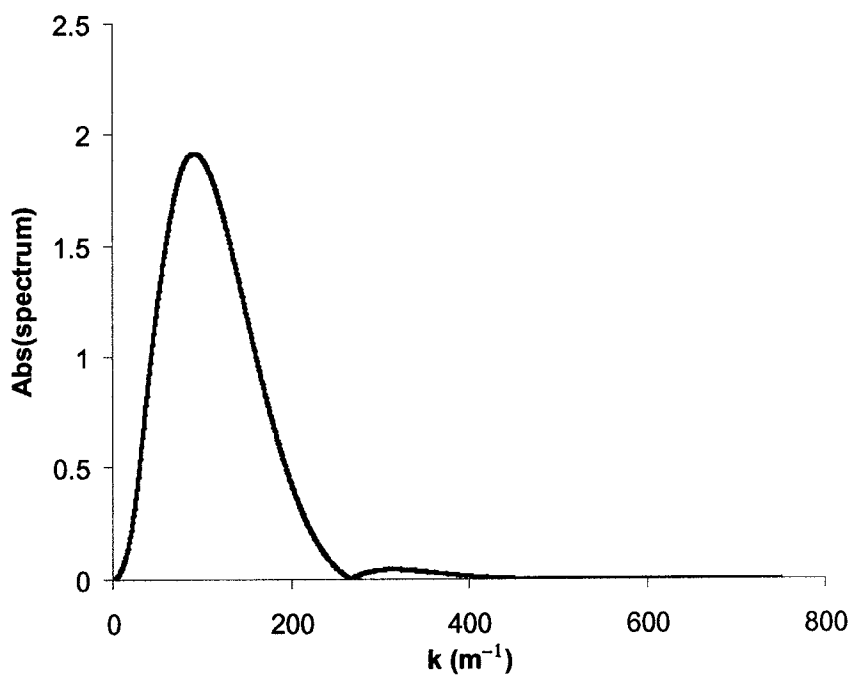
Figure 2.6.f Scattered spectrum by a rigid sphere for $R = 30\,\text{mm}$, $r = 150\,\text{mm}$, $a = 20\,\text{mm}$, and $\theta = \pi/6$ due to an AXW pulse incident on center.

41
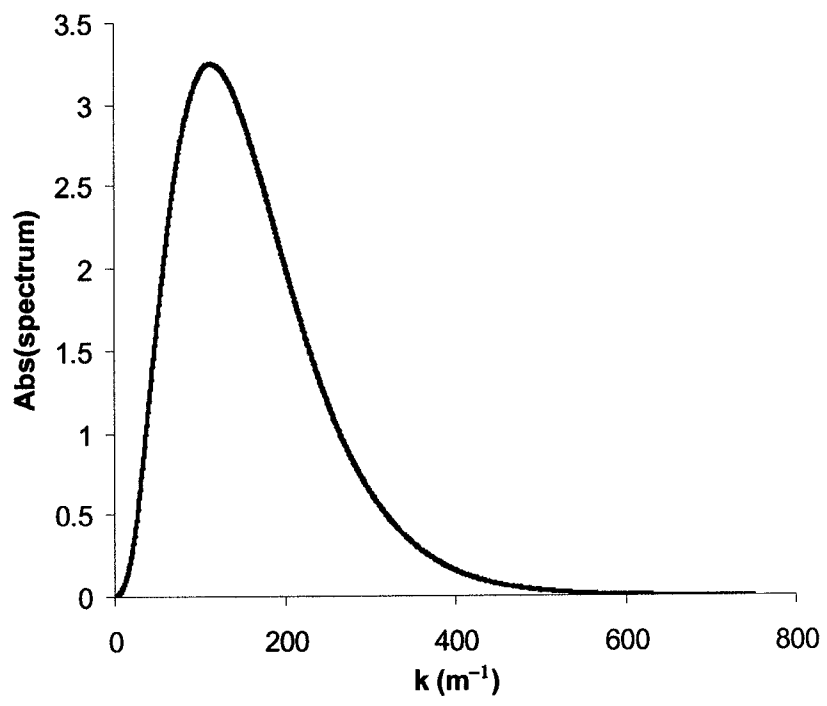
Figure 2.6.g Forward scattered spectrum by a rigid sphere for $R = 30\,\text{mm}$, $r = 150\,\text{mm}$, $a = 20\,\text{mm}$, and $\theta = 0$ due to an AXW pulse incident on center.
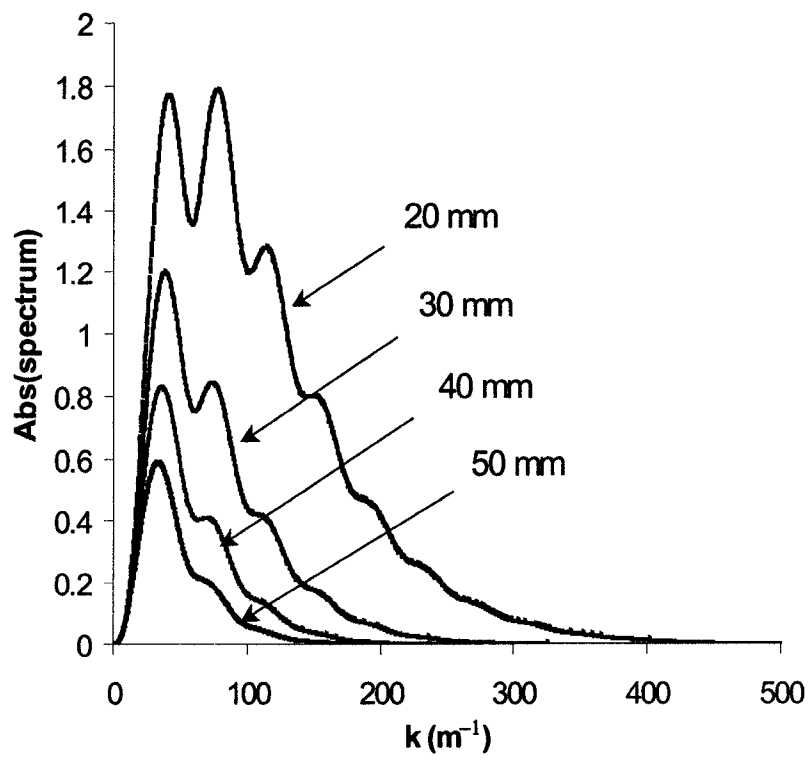
Figure 2.7 Backscattered spectra by rigid sphere for $R = 30\,\text{mm}$, and $r = 150\,\text{mm}$ different pulse widths: $a = 20\,\text{mm}$, 30mm, 40 mm, and 50 mm, due to an AXW pulse incident on center.

43
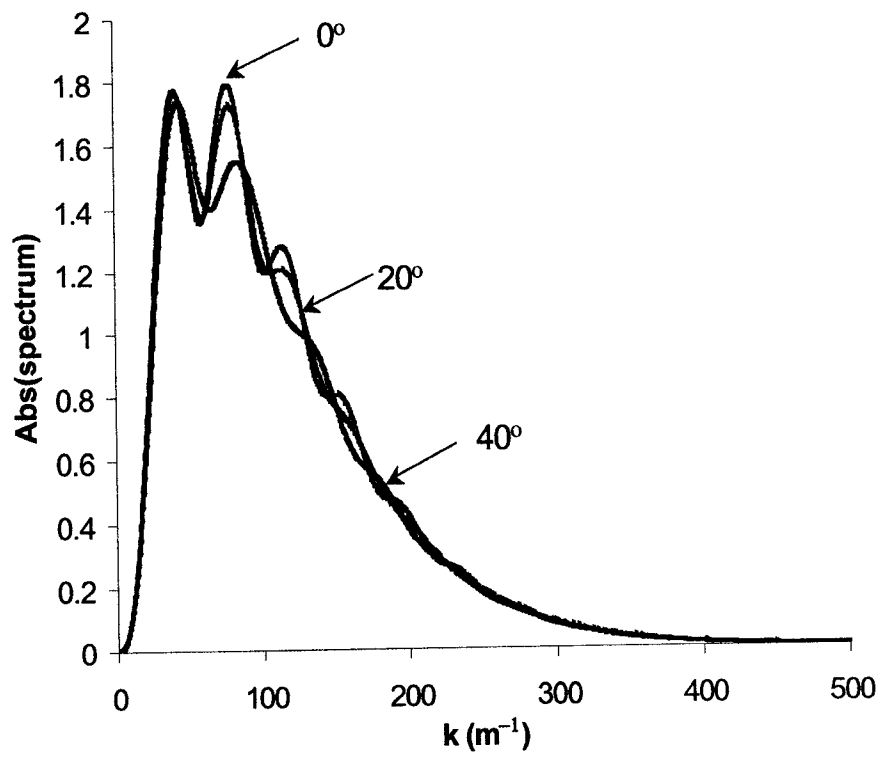
Figure 2.8 Backscattered spectra by rigid sphere for $R = 30\,\text{mm}$, $r = 150\,\text{mm}$, and $a = 20\,\text{mm}$ due to an AXW pulse incident on center with different apex angles: $\xi = 0°$, $\xi = 20°$ and $\xi = 40°$.
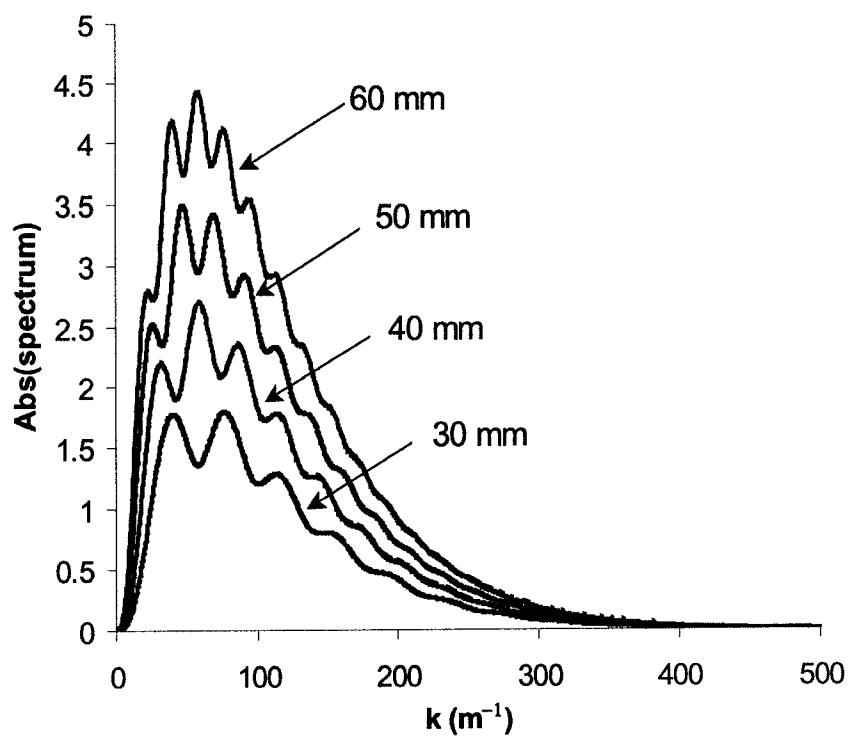
Figure 2.9 Backscattered spectra by a rigid sphere for different radii: $R = 30$ mm, 40 mm, 50 mm and 60 mm; $r = 150$ mm and $a = 20$ mm due to an AXW pulse incident on center.
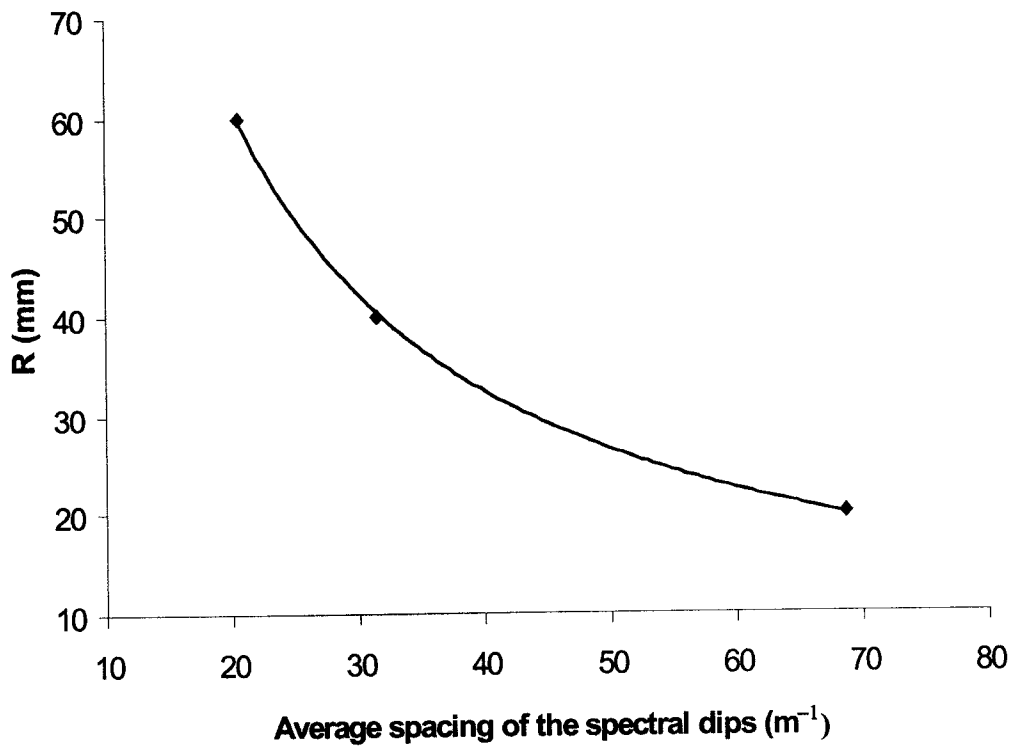
Figure 2.10 Calibration curve between the average spacing of the spectral dips and radius of sphere as obtained by an AXW pulse incident on center for $r = 150\,\text{mm}$, and $a = 20\,\text{mm}$.
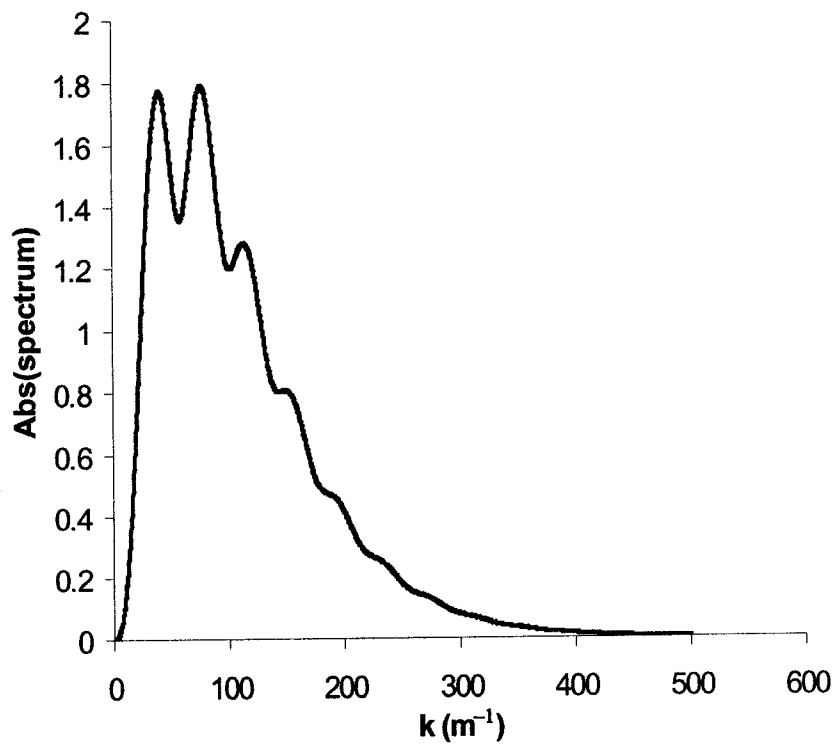
Figure 2.11.a Backscattered spectrum by rigid sphere for $R = 30\,\text{mm}$, $r = 150\,\text{mm}$, $a = 20\,\text{mm}$ due to an AXW pulse incident on center.
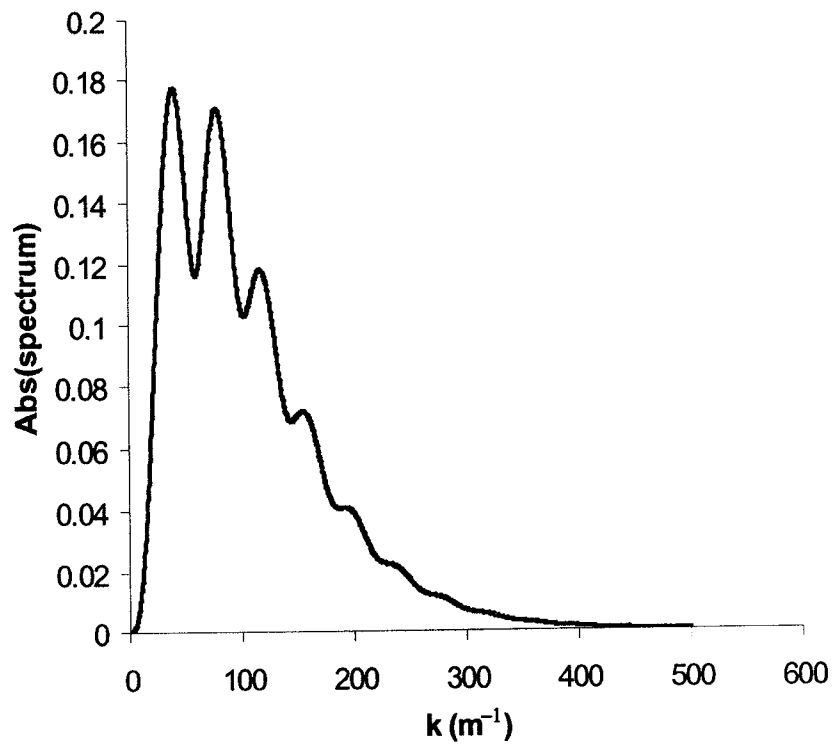
Figure 2.11.b Backscattered spectrum by rigid sphere for $R = 30\,\text{mm}$, $r = 1500\,\text{mm}$, $a = 20\,\text{mm}$ due to an AXW pulse incident on center.
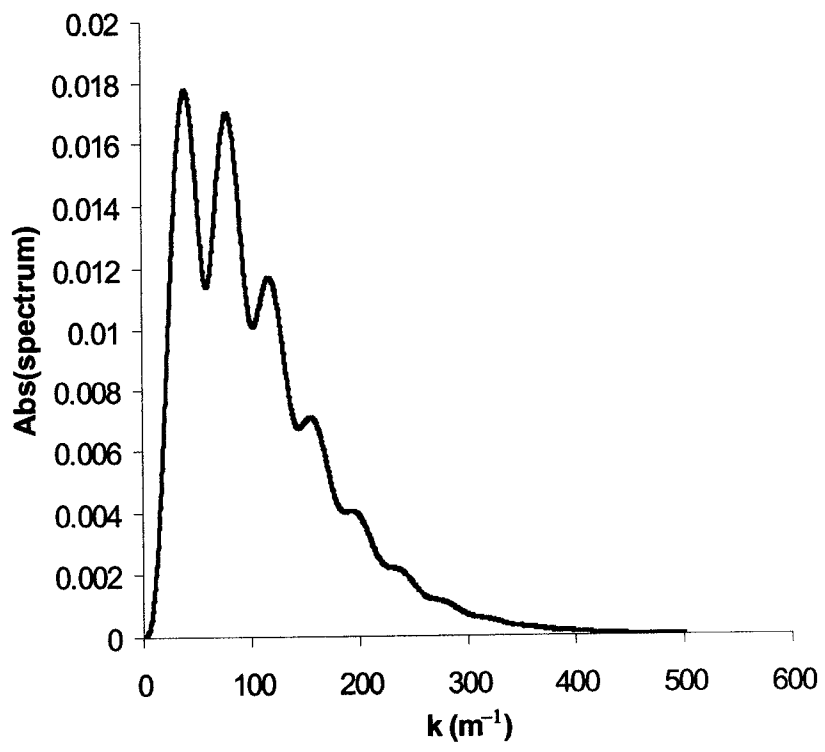
Figure 2.11.c Backscattered spectrum by rigid sphere for $R = 30\,\text{mm}$, $r = 15000\,\text{mm}$, $a = 20\,\text{mm}$ due to an AXW pulse incident on center.
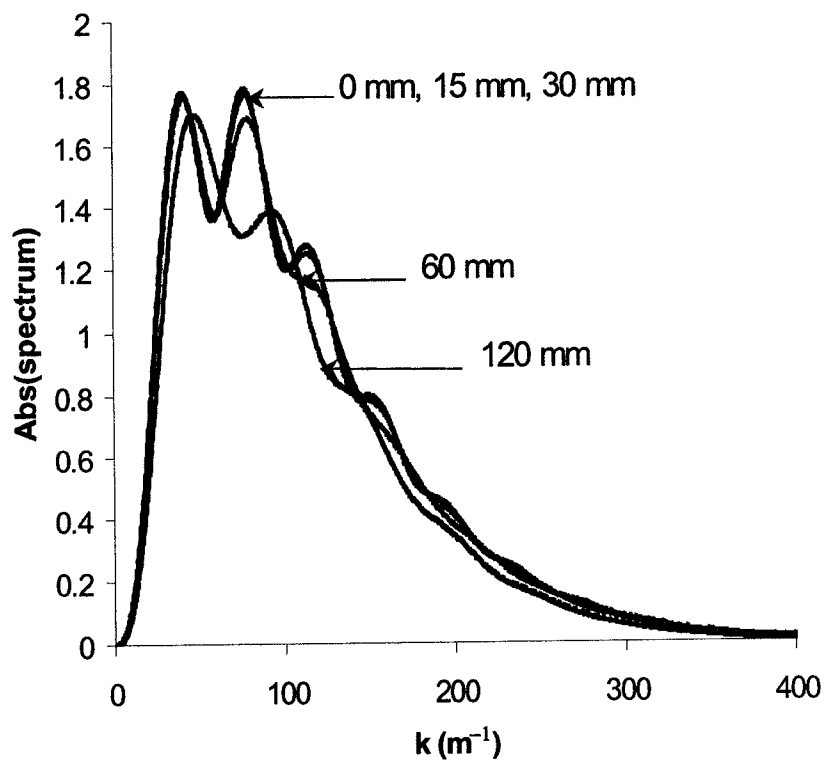
Figure 2.12.a Backscattered spectrum by rigid sphere for $\tilde{\theta} = (\pi/2) + \cos^{-1}(x_0/r)$, $R = 30\,\text{mm}$, $r = 150\,\text{mm}$, $a = 20\,\text{mm}$ and different values of x_0 due to an AXW pulse incident off center.
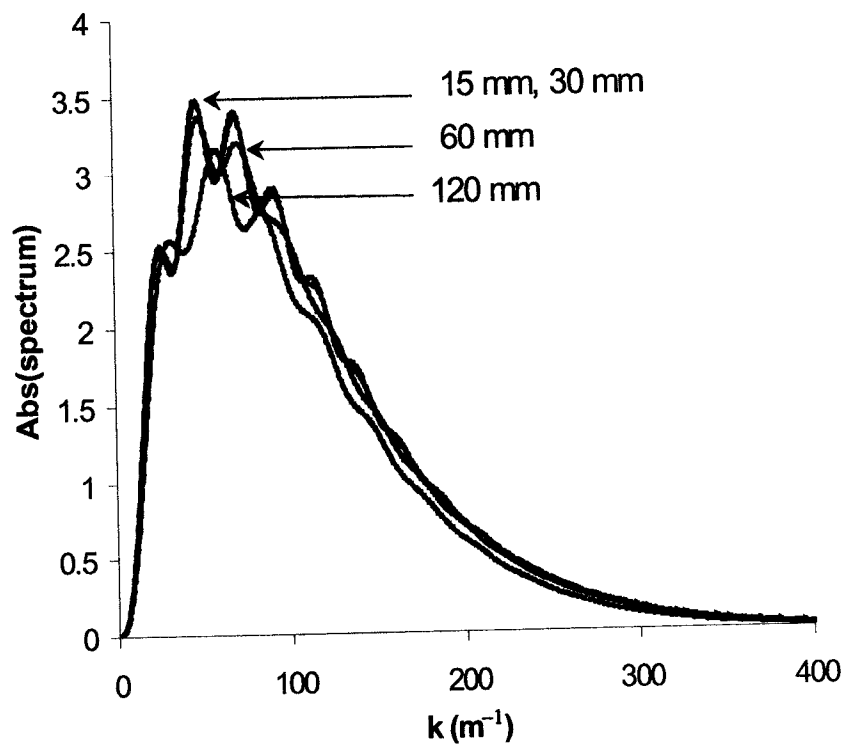
Figure 2.12.b Backscattered spectrum by rigid sphere for $\tilde{\theta} = (\pi/2) + \cos^{-1}(x_0/r)$, $R = 50$ mm, $r = 150$ mm, $a = 20$ mm, and different values of x_0 due to an AXW pulse incident off center.
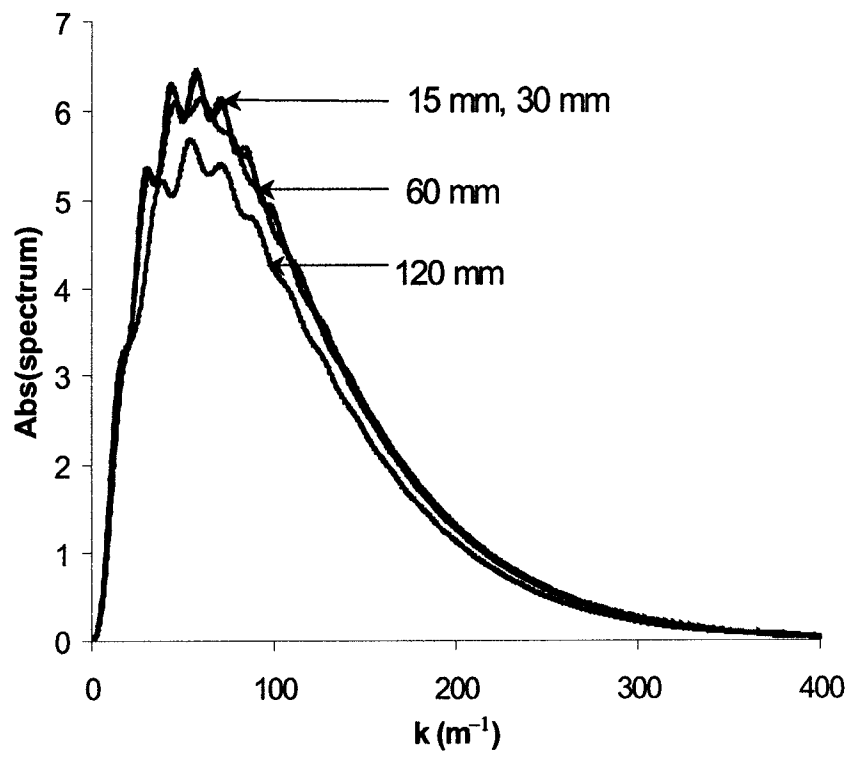
Figure 2.12.c Backscattered spectrum by rigid sphere for $\widetilde{\theta} = (\pi/2) + \cos^{-1}(x_0/r)$, $R = 80\,\text{mm}$, $r = 150\,\text{mm}$, $a = 20\,\text{mm}$ and different values of x_0 due to an AXW pulse incident off center.
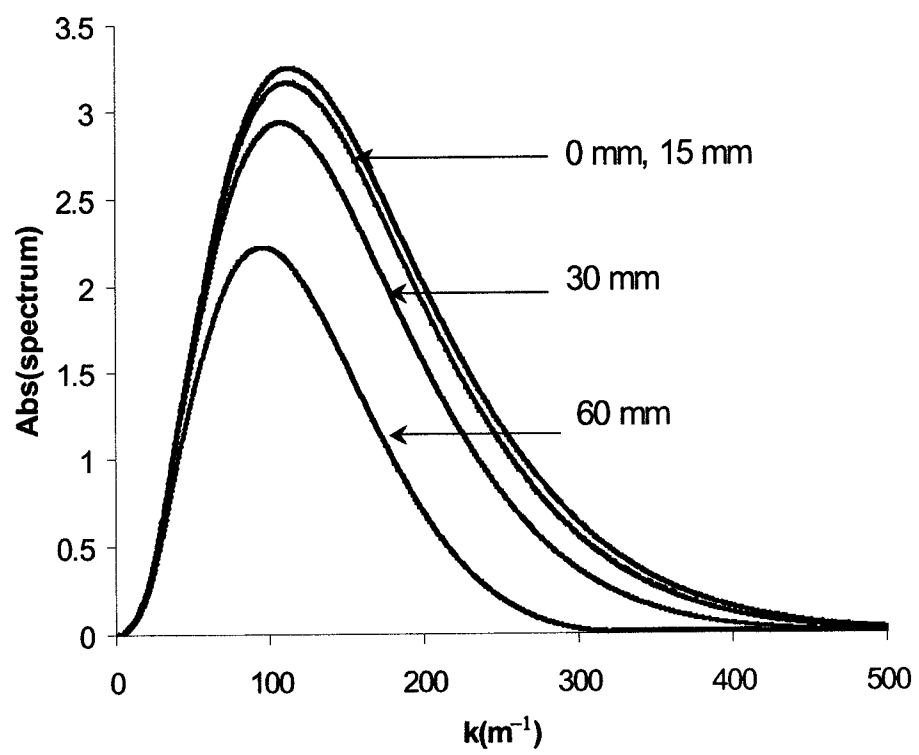
Figure 2.13   Forward scattered spectra by rigid sphere for $\tilde{\theta} = (\pi/2) - \cos^{-1}(x_0/r)$, $R = 30$ mm, $r = 150$ mm, $a = 20$ mm and different values of x_0 due to an AXW pulse incident off center.

Average Spacing of the Dips $(\text{m})^{-1}$	Estimated Radius (mm)	Actual Radius (mm)	% Error
43.1250	30.38	30.00	1.27
24.5625	50.65	50.00	1.25
15.0000	79.27	80.00	0.91

Table 2.1   Comparison between the estimated and actual radii of the spheres as have been calculated from the average spacing of the dips that are obtained from the backscattered spectrum due to on-center incidence.

54

Average Spacing of the Dips $(m)^{-1}$	Estimated Radius (mm)	Actual Radius (mm)	% Error
43.1250	30.38	30.00	1.27
25.1250	49.62	50.00	0.76
15.0000	79.27	80.00	0.91

Table 2.2.a   Comparison between the estimated and actual radii of the spheres as have been calculated from the average spacing of the dips that are obtained from the backscattered spectrum due to off-center incidence at a distance $x_0 = 15\,mm$.

Average Spacing of the Dips $(m)^{-1}$	Estimated Radius (mm)	Actual Radius (mm)	% Error
44.2500	29.68	30.00	1.07
25.1250	49.62	50.00	0.76
15.1900	78.37	80.00	2.03

Table 2.2.b   Comparison between the estimated and actual radii of the spheres as have been calculated from the average spacing of the dips that are obtained from the backscattered spectrum due to off-center incidence at a distance $x_0 = 30$ mm.

Average Spacing of the Dips (m)$^{-1}$	Estimated Radius (mm)	Actual Radius (mm)	% Error
--.----	--.--	30.00	-.--
27.0000	46.40	50.00	7.20
16.5000	72.70	80.00	9.13

Table 2.2.c Comparison between the estimated and actual radii of the spheres as have been calculated from the average spacing of the dips that are obtained from the backscattered spectrum due to off-center incidence at a distance $x_0 = 60\,\text{mm}$.

Average Spacing of the Dips $(m)^{-1}$	Estimated Radius (mm)	Actual Radius (mm)	% Error
--.----	--.--	30.00	-.--
--.----	--.--	50.00	-.--
20.2500	60.36	80.00	24.55

Table 2.2.d   Comparison between the estimated and actual radii of the spheres as have been calculated from the average spacing of the dips that are obtained from the backscattered spectrum due to off-center incidence at a distance $x_0 = 120\,mm$.

CHAPTER 3

SCATTERING OF ACOUSTIC X-WAVES BY SOFT SPHERES

3.1 INTRODUCTION

In the previous chapter, we studied the scattering of acoustic X-waves by rigid spheres and showed how we can extract the sphere size from the backscattered spectrum. In this chapter, we shall consider the scattering of AXW by soft spheres. For soft spheres the information contained in the backscattered spectrum does not only include the sphere size, but also the density and speed of wave propagation inside the sphere. This information may allow us to determine the material from which the sphere is made. Therefore, we can benefit from the results of this investigation in applications involving material characterization.

3.2 SCATTERED AXW FIELD DUE TO ON-CENTER INCIDENCE

In this section, we derive an expression for an AXW pulse scattered from a soft sphere. We use a series solution approach analogous to the one employed in Chapter 2. First, the scattered field due to an incident plane wave is provided, then the field scattered due to an incident AXW pulse is calculated by superimposing over the spectrum of the X-wave as explained in Sec. 2.2.

To calculate the scattered AXW pulse we assume that the incident field has the form given in Eq. (2.2.9). This representation is a spectral superposition over plane waves. To be able to calculate the scattered field, consider a general expression for a plane wave incident in the direction θ, ϕ. Specifically,

$$\Phi^i\left(r,\phi,\theta,t\right) = e^{-i\vec{k}\cdot\vec{r}}e^{i\omega t} = e^{-ikr\cos\gamma}e^{i\omega t} \tag{3.2.1}$$

where γ is the angle between $\vec{k} \equiv \left(k,\theta_k,\phi_k\right)$, $\vec{r} \equiv \left(r,\theta,\phi\right)$. In Sec. 2.2, it has been shown that an AXW pulse has its entire spectral plane wave components propagating with an angle $\theta_k = \xi$. Following the procedure described in Sec. 2.3, the plane wave given in Eq. (3.2.1) can be expressed as a series in terms of Legendre Polynomials and spherical Bessel functions

$$\Phi^i\left(r,\theta,\phi,t\right) = e^{-ikr\cos\gamma_k}e^{ikct} = \sum_{n=0}^{\infty}(-i)^n(2n+1)P_n\left(\cos\gamma_k\right)j_n\left(kr\right)e^{ikct}, \tag{3.2.2}$$

where $\cos\gamma_k = \cos\theta_k\cos\xi + \sin\theta_k\sin\xi\cos\left(\phi_k - \phi\right)$.

Analogously to the analysis carried out in Sec. 2.3, the scattered field can be represented as a series of concentric spherical waves diverging from the scatterer having the following mathematical form:

$$\Phi^s\left(r,\theta,\phi,t\right) = \sum_{n=0}^{\infty}A_nP_n\left(\cos\gamma_k\right)h_n^{(2)}\left(kr\right)e^{ikct}, \tag{3.2.3}$$

where $P_n\left(\cos\gamma_k\right)$ is given by Eq. (2.3.3) and A_n can be determined from the boundary conditions. Since the center of the scattering sphere lies on the axis of propagation of the AXW pulse, the problem is azimuthally symmetric. Thus, $m = 0$, and the expression for $P_n\left(\cos\gamma_k\right)$ simplifies to:

$$P_n(\cos\gamma_k) = P_n(\cos\theta)P_n(\cos\xi).\qquad(3.2.4)$$

As in Sec. 2.3, the scattered pulse due to on-center incidence reduces to the following form:

$$\Psi^s_{AXW}(r,\theta,\phi,t) = (2\pi)^2 \int_0^\infty dk\, k^q e^{-ka} e^{ikct} \sum_{n=0}^\infty A_n h_n^{(2)}(kr) P_n(\cos\theta) P_n(\cos\xi).\qquad(3.2.5)$$

In case of the soft sphere, there are two regions of interest. We have the outside region in which the incident and scattered fields exist, while the inside region contains the transmitted field. For plane wave solutions, the incident and scattered fields are given by Eqs. (3.2.2) and (3.2.3). Similarly, the field inside the sphere can be written as follows:

$$\Phi^{in}(r,\theta,\phi,t) = \sum_{n=0}^\infty C_n P_n(\cos\gamma_k) j_n(k_e r) e^{ik_e ct},\qquad(3.2.6)$$

where $k_e = (\omega/c_e)$ is the wave number of the material of the sphere. There are two sets of coefficients associated with the inside and scattered fields. To be able to determine these two sets of coefficients, we need two boundary conditions. However, we have to bear in mind that we are more interested in determining A_n, which is the coefficients for the series solution of the scattered field. The two boundary conditions satisfied on the surface of the sphere is that the radial velocity at the first medium should be equal to that of the second medium and that the pressures on the boundary separating the inside and outside of the sphere should be equal. The two boundary conditions could be written explicitly as

$$V_{n1}(r=R,\theta,\phi,t) = V_{n2}(r=R,\theta,\phi,t), \text{ where } \vec{V}(\vec{r},t) = \vec{\nabla}\Phi(\vec{r},t)\qquad(3.2.7)$$

61

and

$$P_1(r = R, \theta, \phi, t) = P_2(r = R, \theta, \phi, t), \text{ where } P(\vec{r}, t) = -\rho_0 \frac{\partial}{\partial t} \Phi(\vec{r}, t) \qquad (3.2.8)$$

Here, ρ_0 is the density of the medium. The first boundary condition indicates that the gradient of the velocity potential in the first medium is equal to that of the second medium; viz.,

$$\frac{\partial \Phi^i}{\partial r} + \frac{\partial \Phi^s}{\partial r} = \frac{\partial \Phi^{in}}{\partial r} \text{ at } r = R, \qquad (3.2.9)$$

where $\Phi^i, \Phi^s, \Phi^{in}$ are given in Eqs. (3.2.2), (3.2.3), and (3.2.6). Substituting these expressions in Eq. (3.2.9), we get

$$e^{ikct} \sum_{n=0}^{\infty} P_n(\cos\gamma_k)\left((-i)^n (2n+1)kj_n'(kR) + A_n k h_n^{(2)'}(kR)\right) = e^{ik_ect} \sum_{n=0}^{\infty} P_n(\cos\gamma_k) C_n j_n'(k_e R).$$

After simplification, we can obtain C_n in terms of A_n

$$C_n = \frac{e^{ikct} k}{e^{ik_ect} k_e j_n'(k_e R)}\left((-i)^n (2n+1)j_n'(kR) + A_n h_n^{(2)'}(kR)\right). \qquad (3.2.10)$$

To apply the second boundary condition, we need to calculate the pressure inside and outside the sphere, viz.,

$$P_1 = -\rho_0\left(\frac{\partial \Phi^i}{\partial t} + \frac{\partial \Phi^s}{\partial t}\right). \qquad (3.2.11)$$

Using Eqs. (3.2.2), (3.2.6) and (3.2.11) the pressure in the outside region can be written as

$$P_1(r, \theta, \phi, t) = -i\rho_0 kce^{ikct} \sum_{n=0}^{\infty} P_n(\cos\gamma_k)\left((-i)^n (2n+1)j_n(kr) + A_n h_n^{(2)}(kr)\right). \qquad (3.2.12)$$

62

Here, ρ_0 is the density of the surrounding medium. The pressure inside the sphere is equal to

$$P_2 = -\rho_e \frac{\partial \Phi^{in}}{\partial t},$$ (3.2.13)

which gives

$$P_2(r,\theta,\phi,t) = -\rho_e i k_e c_e e^{ik_e c_e t} \sum_{n=0}^{\infty} C_n P_n(\cos\gamma_k) j_n(k_e r).$$ (3.2.14)

The density and the wave speed of the sphere are given by ρ_e and c_e, respectively. Equating (3.2.12) with (3.2.14) at $r = R$, we obtain

$$\frac{\rho_0 k c e^{ikct}}{i} \sum_{n=0}^{\infty} P_n(\cos\gamma_k)\left((-i)^n (2n+1) j_n(kR) + A_n h_n^{(2)}(kR)\right) = \frac{\rho_e k_e c_e e^{ik_e c_e t}}{i}$$

$$\times \sum_{n=0}^{\infty} P_n(\cos\gamma_k) C_n j_n(k_e R).$$

Thus, the following relationship between C_n and A_n is obtained from the second boundary condition

$$C_n = \frac{\rho_0 k c e^{ikct}}{\rho_e k_e c_e e^{ik_e c_e t} j_n(k_e R)}\left((-i)^n (2n+1) j_n(kR) + A_n h_n^{(2)}(kR)\right).$$ (3.2.15)

Equating Eqs. (3.2.10) and (3.2.15) to solve for A_n, we get

$$\frac{j_n(k_e R)}{j_n'(k_e R)}\left((-i)^n (2n+1) j_n'(kR) + A_n h_n^{(2)'}\right) = \frac{\rho_0 c}{\rho_e c_e}\left((-i)^n (2n+1) j_n(kR) + A_n h_n^{(2)}(kR)\right).$$

Rearranging terms

$$A_n\left(\frac{j_n(k_e R)}{j_n'(k_e R)} h_n^{(2)'}(kR) - \frac{\rho_0 c}{\rho_e c_e} h_n^{(2)}(kR)\right) = (-i)^n (2n+1)\left(\frac{\rho_0 c}{\rho_e c_e} j_n(kR) - j_n'(kR) \frac{j_n(k_e R)}{j_n'(k_e R)}\right).$$

Therefore, A_n becomes equal to

$$A_n = -(-i)^n(2n+1)\frac{\left(\dfrac{j_n(k_eR)}{j'_n(k_eR)}j'_n(kR) - \dfrac{\rho_0 c}{\rho_e c_e}j_n(kR)\right)}{\left(\dfrac{j_n(k_eR)}{j'_n(k_eR)}h_n^{(2)'}(kR) - \dfrac{\rho_0 c}{\rho_e c_e}h_n^{(2)}(kR)\right)}. \qquad (3.2.16)$$

Taking $(j_n(k_eR)/j'_n(k_eR))$ as a common factor from both the numerator and denominator gives

$$A_n = -(-i)^n(2n+1)\frac{\left(j'_n(kR) - \dfrac{\rho_0 c}{\rho_e c_e}\dfrac{j'_n(k_eR)}{j_n(k_eR)}j_n(kR)\right)}{\left(h_n^{(2)'}(kR) - \dfrac{\rho_0 c}{\rho_e c_e}\dfrac{j'_n(k_eR)}{j_n(k_eR)}h_n^{(2)}(kR)\right)}, \qquad (3.2.17)$$

where $k_e = (\omega/c_e)$, $k = (\omega/c)$, and $c_e = \sqrt{B/\rho_e} = \sqrt{(1/\rho_e \kappa_e)}$. Here, ρ_0 is the density of the medium surrounding the sphere, while ρ_e is the density of the sphere. Similarly, c, and c_e are the speeds of wave propagation outside and inside the sphere, respectively. In addition, R is the radius of the sphere, κ_e is the adiabatic compressibility of the material, and B is the bulk modulus, which is the reciprocal of the compressibility.

Letting $\alpha_n = i(\rho_0 c/\rho_e c_e)(j'_n(k_eR)/j_n(k_eR))$ reduces A_n to the following form

$$A_n = -(-i)^n(2n+1)\frac{(j'_n(kR) + i\alpha_n j_n(kR))}{\left(h_n^{(2)'}(kR) + i\alpha_n h_n^{(2)}(kR)\right)}. \qquad (3.2.18)$$

64

Substituting for A_n from Eq. (3.2.18) in Eq. (3.2.3) gives the following expression for the field scattered by a soft sphere:

$$\Phi^s(r,\theta,\phi,t) = e^{ikct}\sum_{n=0}^{\infty} -(-i)^n(2n+1)\frac{\left(j_n'(kR)+i\alpha_n j_n(kR)\right)}{\left(h_n^{(2)'}(kR)+i\alpha_n h_n^{(2)}(kR)\right)}P_n(\cos\gamma_k)h_n^{(2)}(kr).$$

(3.2.19)

Using this result, the scattered AXW pulse can be written as

$$\Psi_{AXW}^s(r,\theta,\phi,t) = (2\pi)^2\int_0^{\infty}dk\,k^q e^{-ka}e^{ikct}$$

$$\times\sum_{n=0}^{\infty}-(-i)^n(2n+1)\frac{\left(j_n'(kR)+i\alpha_n j_n(kR)\right)}{\left(h_n^{(2)'}(kR)+i\alpha_n h_n^{(2)}(kR)\right)}h_n^{(2)}(kr)P_n(\cos\theta)P_n(\cos\xi).$$

(3.2.20)

It will be shown that the spectrum of this field can be used to determine the radii, density of the scattering sphere, as well as, the speed of propagation of sound in the material of the scatterer.

3.3 SCATTERED FIELD DUE TO INCIDENCE OFF CENTER

In this section, we are interested in providing an expression for the scattered field when the center of the scattering sphere does not lie on the axis of propagation of the incident AXW pulse. Following the analysis given in Sec. 2.4, we obtain the same expression given in Eq. (2.4.9). However, we have to use the expression for the coefficient A_n given in Eq. (2.3.18) instead of that given in Eq. (2.3.13). Explicitly, the off-center scattered field can be written as follows

$$\Psi_{AXW}^{S}(r,\theta,\phi,t) = 4\pi^2 \int_0^\infty dk k^q e^{ikct} e^{-ka} \sum_{n=0}^\infty -(-i)^n (2n+1) \frac{(j_n'(kR) + i\alpha_n j_n(kR))}{\left(h_n^{(2)'}(kR) + i\alpha_n h_n^{(2)}(kR)\right)}$$

$$\times h_n^{(2)}(kr) \sum_{m=0}^n (i)^m \varepsilon_m \frac{(n-m)!}{(n-m)!} P_n^m(\cos\widetilde\theta) P_n^m(\cos\xi) J_m(kx_0 \sin\xi).$$

(3.3.1)

The spectrum appearing in this expression will be used to show how off-center incidence can affect the method advocated in this work for characterizing the size and material of the scattering sphere.

3.4 NUMERICAL RESULTS DUE TO ON-CENTER INCIDENCE

In this section, we discuss the influence of the different parameters characterizing the scattering sphere on the spectrum of the scattered AXW pulse. The effects of changing the bandwidth of the AXW pulse and its axicon angle will not be discussed because their effects are similar to the ones demonstrated for the case the rigid sphere. Specifically, small axicon angles, corresponding to paraxial incidence, have little effect on the shape of the spectrum of the scattered field. On the other hand, smaller values of a increase the bandwidth and make the dips of the scattered spectrum more pronounced. However, we consider the effect of changing the detection angle on the spectrum. In addition, we are going to concentrate on the influences of changing the medium surrounding the scatterer, the radius and the density of the sphere, and the speed of sound propagation in the sphere. Using the information gained from investigating the effects of the various attributes of the scattering spheres on the spectra of the scattered fields, we propose a method by which we can identify the size and material of an unknown spherical object.

3.4.1 Effect of Changing the Scattering Angle

As previously done in Chapter 2, the scattering angle is changed from 0 to π in steps of $\pi/6$ where $\theta = 0$ and $\theta = \pi$ are the forward scattering and backscattering angles. The spectra shown in Figs. (3.1.a-g) are plotted for $R = 30\,\text{mm}$, $r = 150\,\text{mm}$, $a = 20\,\text{mm}$, $q = 1$ and $\xi = 2°$. It should be noted that the backscattered spectrum looks like that of the rigid sphere in the low frequency range up to approximately 35 KHz. However, after 35 KHz, the spectrum becomes different and more spectral-dips appear. As for the spectrum of the forward scattered field, it is almost the same as that of the rigid sphere with higher amplitude than the backscattered. The plots in Fig. (3.1) show that the forward scattered field is smooth and contains no dips. As such, the measured spectra in the forward direction cannot be used in characterizing the sphere or determining its material.

3.4.2 Effect of Changing the Medium Surrounding the Sphere

In order to classify a certain material as rigid or soft, it is important to consider the medium surrounding the scattering object. Fig. (3.2) shows that the backscattered spectra of two spheres, Mn and Pb, placed in air are identical and they look almost the same as that of a rigid sphere. On the other hand, comparing Figs. (3.3.a) and (3.3.b) implies that Mn, and Pb have different backscattered spectra when placed in water. If we recall the expression (3.18) for A_n, we notice that $\alpha_n \to 0$ if the ratio $\left(\rho_0 c / \rho_e c_e\right)$ is very small. In case of air, $\rho_0 = 1\cdot 2\,\text{Kg/m}^3$ and $c = 350\,\text{m/s}$ while for water

$\rho_0 = 1 \cdot 0 \times 10^3$ Kg/m^3 and $c = 1500$ m/s approximately. Thus, the product of $\rho_0 c$ is of the order 10^2 for air and 10^6 for water. All the materials of Table (3.1) have $\rho_c c_c \approx 10^6$; thus $\alpha_n \to 0$ only in case of air. Therefore, the spheres made of the materials considered in Table (3.1) are dealt with as rigid or soft spheres depending on whether the medium surrounding them is air or water, respectively.

3.4.3 The Effect of Changing the Radius of the Sphere

It has been shown in Chapter 2 that more details appear in the backscattered spectrum if the radius of the sphere gets bigger keeping the pulse width constant. In addition, as the radius of the sphere becomes bigger, the average spacing of the spectral dips gets smaller [cf. Fig. (2.9)]. However, it is important to note that the backscattered spectrum of the soft sphere looks as that of the rigid sphere in the low frequency range (approximately up to 30 KHz). On the other hand, in the high frequency portion of the spectrum, we get more pronounced dips. The plots in Figs. (3.2), (3.3.a), and (3.3.b) show that the average spacing of the spectral dips in the low frequency range is almost identical for Mn and Pb spheres placed in water. However, the average spacing between the dips in the high frequency ranges are different. In Figs. (3.4.a-j), we provide spectra of AXW pulses scattered from spheres of different materials placed in water. To be able to extract information about the size of the sphere, we need to generate a "calibration" curve that relates the average spacing of the spectral dips calculated from the low frequency range to the radii of the spheres. In Fig. (3.5.a), we provide such calibration curves using the low frequency dip separations for four materials; specifically, Ti, Mn, Ni, and Mo. This figure shows that the calibration

curves for the four materials are very close to each other. Consequently, we can start with an arbitrary calibration curve that does not depend on the material. Such an arbitrary "radius calibration" curve is shown in Fig. (3.5.b). This curve is done using the average spacing of the spectral dips obtained from the low frequency range of the backscattered spectra of three different spheres having radii equal to 30, 40, and 50 mm. The spectra of the scattered fields for these radii are evaluated for $r = 150 \, \text{mm}$, $a = 15 \, \text{mm}$, $\rho_0 = 1 \cdot 0 \times 10^3 \, \text{Kg}/\text{m}^3$, $\rho_e = 7 \cdot 8 \times 10^3 \, \text{Kg}/\text{m}^3$, $c = 1500 \, \text{m}/\text{s}$, and $c_e = 3000 \, \text{m}/\text{s}$. The points are plotted using MS Excel and a trend line is drawn to give the mathematical equation $R = 1041.1 \left(\Delta k_{av} \right)^{-0.937}$ for the calibration curve. Tables (3.2.a-c) give the estimated radii for different materials as obtained from the aforementioned relation deduced from Fig. (3.5.b). Table (3.2.a) shows the estimated radii of the various scattering spheres from the information contained in the spectra of the different materials. The spectra are originally calculated for a sphere of size $R = 25$ mm. The estimated radii values, deduced from the simulated spectra when matched up to the calibration curve [cf. Fig. (3.5.b)], differ from the theoretical ones by less than 4% for all materials except Al that differs by 11%. This is because the backscattered spectrum of Aluminum does not contain enough details at low frequencies to calculate the average spacing of the spectral dips. On the other hand, Table (3.2.b) shows that for $R = 35$ mm the percentage error decreases to values below 2% for all materials except Al stays at 7%. Finally, for $R = 40$ mm all the materials have less than 2% error as shown in Table (3.2.c). The reason for this decrease in percentage error is due to the fact that as the radius of the sphere increase with respect to the pulse width more details appear in the entire backscattered spectrum. In all calculations, we have used $a = 15 \, \text{mm}$, $q = 1$ and $\xi = 2°$.

3.4.4 Effect of Changing the Density of the Material

The plots in Figs. (3.4.a-j) show the simulated backscattered spectra of different materials immersed in water for constant radius, and pulse width but at three different observation distances. From these figures, it is obvious that each material gives different amplitudes, however, the amplitudes are not only susceptible to the density of the material but also the radius of the sphere, observation distance, and the power of the received signal which is proportional to the power of the source. Thus, if we know the power of the source and the observation distance we can do a calibration between the density of the material and the amplitude of the backscattered spectrum at different radii. We propose that the relation between the amplitude and the density takes the form of $A \propto 1/\sqrt{\rho_e}$, where A is the amplitude and ρ_e is the density of the material of the sphere. In addition, we argue that the amplitude of the first peak in the spectrum yields the best results. Fig. (3.6) provides calibration curves relating the amplitudes of the first peaks in the backscattered spectra of four different materials (Ti, Mn, Ni, and Mo) to their densities; for radii of 30, 35 and 45 mm. The data are plotted using MS Excel and trend lines are drawn to give the mathematical form of these curves. For example the equation of the line at $R = 35\,\text{mm}$, $r = 150\,\text{mm}$, $a = 15\,\text{mm}$, $\rho = 1 \cdot 0 \times 10^3\,\text{Kg/m}^3$, and $c_e = 1500\,\text{m/s}$ is given by $1/\sqrt{\rho_e} = -0 \cdot 0228A + 0 \cdot 0603$. In Fig. (3.7), we present typical calibration curves between density and amplitude at different observation distances. The relationship between the amplitude and observation distance, shown in Fig. (3.8), is $A \propto 1/r$ as suggested by the trend lines of the MS Excel.

70

3.4.5 The Effect of Changing the Speed of Wave Propagation

In Sec. 3.4.3, we discussed the effect of changing the radius and we pointed out that varying the speed of wave propagation inside the sphere affects the average spacing of the spectral dips in the high frequency range. However, from Fig. (3.5.a) we can deduce that the speed has also a small effect on the low frequency range since the four curves do not overlap completely. Therefore, we recommend that the average spacing of the spectral dips of the whole back-scattered spectrum be calculated when doing the calibration curve for the speed of sound in the material. Fig. (3.9) provides a typical calibration curve for the average spacing of the spectral dips of the entire spectrum with the speed of wave propagation inside the sphere for different radii. Again, we have used the back-scattered spectra of Ti, Mn, Ni, and Mo with the same values of parameters used in Sec. 3.4.4. We plotted the average spacing of the spectral dips obtained from the whole spectrum against the speed of propagation inside the spheres, the best fit of the points suggested the following mathematical equation for the $R = 35\,\text{mm}$ line; $c_c = 35 \cdot 225(\Delta k'_{\text{ave}}) + 606 \cdot 45$. The average spacing of the spectral dips increases linearly with the speed of propagation inside the spheres.

3.4.6 Size and Material Identification

We shall consider specific numerical calculations to present a recipe for identifying the size and material of an unknown sphere using the back-scattered spectra of an acoustical X-wave. First, we shall find the average spacing of the spectral dips at low frequencies Δk_{av} (up to 30 KHz), the amplitude of the first peak A, and the average

spacing of the spectral dips of the whole spectrum $\Delta k'_{av}$. Subsequently, we insert the value Δk_{av} in the relation obtained from the arbitrary "radius calibration" curve to obtain an estimate for the radius of the scattering sphere. Knowing A and the predicted radius, we use the appropriate calibration curve of the density versus the amplitude to find the density of the material. Similarly, using the predicted radius and $\Delta k'_{av}$ we find the speed from the appropriate calibration curve. Let us consider the simulated backscattered spectra of the different materials shown in Figs. (3.4.e-j); one should recall, in the meanwhile that the four figures given in Figs. (3.4.a-d) have been used to generate the calibration curves. From the spectra in Figs. (3.4.e-j), we calculate Δk_{av}, A, and $\Delta k'_{av}$. Using Δk_{av} and the "radius calibration" curve provided in Fig. (3.5.b), the radii of the spheres are found to be about 35 mm as shown in Table (3.2.b). Estimated values agree with theoretical ones with a variation of $\pm 2\%$ for all materials except Al. Then, we find the density of the materials using A and the calibration curve of the density with the amplitude of the first peak at $R = 35$ mm that is given in Fig. (3.6). The results are tabulated in Table (3.3) and they agree with the theoretical values within a margin of error of $\pm 5\%$ for all materials except Al, which has a percentage error of 9%. Finally, we find the speed of the sound in the material of the sphere using $\Delta k'_{av}$ with the calibration curve for the speed versus the average spacing of the spectral dips for the entire spectrum given in Fig. (3.9) at $R = 35$ mm. The results are shown in Table (3.4) and they agree with the theoretical values within an error margin of 2% for all materials except Pb that has an error of 4.6%.

3.5 NUMERICAL RESULTS DUE TO INCIDENCE OFF CENTER

We already know from Sec. 2.6 that even if the pulse is incident off center, and detected at an angle $\theta = \left((\pi/2) + \cos^{-1}(x_0/r)\right)$, we can still have enough details in the backscattered spectrum from which we can extract information about the spheres

We shall consider the same example mentioned in Sec. 3.4.6 but in this case both the source and detector are displaced for two different distances $x_0 = 15\,\text{mm}$ and $x_0 = 45\,\text{mm}$; i.e. the pulse is once displaced from the center but is still inside the sphere then the peak of the pulse is assumed to pass outside the sphere. The obtained data are tabulated at $x_0 = 15\,\text{mm}$ in Tables (3.5.a), (3.6.a) and (3.7.a), for the radius, for the density and for the speed, respectively. While Tables (3.5.b), (3.6.b), (3.7.b) provide estimates of the radius, density and speed, respectively, when the peak of the X-wave is displaced at $x_0 = 45\,\text{mm}$. Comparing Tables (3.5.a) and (3.5.b), we find that the accuracy in estimating the radius, using Fig. (3.5.b) is almost the same, approximately 2% for all materials except for Al that increased slightly from 7% to 8%. Thus, for a pulse incident on center or off center but inside the sphere, the accuracy of estimating the radius is almost the same. On the other hand, the error increases to 4%, for all materials except Al that has an error of 12%, when the pulse is incident outside the sphere. As for the density and the speed, the accuracy of the results remains the same independent of whether the pulse is incident on center or off center for both cases when the peak passes through or outside the sphere.

73

3.6 CONCLUDING REMARKS

In this chapter, we studied the scattering of AXW by soft spheres. We showed that in order to identify the material as soft or rigid, we have to consider the medium surrounding the scatterers. In addition, we found that the backscattered spectrum is function of the observation distance and the power of the detected signal, which is proportional to that of the source. Thus, if we have a source of known power, we can identify the size of the scattering sphere from an arbitrary calibration curve relating the low frequency average spacing of the spectral dips to the radius of the sphere. Subsequently, we can identify the material using the amplitude of the first peak in the spectra and the average spacing of the spectral dips in the whole spectrum. These two pieces of information can help us determine the density and the wave speed of the material of the scattering sphere. We found that our evaluations remain valid with acceptable estimates for the size and material of the scatterer if the pulse is incident off center.
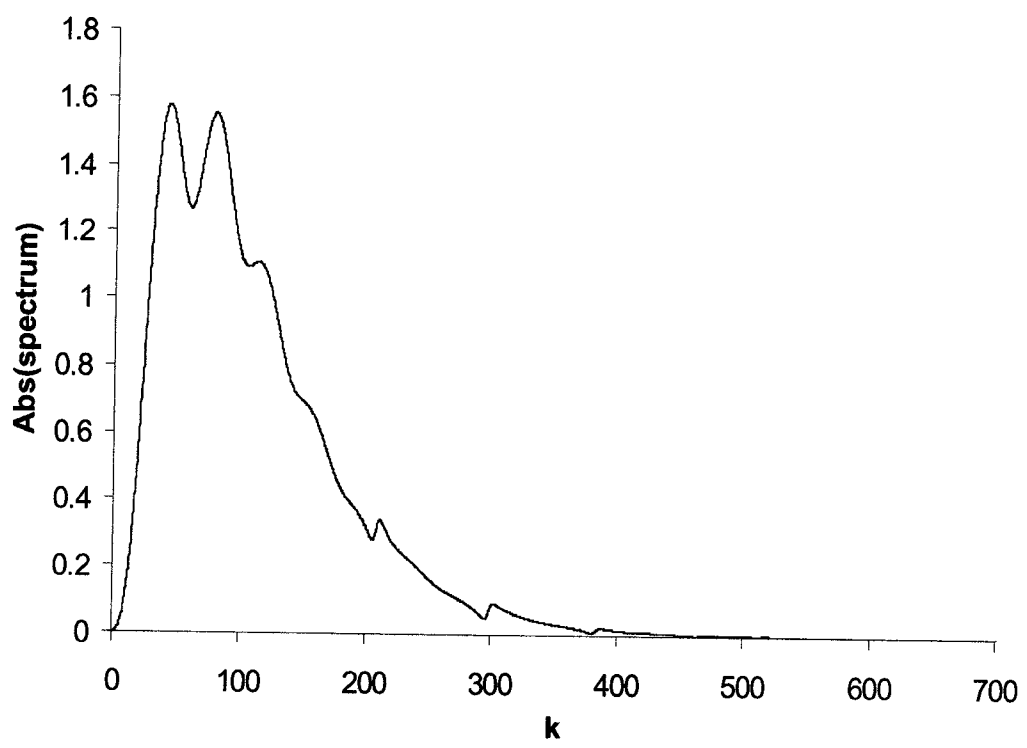
Figure 3.1.a Backscattered spectrum by a soft sphere for $R = 30$ mm, $r = 150$ mm, $\rho_0 = 1 \cdot 0 \times 10^3$ Kg/m^3, $c = 1500$ m/s, $c_e = 3000$ m/s, $\rho_e = 7 \cdot 8 \times 10^3$ Kg/m^3, $a = 20$ mm and $\theta = \pi$ due to an AXW pulse incident on center.

75
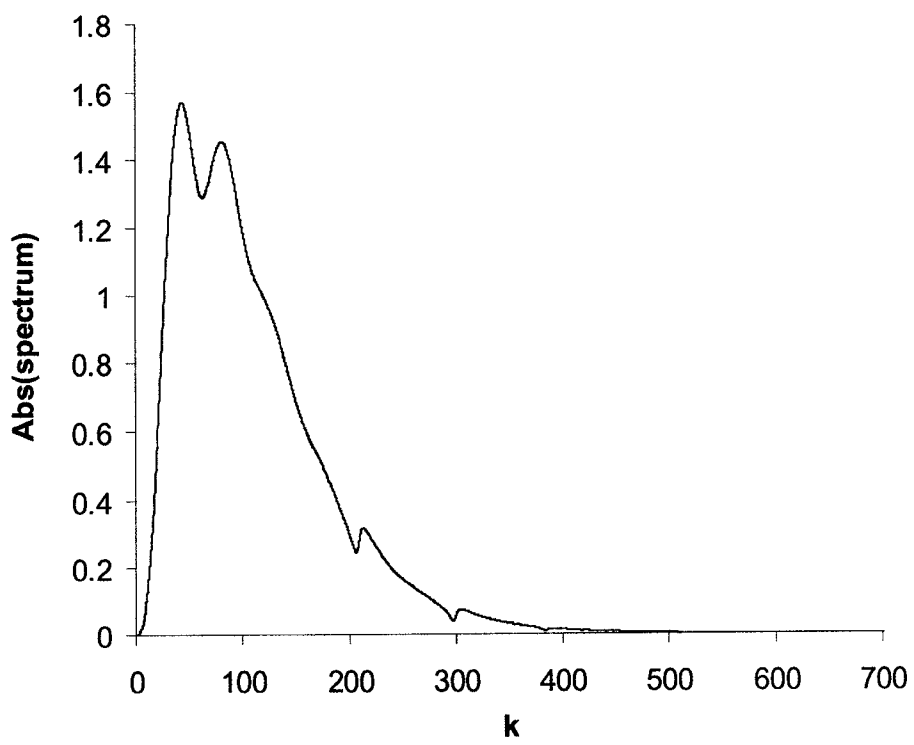
Figure 3.1.b Scattered spectrum by a soft sphere for $R = 30\,\text{mm}$, $r = 150\,\text{mm}$, $c = 1500\,\text{m/s}$, $\rho_0 = 1\cdot0\times10^3\,\text{Kg/m}^3$, $c_e = 3000\,\text{m/s}$, $\rho_e = 7\cdot8\times10^3\,\text{Kg/m}^3$, $a = 20\,\text{mm}$ and $\theta = 5\pi/6$ due to an AXW pulse incident on center.
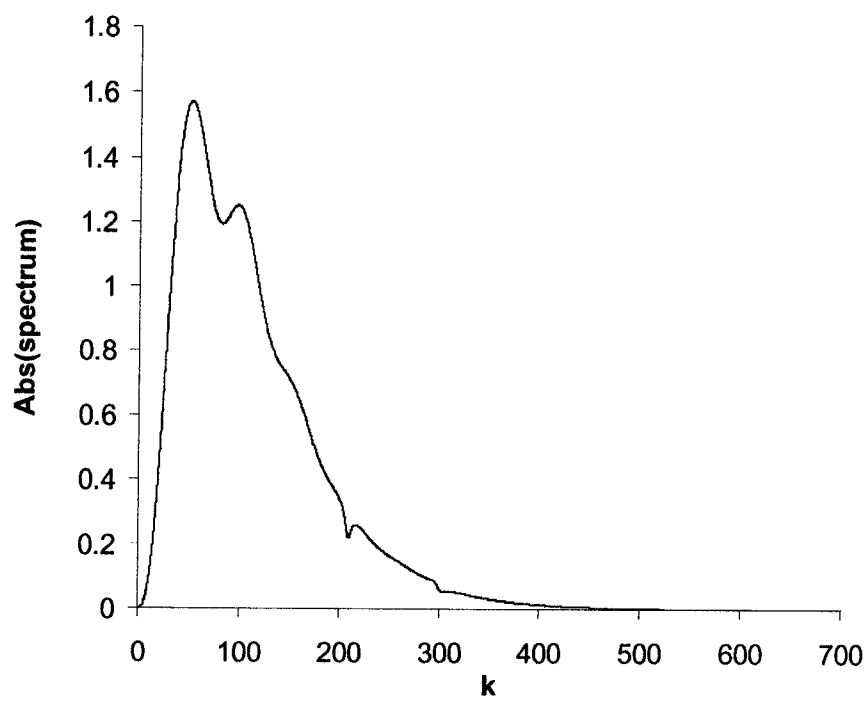
Figure 3.1.c Scattered spectrum by a soft sphere for $R = 30\,\text{mm}$, $r = 150\,\text{mm}$, $c = 1500\,\text{m/s}$, $\rho_0 = 1.0 \times 10^3\,\text{Kg/m}^3$, $c_e = 3000\,\text{m/s}$, $\rho_e = 7.8 \times 10^3\,\text{Kg/m}^3$, $a = 20\,\text{mm}$, and $\theta = 2\pi/3$ due to an AXW pulse incident on center.
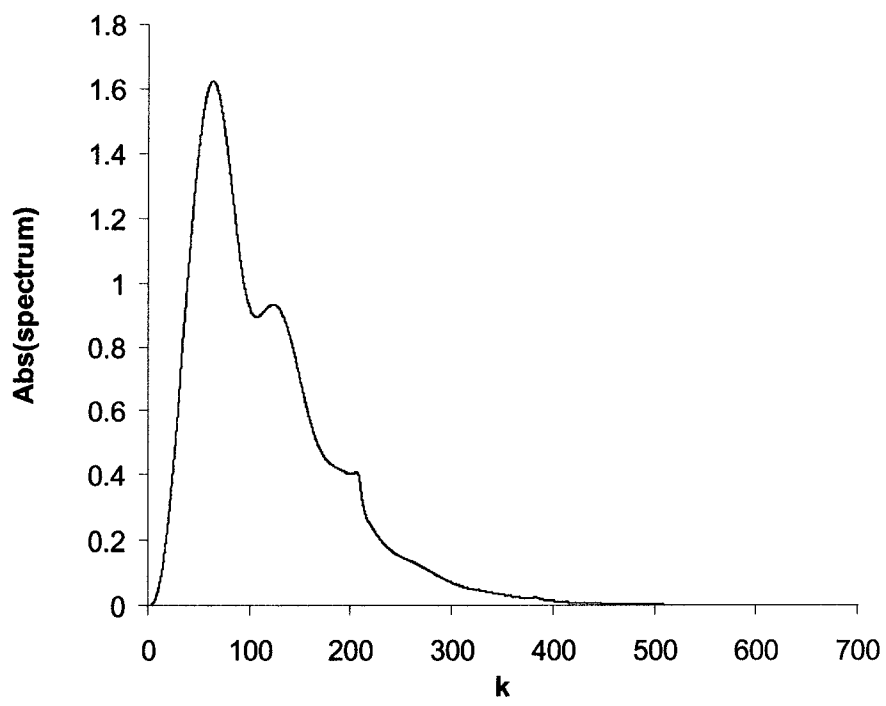
Figure 3.1.d Scattered spectrum by a soft sphere for $R = 30\,\text{mm}$, $r = 150\,\text{mm}$, $c = 1500\,\text{m/s}$, $\rho_0 = 1.0 \times 10^3\,\text{Kg/m}^3$, $c_e = 3000\,\text{m/s}$, $\rho_e = 7.8 \times 10^3\,\text{Kg/m}^3$, $a = 20\,\text{mm}$, and $\theta = \pi/2$ due to an AXW pulse incident on center.
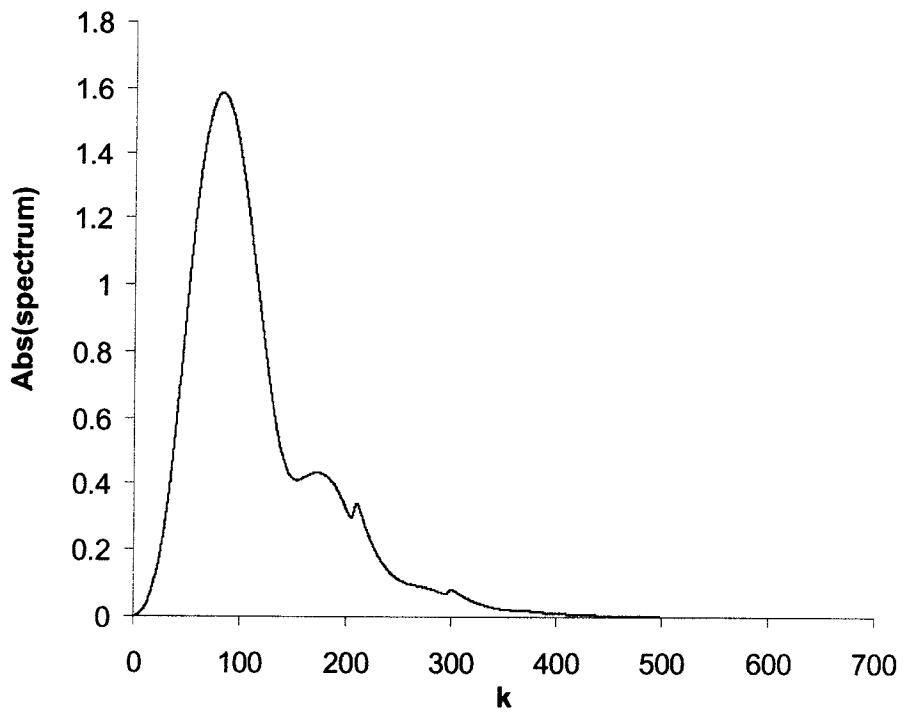
Figure 3.1.e Scattered spectrum by a soft sphere for $R = 30\,\text{mm}$, $r = 150\,\text{mm}$, $c = 1500\,\text{m/s}$, $\rho_0 = 1 \cdot 0 \times 10^3\,\text{Kg/m}^3$, $c_e = 3000\,\text{m/s}$, $\rho_e = 7 \cdot 8 \times 10^3\,\text{Kg/m}^3$, $a = 20\,\text{mm}$, and $\theta = \pi/3$ due to an AXW pulse incident on center.
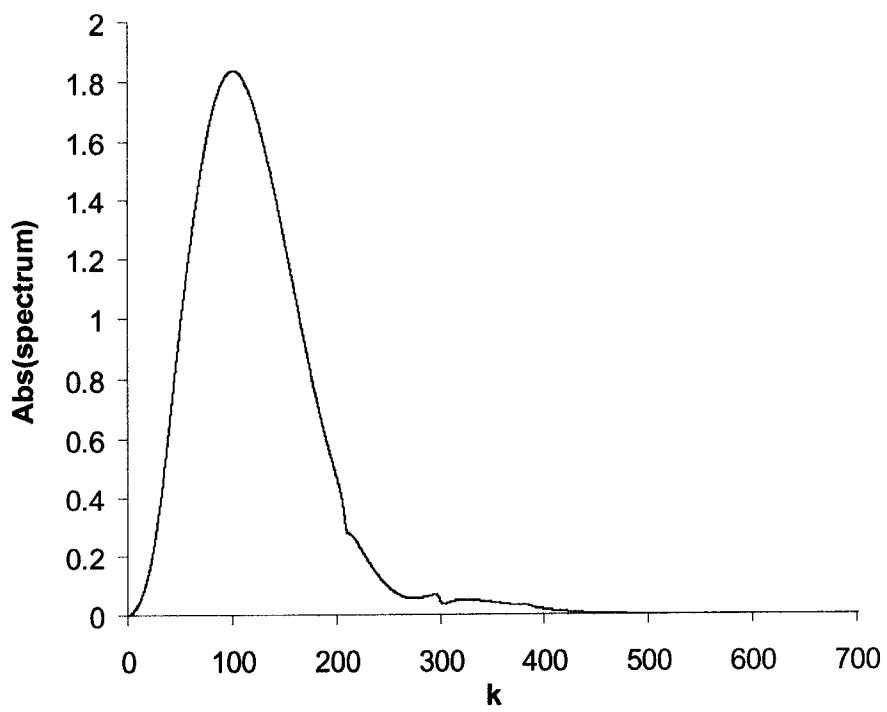
Figure 3.1.f Scattered spectrum by a soft sphere for $R = 30\,\text{mm}$, $r = 150\,\text{mm}$, $c = 1500\,\text{m/s}$, $\rho_0 = 1\cdot 0\times 10^3\,\text{Kg/m}^3$, $c_e = 3000\,\text{m/s}$, $\rho_e = 7\cdot 8\times 10^3\,\text{Kg/m}^3$, $a = 20\,\text{mm}$, and $\theta = \pi/6$ due to an AXW pulse incident on center.
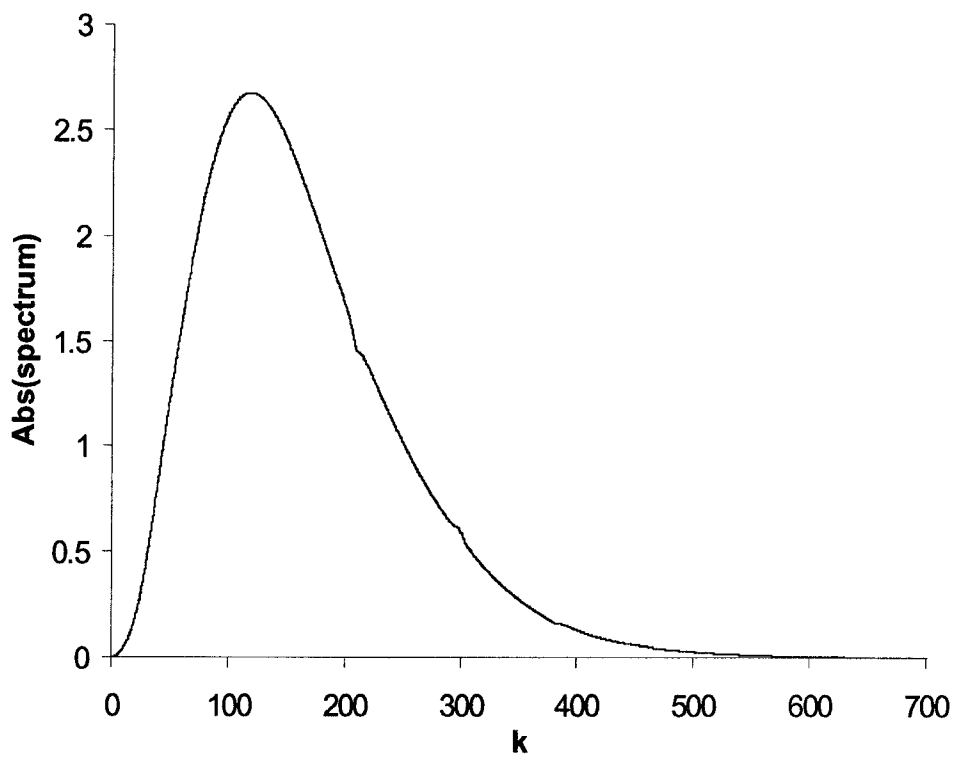
Figure 3.1.g Forward scattered spectrum by a soft sphere for $R = 30\,\text{mm}$, $r = 150\,\text{mm}$, $\rho_0 = 1 \cdot 0 \times 10^3\,\text{Kg}/\text{m}^3$ $c = 1500\,\text{m}/\text{s}$, $c_e = 3000\,\text{m}/\text{s}$, $\rho_e = 7 \cdot 8 \times 10^3\,\text{Kg}/\text{m}^3$, $a = 20\,\text{mm}$, and $\theta = 0$ due to an AXW pulse incident on center.

81
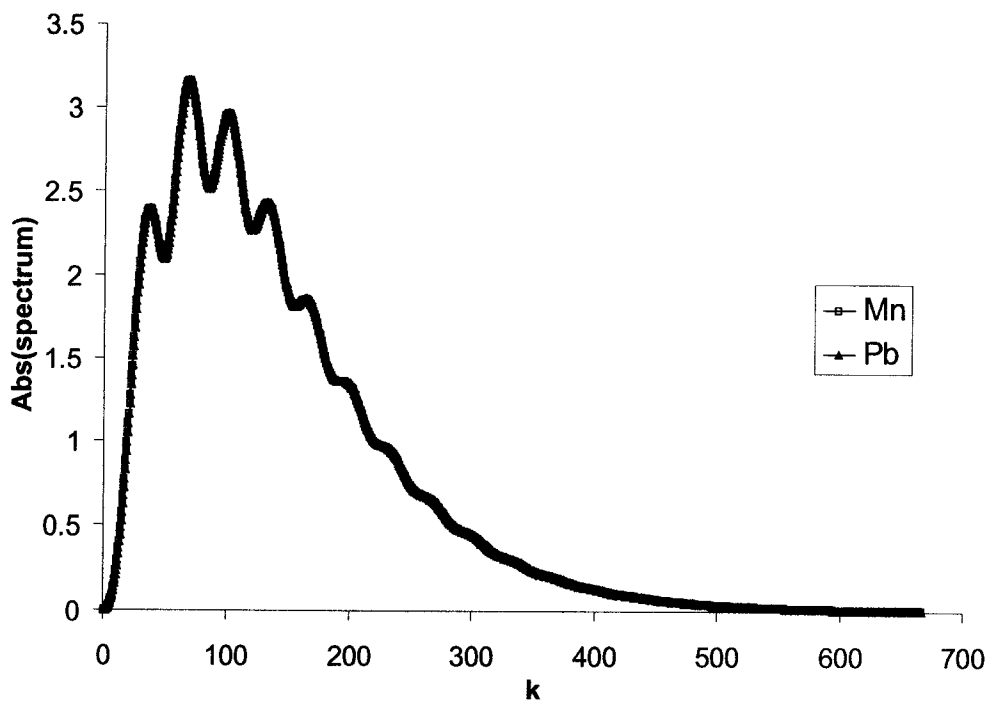
Figure 3.2 Backscattered spectra by Mn and Pb spheres in air for $R = 35\,\text{mm}$, $r = 150\,\text{mm}$, $a = 15\,\text{mm}$, $c = 350\,\text{m/s}$, and $\rho_0 = 1 \cdot 2\,\text{Kg/m}^3$ due to an AXW pulse incident on center.
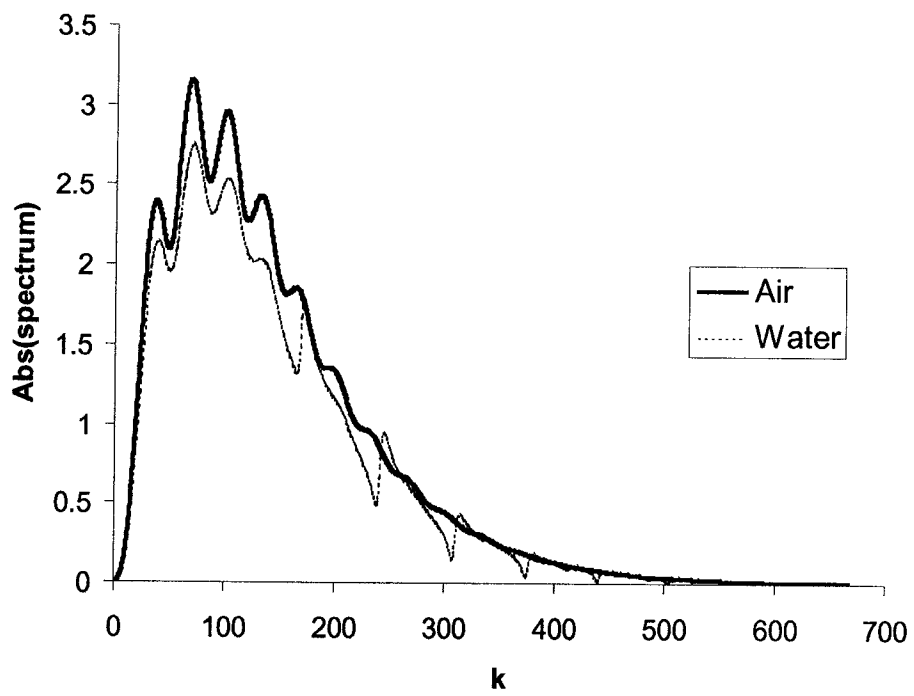
Figure 3.3.a Backscattered spectra by a Mn sphere placed in air and water for $R = 35\,\text{mm}$, $r = 150\,\text{mm}$, $c_e = 2824 \cdot 64\,\text{m/s}$, $\rho_e = 7 \cdot 47 \times 10^3\,\text{Kg/m}^3$, and $a = 15\,\text{mm}$ due to an AXW pulse incident on center.
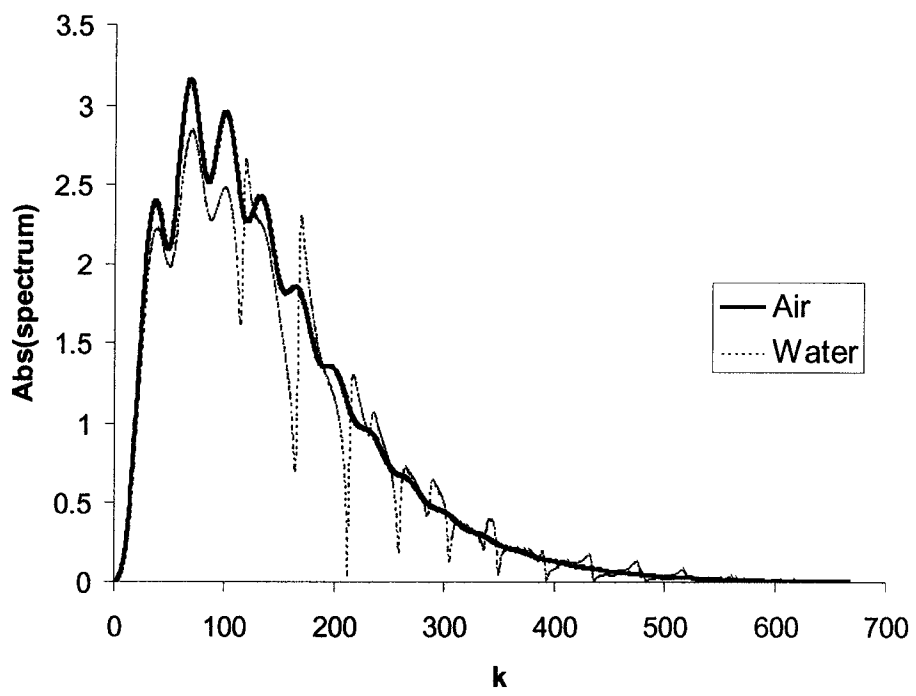
Figure 3.3.b Backscattered spectra by a Pb sphere placed in air and water for $R = 35\,\text{mm}$, $r = 150\,\text{mm}$, $c_e = 1947 \cdot 28\,\text{m/s}$, $\rho_e = 1 \cdot 13 \times 10^4\,\text{Kg/m}^3$, and $a = 15\,\text{mm}$ due to an AXW pulse incident on center.
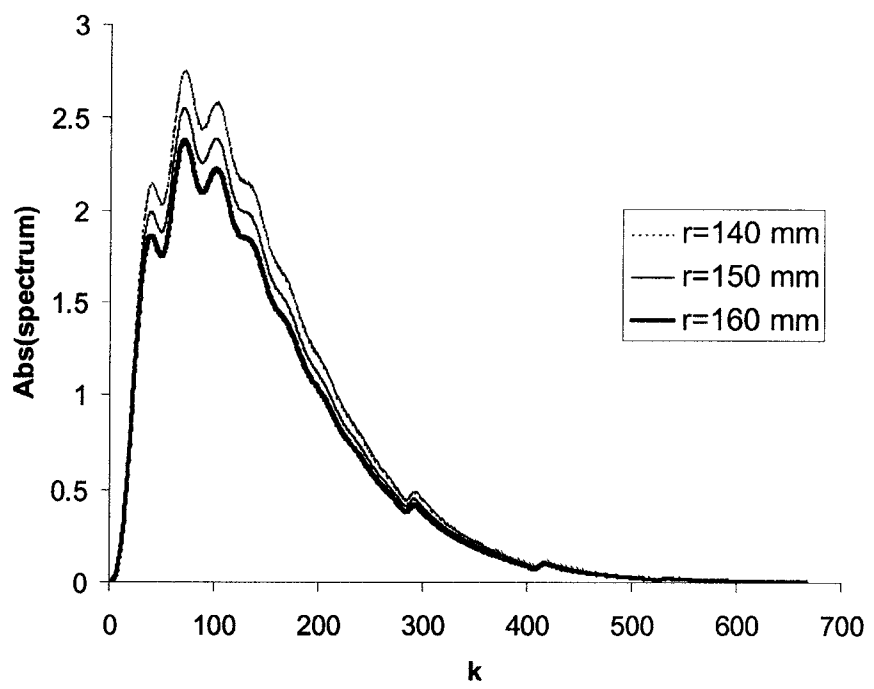
Figure 3.4.a Backscattered spectra by a Ti sphere for $R = 35\,\text{mm}$, $\rho_0 = 1 \cdot 0 \times 10^3\,\text{Kg/m}^3$, $c = 1500\,\text{m/s}$, $c_e = 4827 \cdot 40$ m/s, $\rho_e = 4 \cdot 51 \times 10^3\,\text{Kg/m}^3$, $a = 15\,\text{mm}$, and different values of r, due to an AXW pulse incident on center.
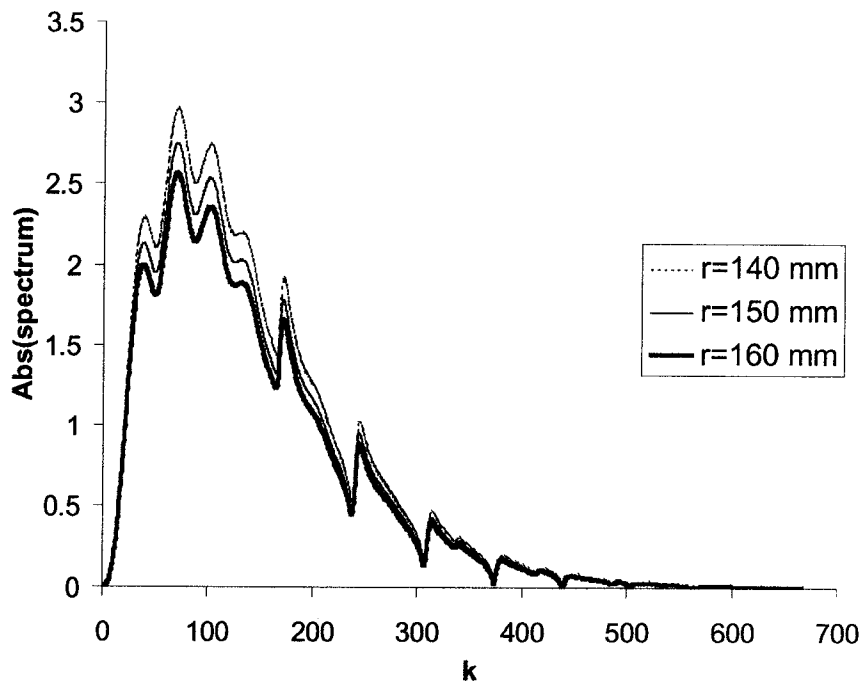
Figure 3.4.b Backscattered spectra by a Mn sphere for $R = 35\,\text{mm}$, $\rho_0 = 1\cdot 0\times 10^3\,\text{Kg}/\text{m}^3$, $c = 1500\,\text{m}/\text{s}$, $c_e = 2824\cdot 64$ m/s, $\rho_e = 7\cdot 47\times 10^3\,\text{Kg}/\text{m}^3$, $a = 15\,\text{mm}$, and different values of r, due to an AXW pulse incident on center.
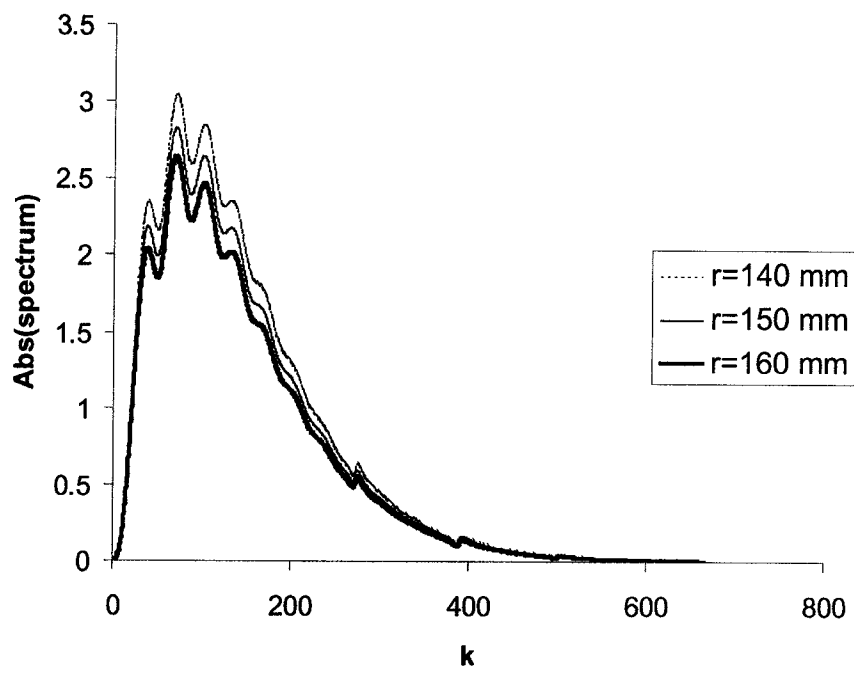
Figure 3.4.c Backscattered spectra by a Ni sphere for $R = 35\,\text{mm}$, $\rho_0 = 1 \cdot 0 \times 10^3\,\text{Kg}/\text{m}^3$, $c = 1500\,\text{m}/\text{s}$, $c_e = 4568 \cdot 96$ m/s, $\rho_e = 8 \cdot 91 \times 10^3\,\text{Kg}/\text{m}^3$, $a = 15\,\text{mm}$, and different values of r, due to an AXW pulse incident on center.
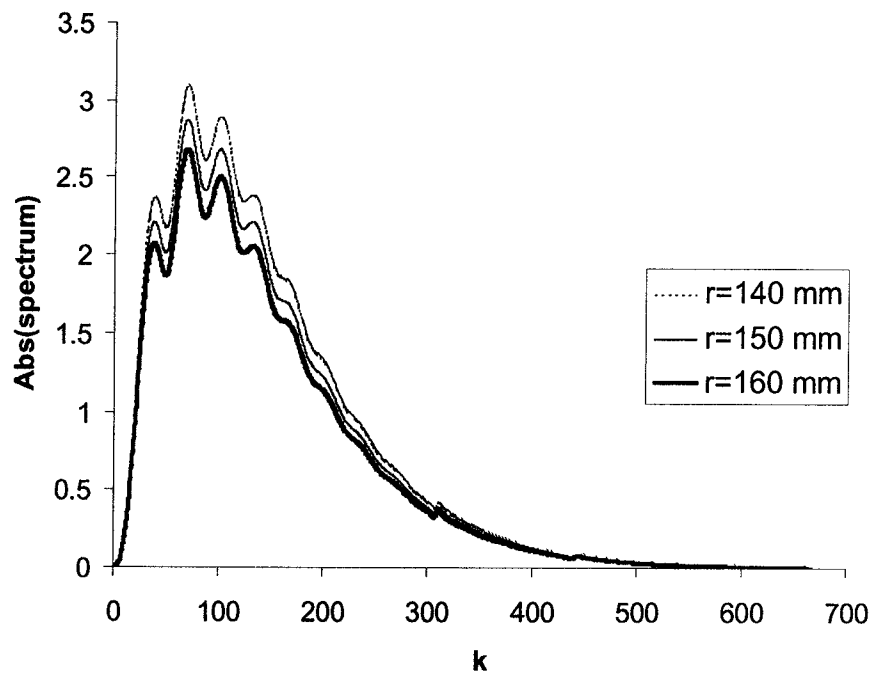
Figure 3.4.d Backscattered spectra by a Mo sphere for $R = 35\,\mathrm{mm}$, $\rho_0 = 1\cdot 0\times 10^3\,\mathrm{Kg/m^3}$, $c = 1500\,\mathrm{m/s}$, $c_e = 5163\cdot 66$ $\mathrm{m/s}$, $\rho_e = 1\cdot 02\times 10^3\,\mathrm{Kg/m^3}$, $a = 15\,\mathrm{mm}$, and different values of r, due to an AXW pulse incident on center.
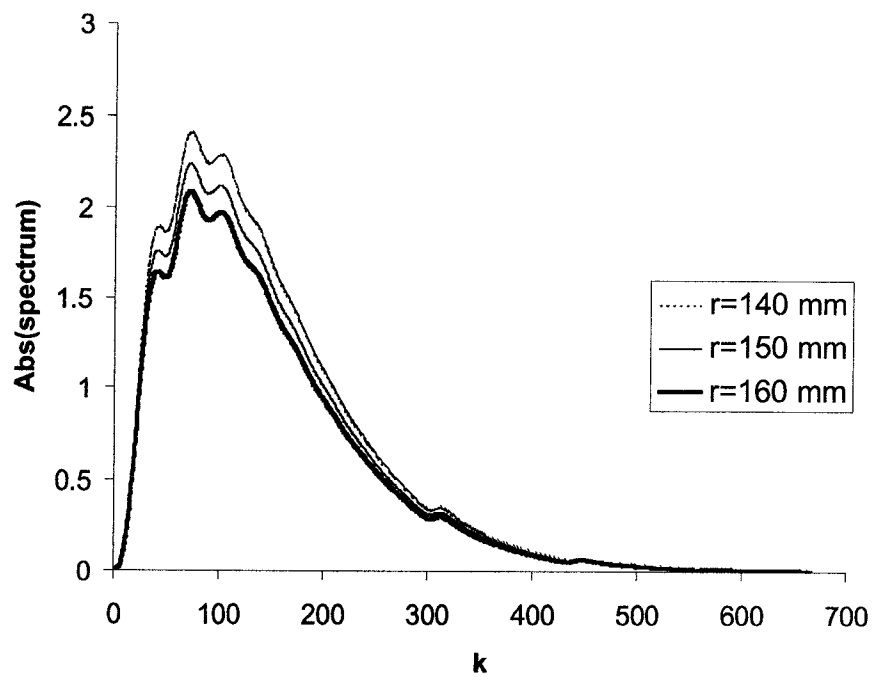
Figure 3.4.e Backscattered spectra by an Al sphere for $R = 35\,\text{mm}$, $\rho_0 = 1\cdot0\times10^3\,\text{Kg}/\text{m}^3$, $c = 1500\,\text{m}/\text{s}$, $c_e = 5171\cdot14$ m/s, $\rho_e = 2\cdot7\times10^3\,\text{Kg}/\text{m}^3$, $a = 15\,\text{mm}$, and different values of r, due to an AXW pulse incident on center.
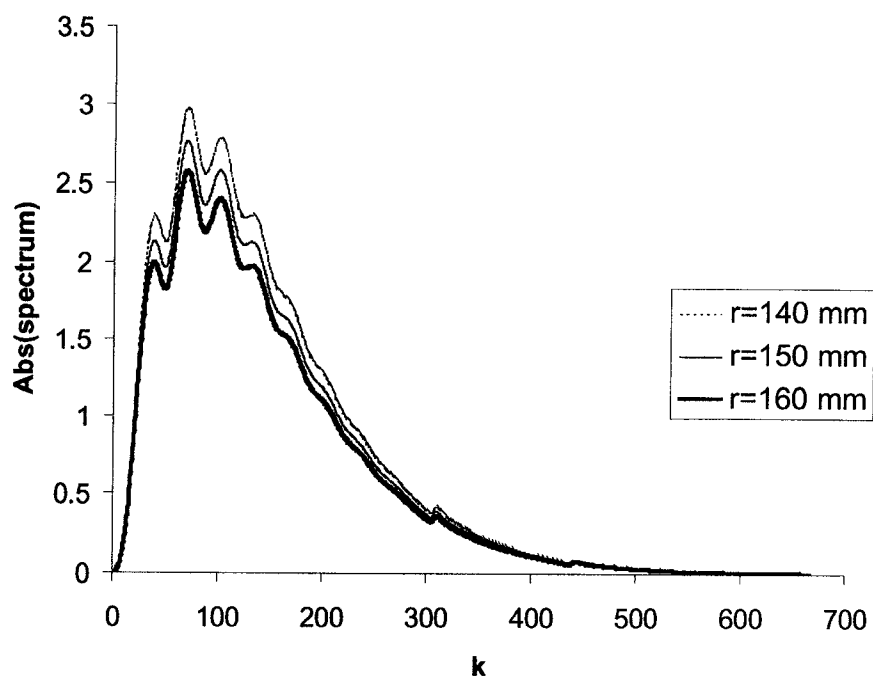
Figure 3.4.f Backscattered spectra by a Cr sphere for $R = 35\,\text{mm}$, $\rho_0 = 1 \cdot 0 \times 10^3\,\text{Kg}/\text{m}^3$, $c = 1500\,\text{m}/\text{s}$, $c_e = 5141 \cdot 93$ m/s, $\rho_e = 7 \cdot 19 \times 10^3\,\text{Kg}/\text{m}^3$, $a = 15\,\text{mm}$, and different values of r, due to an AXW pulse incident on center.
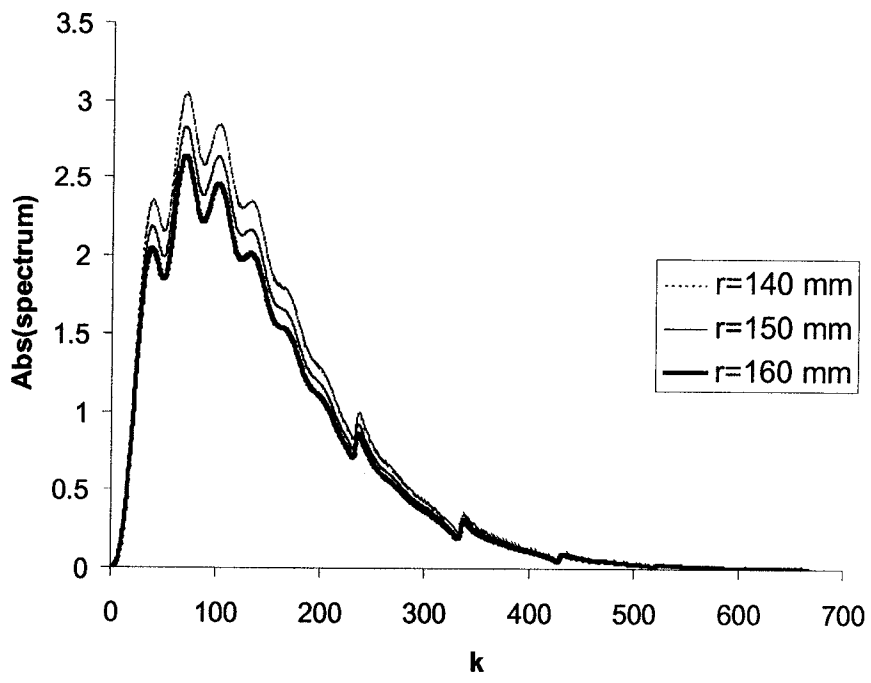
Figure 3.4.g Backscattered spectra by a Cu sphere for $R = 35\,\text{mm}$, $\rho_0 = 1 \cdot 0 \times 10^3 \, \text{Kg}/\text{m}^3$, $c = 1500\,\text{m/s}$, $c_e = 3916 \cdot 83$ m/s, $\rho_e = 8 \cdot 93 \times 10^3 \, \text{Kg}/\text{m}^3$, $a = 15\,\text{mm}$, and different values of r, due to an AXW pulse incident on center.
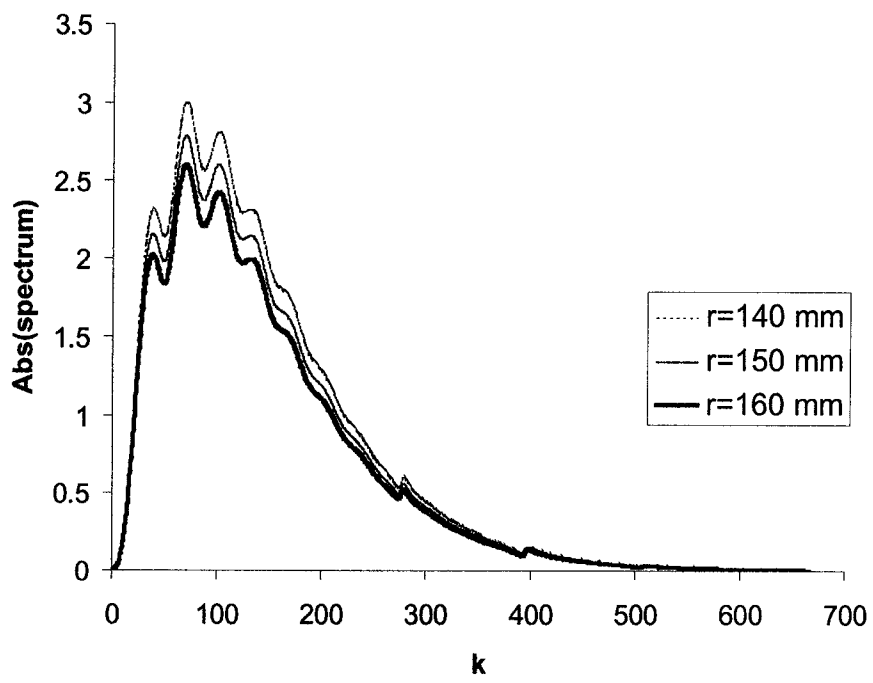
Figure 3.4.h Backscattered spectra by a Fe sphere for $R = 35\,\text{mm}$, $\rho_0 = 1\cdot 0 \times 10^3\,\text{Kg}/\text{m}^3$, $c = 1500\,\text{m}/\text{s}$, $c_e = 4624\cdot 39$ m/s, $\rho_e = 7\cdot 87 \times 10^3\,\text{Kg}/\text{m}^3$, $a = 15\,\text{mm}$, and different values of r, due to an AXW pulse incident on center.

92
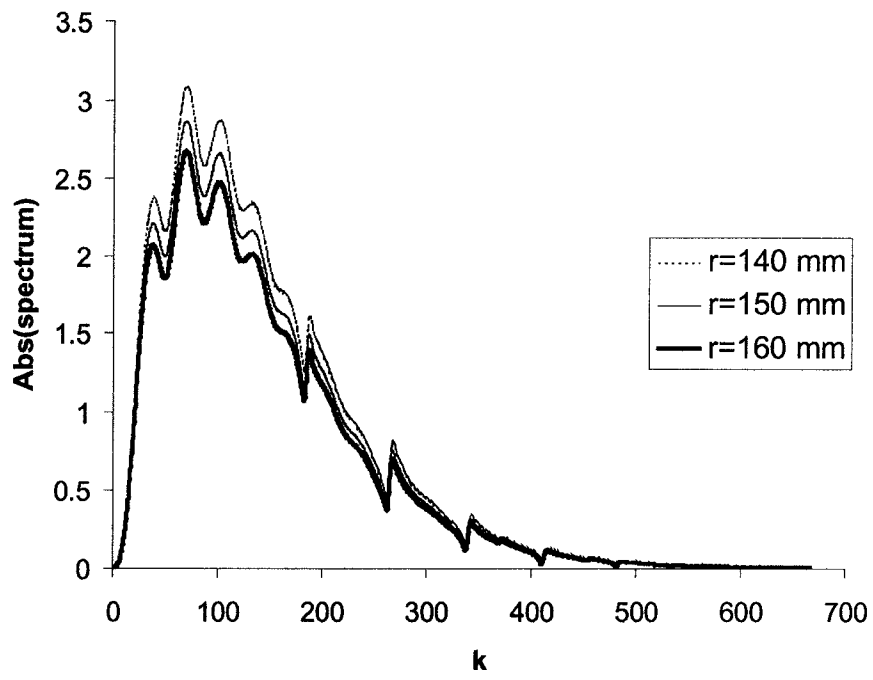
Figure 3.4.j Backscattered spectra by an Ag sphere for $R = 35\,\text{mm}$, $\rho_0 = 1 \cdot 0 \times 10^3\,\text{Kg/m}^3$, $c = 1500\,\text{m/s}$, $c_e = 3096 \cdot 85$ m/s, $\rho_e = 1 \cdot 05 \times 10^4\,\text{Kg/m}^3$, $a = 15\,\text{mm}$, and different values of r, due to an AXW pulse incident on center.
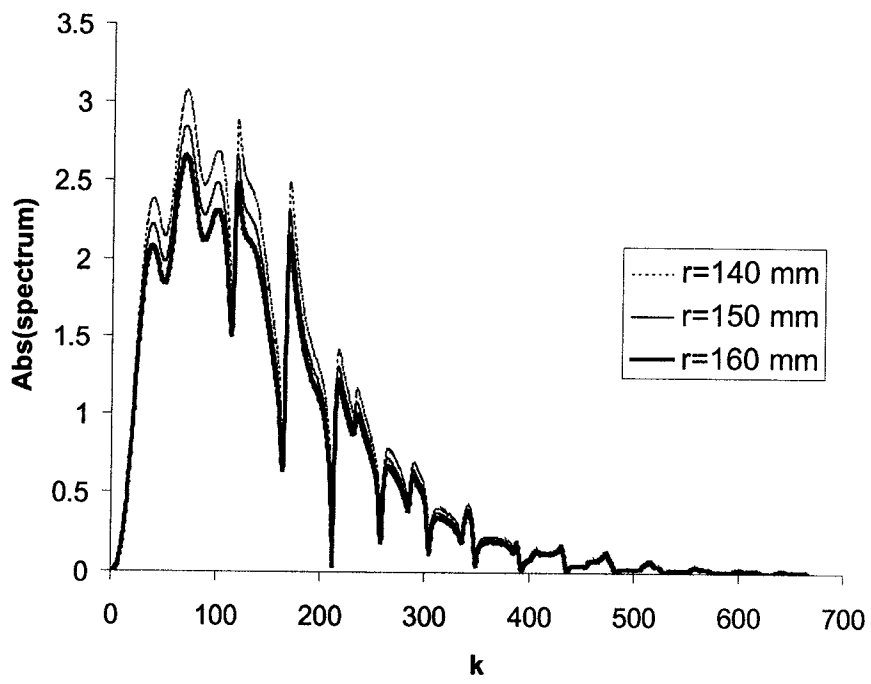
Figure 3.4.i Backscattered spectra by a Pb sphere for $R = 35\,\text{mm}$, $\rho_0 = 1 \cdot 0 \times 10^3\,\text{Kg}/\text{m}^3$, $c = 1500\,\text{m}/\text{s}$, $c_e = 1947 \cdot 28$ m/s, $\rho_e = 1 \cdot 13 \times 10^4\,\text{Kg}/\text{m}^3$, $a = 15\,\text{mm}$, and different values of r, due to an AXW pulse incident on center.
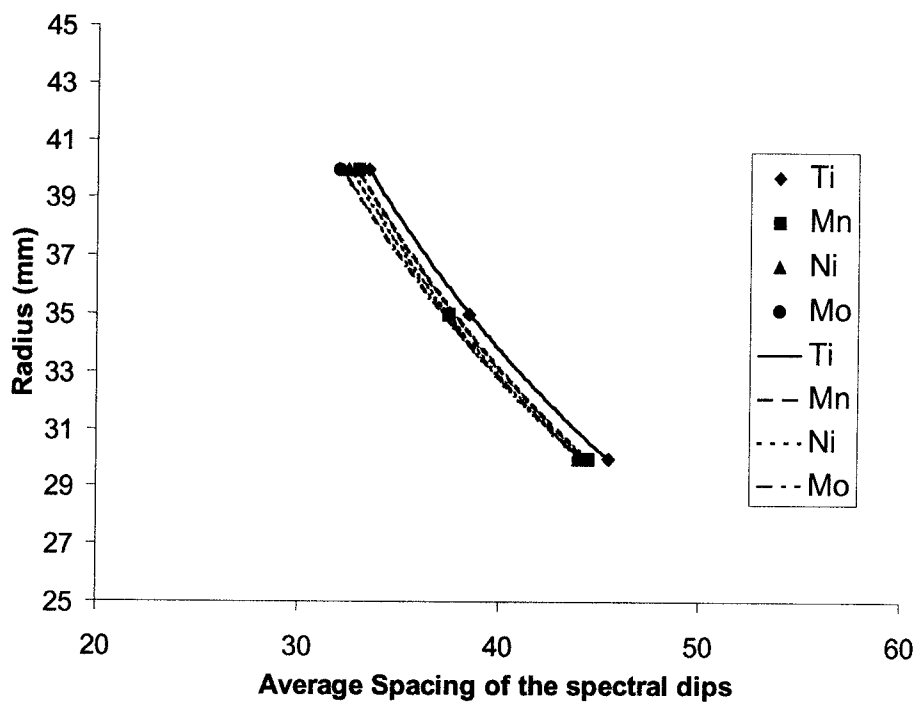
Figure 3.5.a Calibration curves relating the radius of the sphere to the average spacing of the spectral dips by different materials: Ti, Mn, Ni, and Mo, immersed in water for $r = 150\,\text{mm}$, $a = 15\,\text{mm}$.
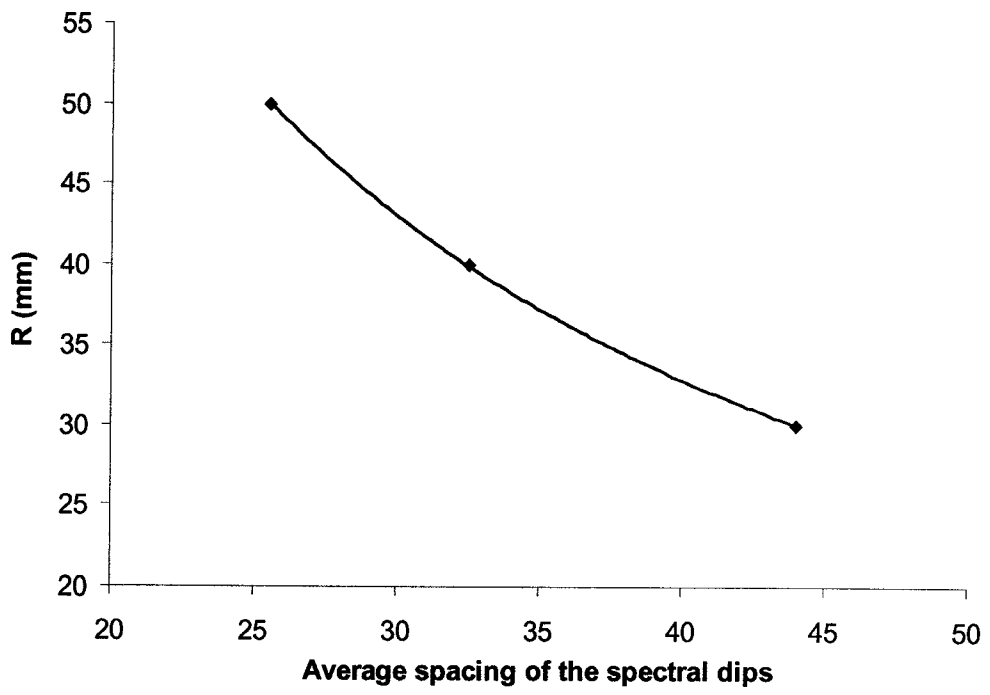
Figure 3.5.b Calibration curve between the radius of the sphere and average spacing of the spectral dips of the backscattered spectrum for $r = 150$ mm, $\rho_0 = 1\cdot0\times10^3$ Kg/m³, $c = 1500$ m/s, $\rho_e = 7\cdot8\times10^3$ Kg/m³, $c_e = 3000$ m/s, and $a = 15$ mm.
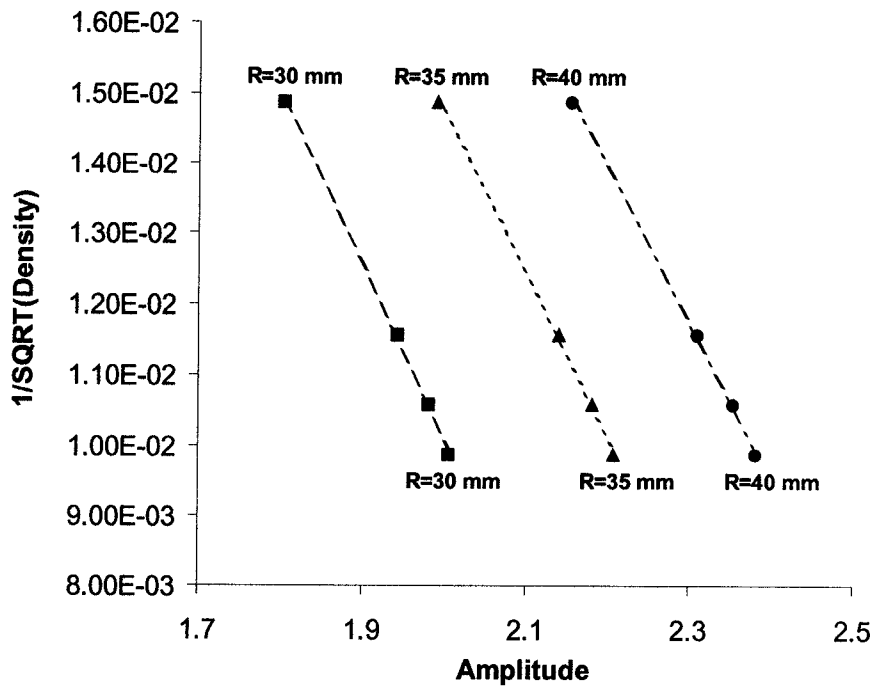
Figure 3.6 Calibration curves relating the density of the material to the amplitude of the backscattered spectrum for different radii, $r = 150\,\text{mm}$, $\rho_0 = 1 \cdot 0 \times 10^3\,\text{Kg}/\text{m}^3$, $c = 1500\,\text{m}/\text{s}$, and $a = 15\,\text{mm}$.

97
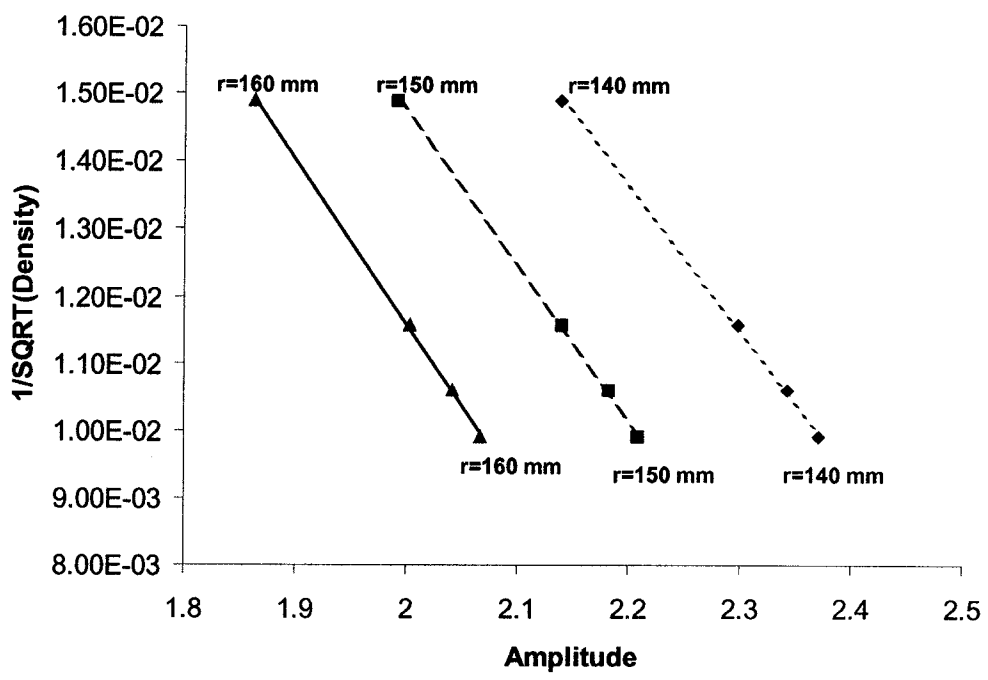
Figure 3.7 Calibration curves relating the density of the material to the amplitude of the backscattered spectrum for different observation distances, $R = 35\,\text{mm}$, $\rho_0 = 1\cdot0\times10^3\,\text{Kg}/\text{m}^3$, $c = 1500\,\text{m}/\text{s}$, and $a = 15\,\text{mm}$.
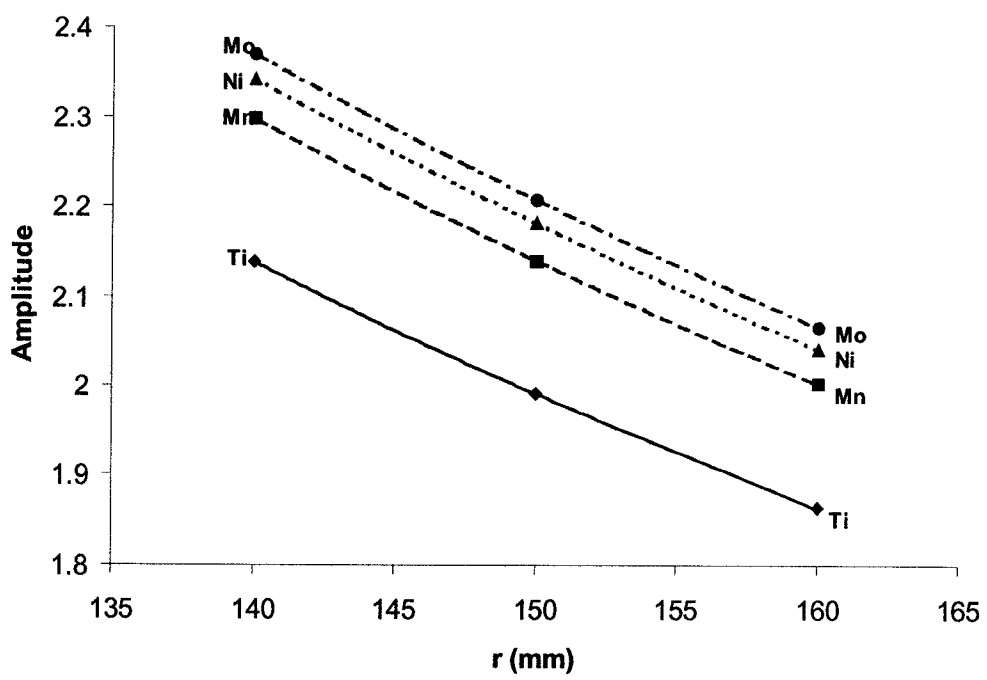
Figure 3.8 Calibration curves relating the amplitude of the backscattered spectrum to the observation distance for different materials: Ti, Mn, Ni, and Mo, immersed in water for $R = 35$ mm, and $a = 15$ mm.
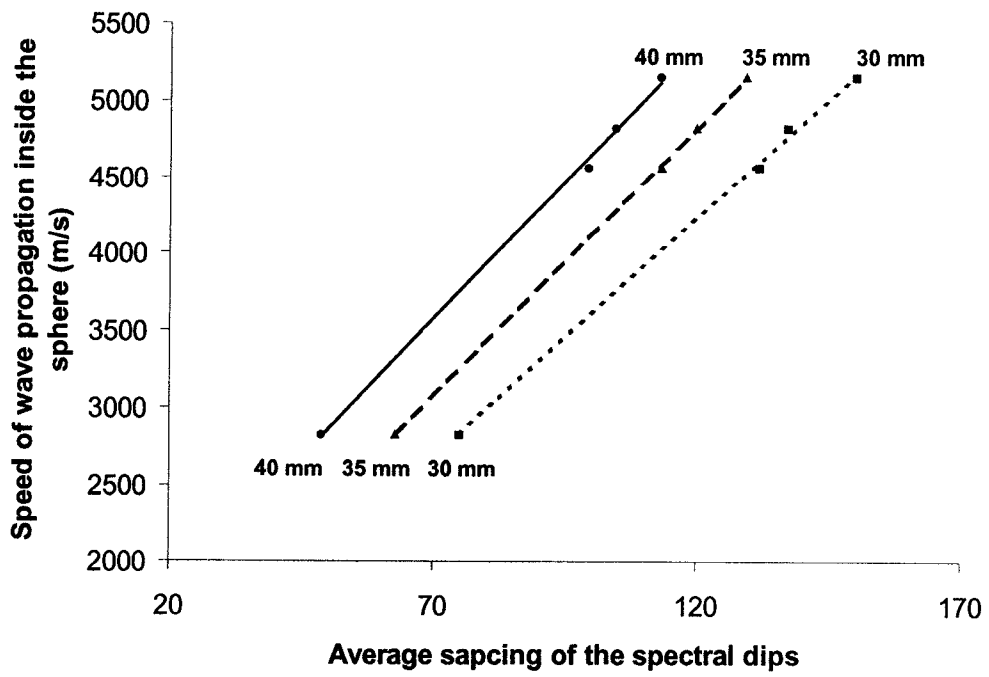
Figure 3.9 Calibration curves relating the speed of wave propagation inside of the sphere to the average spacing of the spectral dips of the backscattered spectrum for different radii, $r = 150\,\text{mm}$, $\rho_0 = 1 \cdot 0 \times 10^3\ \text{Kg}/\text{m}^3$, $c = 1500\ \text{m}/\text{s}$, and $a = 15\,\text{mm}$.

Material	Bulk Modulus (B) 10^{11} N/m^2	Density (ρ_e) 10^3 Kg/m^3	$c_e = \sqrt{B/\rho_e}$ (m/s)
Titanium	1.051	4.51	4827.40
Manganese	0.596	7.47	2824.64
Nickel	1.860	8.91	4568.96
Molybdenum	2.725	10.22	5163.66
Aluminum	0.722	2.70	5171.14
Chromium	1.901	7.19	5141.93
Copper	1.370	8.93	3916.83
Iron	1.683	7.87	4624.39
Lead	0.430	11.34	1947.28
Silver	1.007	10.50	3096.85

Table 3.1   Tabulated bulk modulus, density, and the calculated speed of sound propagation in different materials [86].

101

Material	Average Spacing of Spectral Dips	Estimated Radius (mm)	Actual Radius (mm)	% Error
Aluminum	59.00	22.25	25.00	11.00
Chromium	54.50	24.09	25.00	3.64
Copper	53.50	24.55	25.00	1.81
Iron	54.00	24.32	25.00	2.73
Lead	53.50	24.55	25.00	1.81
Silver	53.00	24.78	25.00	0.89

Table 3.2.a   Comparison between the estimated and actual radii of the spheres as have been calculated from the average spacing of the spectral dips of the simulated backscattered spectra obtained for different materials due to incidence on center.

Material	Average Spacing of Spectral Dips	Estimated Radius (mm)	Actual Radius (mm)	% Error
Aluminum	40.50	32.45	35.00	7.29
Chromium	37.50	35.06	35.00	0.17
Copper	37.25	35.29	35.00	0.83
Iron	37.50	35.06	35.00	0.17
Lead	37.50	35.06	35.00	0.17
Silver	37.00	35.53	35.00	1.51

Table 3.2.b Comparison between the estimated and actual radii of the spheres as have been calculated from the average spacing of the spectral dips of the simulated backscattered spectra obtained for different materials due to incidence on center.

Material	Average Spacing of Spectral Dips	Estimated Radius (mm)	Actual Radius (mm)	% Error
Aluminum	32.50	40.47	40.00	1.17
Chromium	33.00	39.85	40.00	0.37
Copper	32.50	40.47	40.00	1.17
Iron	32.50	40.47	40.00	1.17
Lead	32.50	40.47	40.00	1.17
Silver	32.50	40.47	40.00	1.17

Table 3.2.c   Comparison between the estimated and actual radii of the spheres as have been calculated from the average spacing of the spectral dips of the simulated backscattered spectra obtained for different materials due to incidence on center.

Material	Amplitude of the spectrum	Estimated Density (Kg/m^3)	Actual Density (Kg/m^3)	% Error
Aluminum	1.7587	2.45×10^3	2.70×10^3	9.2
Chromium	2.1334	7.36×10^3	7.19×10^3	2.3
Copper	2.1817	8.97×10^3	8.93×10^3	0.5
Iron	2.1546	8.01×10^3	7.87×10^3	1.7
Lead	2.2216	1.07×10^4	1.13×10^4	4.9
Silver	2.2120	1.03×10^4	1.05×10^4	1.9

Table 3.3   Comparison between the estimated and actual densities of the spheres for $R = 35$ mm, as have been calculated from the amplitudes of the simulated backscattered spectra obtained for different materials due to incidence on center.

Material	Average Spacing of Spectral Dips	Estimated Speed (m/s)	Actual Speed (m/s)	% Error
Aluminum	128.67	5138.85	5171.14	0.62
Chromium	129.33	5162.10	5141.93	0.39
Copper	94.62	3939.44	3916.83	0.58
Iron	114.50	4639.71	4624.39	0.33
Lead	40.62	2037.29	1947.28	4.62
Silver	72.25	3151.46	3096.85	1.76

Table 3.4   Comparison between the estimated and actual speeds of propagation inside the spheres for $R = 35\,\text{mm}$, as have been calculated from the average spacing of the spectral dips of the simulated backscattered spectra obtained for different materials due to incidence on center.

106

Material	Average Spacing of Spectral Dips	Estimated Radius (mm)	Actual Radius (mm)	% Error
Aluminum	41.00	32.06	35.00	8.41
Chromium	38.00	34.59	35.00	1.16
Copper	37.50	35.06	35.00	0.17
Iron	37.75	34.82	35.00	0.50
Lead	38.00	34.59	35.00	1.16
Silver	37.00	35.53	35.00	1.51

Table 3.5.a   Comparison between the estimated and actual radii of the spheres as have been calculated from the average spacing of the spectral dips of the backscattered spectra obtained for different materials due to incidence off center by a distance $x = 15$ mm.

Material	Average Spacing of Spectral Dips	Estimated Radius (mm)	Actual Radius (mm)	% Error
Aluminum	43.00	30.56	35.00	12.68
Chromium	39.00	33.70	35.00	3.70
Copper	38.50	34.14	35.00	2.45
Iron	39.00	33.70	35.00	3.70
Lead	39.50	33.28	35.00	4.92
Silver	38.50	34.14	35.00	2.45

Table 3.5.b   Comparison between the estimated and actual radii of the spheres as have been calculated from the average spacing of the spectral dips of the simulated backscattered spectra obtained for different materials due to incidence off center by a distance $x = 45$ mm.

Material	Amplitude of the spectrum	Estimated Density (Kg/m^3)	Actual Density (Kg/m^3)	% Error
Aluminum	1.7601	2.46×10^3	2.70×10^3	8.9
Chromium	2.1338	7.37×10^3	7.19×10^3	2.5
Copper	2.1819	8.98×10^3	8.93×10^3	0.6
Iron	2.1549	8.02×10^3	7.87×10^3	1.91
Lead	2.2217	1.07×10^4	1.13×10^4	6.0
Silver	2.2121	1.03×10^4	1.05×10^4	1.9

Table 3.6.a Comparison between the estimated and actual densities of the spheres for $R = 35$ mm as have been calculated from the amplitudes of the simulated backscattered spectra obtained for different materials due to incidence off center by a distance $x = 15$ mm.

Material	Amplitude of the spectrum	Estimated Density (Kg/m^3)	Actual Density (Kg/m^3)	% Error
Aluminum	1.7719	2.52×10^3	2.70×10^3	6.7
Chromium	2.1373	7.47×10^3	7.19×10^3	3.9
Copper	2.1841	9.07×10^3	8.93×10^3	1.6
Iron	2.1579	8.12×10^3	7.87×10^3	3.2
Lead	2.2225	1.08×10^4	1.13×10^4	4.4
Silver	2.2137	1.03×10^4	1.05×10^4	1.9

Table 3.6.b Comparison between the estimated and actual densities of the spheres for $R = 35$ mm as have been calculated from the amplitudes of the simulated backscattered spectra obtained for different materials due to incidence off center by a distance $x = 45$ mm.

Material	Average Spacing of Spectral Dips	Estimated Speed (m/s)	Actual Speed (m/s)	% Error
Aluminum	128.83	5144.60	5171.14	0.51
Chromium	129.33	5162.22	5141.93	0.39
Copper	94.62	3939.62	3916.83	0.58
Iron	114.67	4645.58	4624.39	0.46
Lead	40.62	2037.47	1947.28	4.63
Silver	72.12	3147.05	3096.85	1.62

Table 3.7.a   Comparison between the estimated and actual speeds of propagation inside the spheres for $R = 35$ mm as have been calculated from the average spacing of the spectral dips of the backscattered spectra obtained for different materials due to incidence off center by a distance $x = 15$ mm.

111

Material	Average Spacing of Spectral Dips	Estimated Speed (m/s)	Actual Speed (m/s)	% Error
Aluminum	129.33	5162.22	5171.14	0.17
Chromium	129.50	5168.09	5141.93	0.51
Copper	94.62	3939.62	3916.83	0.58
Iron	114.67	4645.58	4624.39	0.46
Lead	40.62	2037.47	1947.28	4.63
Silver	72.12	3147.05	3096.85	1.62

Table 3.7.b   Comparison between the estimated and actual speeds of propagation inside the spheres for $R = 35$ mm as have been calculated from the average spacing of the spectral dips of the backscattered spectra obtained for different materials due to incidence off center by a distance $x = 45$ mm.

CHAPTER 4

SCATTERING OF ELECTROMAGNETIC X-WAVESBY A PERFECTLY CONDUCTING SPHER

4.1 INTRODUCTION

In the previous two chapters, we studied the scattering of acoustic X-waves by rigid and soft sphere. In this chapter, we shall deal with the scattering of transverse electric (TE) electromagnetic X-wave (EMXW) by a rigid conducting sphere. We start by assuming a plane wave incident on a rigid conducting sphere such that the wave is propagating in the z-direction. The electric and magnetic field components are directed along the x-axis and y-axis, respectively, as shown in Fig. (4.1). X-waves are composed as superpositions over plane waves propagating along a direction tilted at a fixed angle relative to the axis of propagation such that the associated wave vectors form a conic surface. In order to study the scattering of X-waves, we need to derive first expressions for the scattering of an electromagnetic plane wave incident at a tilted angle relative to the z-axis and then integrate over the azimuthal angular direction to include all vectors lying on the spectral cone.

4.2 SCATTERING OF A PLANE WAVE BY A CONDUCTING SPHERE

Starting with a plane wave traveling in the z-direction, we use appropriate counter clockwise (CCW) rotation matrices [87] to rotate the coordinate system around the x-

direction by an angle ϕ' then about the new z-axis, namely z', by an angle θ_k. The indicated rotations are shown in Fig. (2). The $\vec{k}$, $\vec{E}$, and $\vec{H}$ vectors before rotation would have the following forms:

$$\vec{k} = \vec{u}_z k \qquad (4.2.1)$$

$$\vec{E} = \vec{u}_x E_0 e^{-i\vec{k}\cdot\vec{r}} \qquad (4.2.2)$$

$$\vec{H} = \vec{u}_y H_0 e^{-i\vec{k}\cdot\vec{r}} \qquad (4.2.3)$$

The rotation CCW rotation matrix would be as follows:

$$Z'X = \begin{bmatrix} \cos\phi' & \sin\phi' & 0 \\ -\sin\phi' & \cos\phi' & 0 \\ 0 & 0 & 1 \end{bmatrix} \begin{bmatrix} 1 & 0 & 0 \\ 0 & \cos\theta_k & \sin\theta_k \\ 0 & -\sin\theta_k & \cos\theta_k \end{bmatrix}.$$

The rotation angle ϕ' is related to the azimuthal angle ϕ_k of the $\vec{k}$ vector in the new coordinate system as follows:

$$\phi' = (\pi/2) - \phi_k. \qquad (4.2.4)$$

Therefore,

$$\cos\phi' = \cos((\pi/2) - \phi_k) = \cos(\pi/2)\cos\phi_k + \sin(\pi/2)\sin\phi_k = \sin\phi_k, \qquad (4.2.5)$$

and

$$\sin\phi' = \sin((\pi/2) - \phi_k) = \sin(\pi/2)\cos\phi_k - \cos(\pi/2)\sin\phi_k = \cos\phi_k. \qquad (4.2.6)$$

Using Eqs. (4.2.5) and (4.2.6) in the previously mentioned rotation matrix yields

$$Z'X = \begin{bmatrix} \sin\phi_k & \cos\phi_k & 0 \\ -\cos\phi_k & \sin\phi_k & 0 \\ 0 & 0 & 1 \end{bmatrix} \begin{bmatrix} 1 & 0 & 0 \\ 0 & \cos\theta_k & \sin\theta_k \\ 0 & -\sin\theta_k & \cos\theta_k \end{bmatrix}.$$

114

Therefore, the wave vector after rotation would look like

$$\vec{k}'' = Z'X \begin{bmatrix} 0 \\ 0 \\ k \end{bmatrix} = k\left(\vec{u}_x \sin\theta_k \cos\phi_k + \vec{u}_y \sin\theta_k \sin\phi_k + \vec{u}_z \cos\theta_k\right). \qquad (4.2.7)$$

Similarly, the incident electric field after rotation would be

$$\vec{E}'' = Z'X \begin{bmatrix} E_0 e^{-i\vec{k}\cdot\vec{r}} \\ 0 \\ 0 \end{bmatrix} = E_0 e^{-i\vec{k}\cdot\vec{r}}\left(\vec{u}_x \sin\phi_k - \vec{u}_y \cos\phi_k\right), \qquad (4.2.8)$$

and the rotated incident magnetic field would be

$$\vec{H}'' = Z'X \begin{bmatrix} 0 \\ H_0 e^{-i\vec{k}\cdot\vec{r}} \\ 0 \end{bmatrix} = H_0 e^{-i\vec{k}\cdot\vec{r}}\left(\vec{u}_x \cos\phi_k \cos\theta_k + \vec{u}_y \sin\phi_k \cos\theta_k - \vec{u}_z \sin\theta_k\right). \qquad (4.2.9)$$

In order to be sure that the rotated results are correct we should verify that $\vec{E}'' \cdot \vec{k}'' = 0$
and $\vec{H}'' \cdot \vec{k}'' = 0$. Moreover, $\vec{k}'' \cdot \vec{r}'' = kr\cos\gamma$, [cf. section 2.2] where $\cos\gamma$ is given by
Eq. (2.2.5). Along these lines, using Eqs. (4.2.7) and (4.2.8)

$$\vec{E}'' \cdot \vec{k}'' = E_0 e^{-i\vec{k}\cdot\vec{r}}\left(\sin\theta_k \sin\phi_k \cos\phi_k - \sin\theta_k \sin\phi_k \cos\phi_k\right) = 0.$$

Similarly, using Eqs. (4.2.7) and (4.2.9)

$$\vec{H}'' \cdot \vec{k}'' = H_0 e^{-i\vec{k}\cdot\vec{r}}\left(\sin\theta_k \cos\theta_k \cos^2\phi_k + \sin\theta_k \cos\theta_k \sin^2\phi_k - \sin\xi\cos\xi\right) = 0.$$

Since $\vec{r}''(r,\theta,\phi) = r\sin\theta\cos\phi + r\sin\theta\sin\phi + r\cos\theta$, hence,

$$\vec{k}'' \cdot \vec{r}'' = kr\left(\sin\theta_k \cos\phi_k \sin\theta\cos\phi + \sin\theta_k \sin\phi_k \sin\theta\sin\phi + \cos\theta_k \cos\theta\right)$$
$$= kr\left(\sin\theta_k \sin\theta\cos(\phi_k - \phi) + \cos\theta_k \cos\theta\right).$$

By verifying the above three relations we established that the incident plane wave components are rotated to form a family of plane waves having their wave vectors lying on a conic surface with a half apex angle θ_k.

We calculate the incident electric field components of Eq. (4.2.8) in spherical coordinates, viz.,

$$
\begin{aligned}
E_r^i &= E_x^i \sin\theta\cos\phi + E_y^i \sin\theta\sin\phi + E_z^i \cos\theta \\
&= E_0 e^{-ikr\cos\gamma}\left(\sin\theta\cos\phi\sin\phi_k - \sin\theta\sin\phi\cos\phi_k\right) \\
&= E_0 e^{-ikr\cos\gamma}\sin\theta\sin(\phi_k - \phi),
\end{aligned}
\tag{4.2.10}
$$

$$
\begin{aligned}
E_\theta^i &= E_x^i \cos\theta\cos\phi + E_y^i \cos\theta\sin\phi - E_z^i \sin\theta \\
&= E_0 e^{-ikr\cos\gamma}\left(\cos\theta\cos\phi\cos\phi_k - \cos\theta\sin\phi\cos\phi_k\right) \\
&= E_0 e^{-ikr\cos\gamma}\cos\theta\sin(\phi_k - \phi),
\end{aligned}
\tag{4.2.11}
$$

and

$$
\begin{aligned}
E_\phi^i &= -E_x^i \sin\phi + E_y^i \cos\phi = E_0 e^{-ikr\cos\gamma}\left(-\sin\phi\sin\phi_k - \cos\phi\cos\phi_k\right) \\
&= -E_0 e^{-ikr\cos\gamma}\cos(\phi_k - \phi).
\end{aligned}
\tag{4.2.12}
$$

From Chapter 2, [cf. Eqs. (2.3.2) and (2.3.3)], we have

$$
e^{-ikr\cos\gamma} = \sum_{n=0}^{\infty}(-i)^n(2n+1)j_n(kr)P_n(\cos\gamma)
\tag{4.2.13}
$$

and

$$
P_n(\cos\gamma) = \sum_{m=0}^{\infty}\varepsilon_m\frac{(n-m)!}{(n+m)!}P_n^m(\cos\theta)P_n^m(\cos\theta_k)\cos(m(\phi_k - \phi)),
\tag{4.2.14}
$$

where $\varepsilon_m = 1$ for $m = 0$, or $\varepsilon_m = 2$ otherwise.

Considering that

$$
\frac{\partial}{\partial\phi_k}e^{-ikr\cos\gamma} = \frac{\partial}{\partial\phi_k}e^{-ikr(\cos\theta\cos\theta_k + \sin\theta\sin\theta_k\cos(\phi_k - \phi))} = ikr\sin\theta_k\sin\theta\sin(\phi_k - \phi)e^{-ikr\cos\gamma}
$$

116

Therefore,

$$\sin\theta\sin(\phi_k - \phi)e^{-ikr\cos\gamma} = \frac{1}{ikr\sin\theta_k}\frac{\partial}{\partial\phi_k}e^{-ikr\cos\gamma} \qquad (4.2.15)$$

Using Eqs. (4.2.13) and (4.2.15) in Eqs. (4.2.10-12), the spherical components of the incident electric field becomes

$$E_r^i = \frac{E_0}{ikr\sin\theta_k}\sum_{n=0}^{\infty}(-i)^n(2n+1)j_n(kr)\frac{\partial P_n(\cos\gamma)}{\partial\phi_k}, \qquad (4.2.16)$$

$$E_\theta^i = E_0\cos\theta\sin(\phi_k - \phi)\sum_{n=0}^{\infty}(-i)^n(2n+1)j_n(kr)P_n(\cos\gamma), \qquad (4.2.17)$$

$$E_\phi^i = -E_0\cos(\phi_k - \phi)\sum_{n=0}^{\infty}(-i)^n(2n+1)j_n(kr)P_n(\cos\gamma). \qquad (4.2.18)$$

Analogously, we can derive the magnetic field components of Eq. (4.2.9) in spherical coordinates

$$\begin{aligned}
H_r^i &= H_x^i\sin\theta\cos\phi + H_y^i\sin\theta\sin\phi + H_z^i\cos\theta \\
&= H_0 e^{ikr\cos\gamma}\left(\cos\theta_k\cos\phi_k\sin\theta\cos\phi + \cos\theta_k\sin\phi_k\sin\theta\sin\phi - \cos\theta\sin\theta_k\right) \\
&= H_0 e^{-ikr\cos\gamma}\left(\cos\theta_k\sin\theta\cos(\phi_k - \phi) - \sin\theta_k\cos\theta\right).
\end{aligned}$$

But

$$\begin{aligned}
\frac{\partial}{\partial\theta_k}e^{-ikr\cos\gamma} &= \frac{\partial}{\partial\theta_k}e^{ikr(\sin\theta\sin\theta_k\cos(\phi_k-\phi)+\cos\theta\cos\theta_k)} \\
&= -ikr\left(\sin\theta\cos\theta_k\cos(\phi_k - \phi) - \cos\theta\sin\theta_k\right)e^{-ikr\cos\gamma}.
\end{aligned}$$

Hence,

$$\left(\sin\theta\cos\theta_k\cos(\phi_k - \phi) - \cos\theta\sin\theta_k\right)e^{-ikr\cos\gamma} = -\frac{1}{ikr}\frac{\partial}{\partial\theta_k}e^{-ikr\cos\gamma}. \qquad (4.2.19)$$

117

Using Eq. (4.2.19) in the expression for the radial component of the incident magnetic field gives

$$H_r^i = -\frac{H_0}{ikr} \sum_{n=0}^{\infty} (-i)^n (2n+1) j_n(kr) \frac{\partial P_n(\cos\gamma)}{\partial\theta_k} \tag{4.2.20}$$

As for the magnetic field component in the θ direction

$$
\begin{aligned}
H_\theta^i &= H_x^i \cos\theta\cos\phi + H_y^i \cos\theta\sin\phi - H_z^i \sin\theta \\
&= H_0 e^{-ikr\cos\gamma} (\cos\theta_k \cos\phi_k \cos\theta\cos\phi + \cos\theta_k \sin\phi_k \cos\theta\sin\phi + \sin\theta\sin\theta_k) \\
&= H_0 (\cos\theta\cos\theta_k \cos(\phi_k - \phi) + \sin\theta\sin\theta_k) \sum_{n=0}^{\infty} (-i)^n (2n+1) j_n(kr) P_n(\cos\gamma),
\end{aligned}
$$

$$\tag{4.2.21}$$

and the magnetic field component in the azimuthal direction would be

$$
\begin{aligned}
H_\phi^i &= -H_x^i \sin\phi + H_y^i \cos\phi \\
&= H_0 e^{-ikr\cos\gamma} (-\cos\theta_k \cos\phi_k \sin\phi + \cos\theta_k \sin\phi_k \cos\phi) \\
&= H_0 \cos\theta_k \sin(\phi_k - \phi) \sum_{n=0}^{\infty} (-i)^n (2n+1) j_n(kr) P_n(\cos\gamma).
\end{aligned}
$$

$$\tag{4.2.22}$$

Following the procedure described in Chapter 10 of Ref. 80, The TE and TM potentials F_r^i and A_r^i for the incident field can be calculated as follows:

$$E_r^i = \frac{1}{i\omega\mu\varepsilon} \left(\frac{\partial^2}{\partial r^2} + k^2 \right) A_r^i \tag{4.2.23}$$

Substituting Eq. (4.2.16) in (4.2.23) and letting $\hat{J}_n(kr) = (kr) j_n(kr)$, we obtain

$$\frac{E_0}{i(kr)^2 \sin\theta_k} \sum_{n=0}^{\infty} (-i)^n (2n+1) \hat{J}_n(kr) \frac{\partial P_n(\cos\gamma)}{\partial\phi_k} = \frac{1}{i\omega\mu\varepsilon} \left(\frac{\partial^2}{\partial r^2} + k^2 \right) A_r^i$$

Using the fact that

$$\left(\frac{\partial^2}{\partial r^2} + k^2\right)\hat{J}_n(kr) = \frac{n(n+1)}{r^2}\hat{J}_n(kr),$$

we obtain

$$A_r^i = \frac{E_0}{\omega\sin\theta_k}\sum_{n=0}^{\infty}(-i)^n\frac{(2n+1)}{n(n+1)}\hat{J}_n(kr)\frac{\partial P_n(\cos\gamma)}{\partial\phi_k} \qquad (4.2.24)$$

Similarly, we can derive F_r^i from H_r^i

$$H_r^i = \frac{1}{i\omega\mu\epsilon}\left(\frac{\partial^2}{\partial r^2} + k^2\right)F_r^i \qquad (4.2.25)$$

Substituting for H_r^i given in Eq. (4.2.20)

$$-\frac{E_0}{i(kr)^2}\sum_{n=0}^{\infty}(-i)^n(2n+1)\hat{J}_n(kr)\frac{\partial P_n(\cos\gamma)}{\partial\theta_k} = \frac{1}{i\omega\mu\epsilon}\left(\frac{\partial^2}{\partial r^2} + k^2\right)F_r^i .$$

Solving for F_r^i, we obtain

$$F_r^i = -\frac{E_0}{\omega\eta}\sum_{n=0}^{\infty}(-i)^n\frac{(2n+1)}{n(n+1)}\hat{J}_n(kr)\frac{\partial P_n(\cos\gamma)}{\partial\theta_k}, \qquad (4.2.26)$$

where $\eta = \sqrt{\mu/\epsilon}$.

We shall deduce the scattered TE and TM potentials from the incident ones by assuming that they should have the same form but with different series coefficients.

$$A_r^s = \frac{E_0}{\omega\sin\theta_k}\sum_{n=0}^{\infty}b_n\hat{H}_n^{(2)}(kr)\frac{\partial P_n(\cos\gamma)}{\partial\phi_k} \qquad (4.2.27)$$

$$F_r^s = -\frac{E_0}{\omega\eta}\sum_{n=0}^{\infty}c_n\hat{H}_n^{(2)}(kr)\frac{\partial P_n(\cos\gamma)}{\partial\theta_k} \qquad 4.2.28)$$

119

Both field potentials have the same form as the incident ones except that the spherical Bessel function $\hat{J}_n(kr)$ has been replaced by spherical Hankel function $\hat{H}_n^{(2)}(kr)$ to represent the spherical waves traveling away from the scatterer.

The series coefficients have to be calculated from the boundary conditions. For the case of scattering by a perfectly conducting sphere, there are two boundary conditions that should be satisfied:

$$E'_\theta(r = R, 0 \le \theta \le \pi, 0 \le \phi \le 2\pi) = 0, \text{ and} \tag{4.2.29a}$$

$$E'_\phi(r = R, 0 \le \theta \le \pi, 0 \le \phi \le 2\pi) = 0 \tag{4.2.29b}$$

where E' stands for the total field.

The total field components could be calculated using the following expressions:

$$E'_r = \frac{1}{i\omega\mu\varepsilon}\left(\frac{\partial^2}{\partial r^2} + k^2\right)A'_r, \tag{4.2.30a}$$

$$E'_\theta = \frac{1}{i\omega\mu\varepsilon}\frac{1}{r}\frac{\partial^2 A'_r}{\partial r \partial\theta} - \frac{1}{\varepsilon}\frac{1}{r\sin\theta}\frac{\partial F'_r}{\partial\phi}, \tag{4.2.30b}$$

$$E'_\phi = \frac{1}{i\omega\mu\varepsilon}\frac{1}{r\sin\theta}\frac{\partial^2 A'_r}{\partial r \partial\phi} + \frac{1}{\varepsilon}\frac{1}{r}\frac{\partial F'_r}{\partial\theta}, \tag{4.2.30c}$$

$$H'_r = \frac{1}{i\omega\mu\varepsilon}\left(\frac{\partial^2}{\partial r^2} + k^2\right)F'_r, \tag{4.2.30d}$$

$$H'_\theta = \frac{1}{\mu}\frac{1}{r\sin\theta}\frac{\partial A'_r}{\partial\phi} + \frac{1}{i\omega\mu\varepsilon}\frac{1}{r}\frac{\partial^2 F'_r}{\partial r \partial\theta}, \tag{4.2.30e}$$

120

$$H'_\phi = -\frac{1}{\mu}\frac{1}{r}\frac{\partial A'_r}{\partial \theta} + \frac{1}{i\omega\mu\varepsilon}\frac{1}{r\sin\theta}\frac{\partial^2 F'_r}{\partial r\partial\phi}.$$

(4.2.30f)

where

$$A'_r = A'_r + A'^s_r = \frac{E_0}{\omega\sin\theta_k}\sum_{n=0}^{\infty}\left(a_n\hat{J}_n(kr) + b_n\hat{H}_n^{(2)}(kr)\right)\frac{\partial P_n(\cos\gamma)}{\partial\phi_k}$$

(4.2.31a)

$$F'_r = F'_r + F'^s_r = -\frac{H_0}{\omega\eta}\sum_{n=0}^{\infty}\left(a_n\hat{J}_n(kr) + c_n\hat{H}_n^{(2)}(kr)\right)\frac{\partial P_n(\cos\gamma)}{\partial\theta_k}$$

(4.2.31b)

Using Eq. (4.2.30b) with the boundary condition given by Eq. (4.2.29a), we get

$$\frac{1}{i\omega\mu\varepsilon}\frac{1}{r}\frac{\partial^2 A'_r}{\partial r\partial\theta} = \frac{1}{\varepsilon}\frac{1}{r\sin\theta}\frac{\partial F'_r}{\partial\phi}.$$

Therefore,

$$\frac{1}{i\omega\mu\varepsilon}\frac{1}{R}\frac{E_0 k}{\omega\sin\theta_k}\sum_{n=0}^{\infty}\left(a_n\hat{J}_n{}'(kR) + b_n\hat{H}_n^{(2)}{}'(kR)\right)\frac{\partial P_n(\cos\gamma)}{\partial\theta\partial\phi_k}$$
$$-\frac{E_0}{\omega\eta\varepsilon}\frac{1}{R\sin\theta}\sum_{n=0}^{\infty}\left(a_n\hat{J}_n(kR) + c_n\hat{H}_n^{(2)}(kR)\right)\frac{\partial P_n(\cos\gamma)}{\partial\theta_k\partial\phi} = 0.$$

Here, $a_n = (-i)^n(2n+1)/n(n+1)$. The boundary condition of Eq. (4.2.29a) is satisfied provided that

$$a_n\hat{J}_n{}'(kR) + b_n\hat{H}_n^{(2)}{}'(kR) = 0$$

and

$$a_n\hat{J}_n(kR) + c_n\hat{H}_n^{(2)}(kR) = 0.$$

These conditions imply that

121

$$b_n = -(-i)^n \frac{(2n+1)}{n(n+1)} \frac{\hat{J}_n{}'(kR)}{\hat{H}_n^{(2)'}(kR)} \tag{4.2.32a}$$

and

$$c_n = -(-i)^n \frac{(2n+1)}{n(n+1)} \frac{\hat{J}_n(kR)}{\hat{H}_n^{(2)}(kR)}. \tag{4.2.32b}$$

4.3 SCATTERING OF X-WAVES WAVE BY A CONDUCTING SPHERE

Similarly to the acoustic case, we construct the X-wave solution as a superposition of the following form:

$$\vec{E}(\vec{r},t) = \int_0^\infty dk \int_0^{2\pi} d\phi_k \int_0^{2\pi} d\theta_k k^{\mu+2} \sin\theta_k e^{-ka} \delta(\theta_k - \xi) e^{i\omega t} \vec{\bar{E}}(k), \tag{4.3.1}$$

where $\omega = |k|c$. For the incident field it can be directly shown that the above superposition yields

$$E_r^i = E_\theta^i = 0.$$

Therefore, the incident X-wave is polarized in the transverse ϕ-direction, specifically,

$$E_\phi^i = -E_0 \int_0^\infty dk \int_0^{2\pi} d\phi_k \int_0^{\pi} d\theta_k k^{\mu+2} \sin\theta_k e^{-ka} e^{ikct} \delta(\theta_k - \xi) \cos(\phi_k - \phi) \sum_{n=0}^{\infty} (-i)^n (2n+1) j_n(kr)$$

$$\times \sum_{m=0}^{\infty} \varepsilon_m \frac{(n-m)!}{(n+m)!} P_n^m(\cos\xi) P_n^m(\cos\theta) \cos(m(\phi_k - \phi)). \tag{4.3.2}$$

The integration over ϕ_k gives zero values for $m \neq 1$, and the integration over θ_k picks the value $\theta_k = \xi$. Therefore, the incident electric field becomes

$$E_\phi^i = -E_0 \, 2\pi \sin\xi \int_0^\infty dk\, k^{\mu+2} \sin\theta_k\, e^{-ka} e^{ikct} \delta(\theta_k - \xi)\cos(\phi_k - \phi)$$

$$\times \sum_{n=0}^\infty (-i)^n (2n+1) j_n(kr) P_n^1(\cos\theta) P_n^1(\cos\xi). \qquad (4.3.3)$$

The scattered field components would acquire the following form:

$$E_r^s = \int_0^\infty dk \int_0^{2\pi} d\phi_k \int_0^\pi d\theta_k\, k^{\mu+2} \sin\theta_k\, e^{-ka} \delta(\theta_k - \xi) \frac{E_0}{ik^2 \sin\theta_k} \sum_{n=0}^\infty b_n k^2 \frac{\partial P_n(\cos\gamma)}{\partial\phi_k}$$

$$\times \left(\frac{\partial^2 \hat{H}_n^{(2)}(kr)}{\partial r^2} + \hat{H}_n^{(2)}(kr) \right).$$

$$(4.3.4)$$

Carrying out the integration over θ_k, we obtain

$$E_r^s = \frac{E_0}{i} \int_0^\infty dk \int_0^{2\pi} d\phi_k\, k^{\mu+2} e^{-ka} \sum_{n=0}^\infty b_n \left(k^2 \frac{\partial^2 \hat{H}_n^{(2)}(kr)}{\partial r^2} + \hat{H}_n^{(2)}(kr) \right) \sum_{m=0}^\infty \varepsilon_m \frac{(n-m)!}{(n+m)!} (-m)$$

$$\times \sin(m(\phi_k - \phi)) P_n^m(\cos\xi) P_n^m(\cos\theta)). \qquad (4.3.5)$$

The integration over ϕ_k yields $E_r^s = 0$. As for the component in the θ-direction

$$E_\theta^s = \int_0^\infty dk \int_0^{2\pi} d\phi_k \int_0^\pi d\theta_k\, k^{\mu+2} \sin\theta_k\, e^{-ka} \delta(\theta_k - \xi) \frac{E_0}{kr}$$

$$\times \left(\frac{1}{i\sin\theta_k} \sum_{n=0}^\infty b_n \frac{\partial \hat{H}_n^{(2)}(kr)}{\partial r} \sum_{m=0}^\infty \varepsilon_m \frac{(n-m)!}{(n+m)!} (-m)\sin(m(\phi_k - \phi)) P_n^m(\cos\theta_k) \frac{\partial P_n^m(\cos\theta)}{\partial\theta} \right.$$

$$\left. + \frac{1}{\sin\theta} \sum_{n=0}^\infty c_n \hat{H}_n^{(2)}(kr) \sum_{m=0}^\infty \varepsilon_m \frac{(n-m)!}{(n+m)!} (m)\sin(m(\phi_k - \phi)) P_n^m(\cos\theta) \frac{\partial P_n^m(\cos\theta_k)}{\partial\theta_k} \right).$$

$$(4.3.6)$$

123

The inegration over ϕ_k gives $E^s_\theta = 0$. As for the E^s_ϕ component

$$
E^s_\phi = \int_0^\infty dk \int_0^{2\pi} d\phi_k \int_0^\pi d\theta_k\, k^{\mu+2} \sin\theta_k\, e^{-ka}\delta(\theta_k - \xi)\frac{E_0}{kr}
$$

$$
\times \left(\frac{1}{i\sin\theta_k \sin\theta}\sum_{n=0}^\infty b_n \frac{\partial \hat{H}_n^{(2)}(kr)}{\partial r}\sum_{m=0}^\infty \varepsilon_m \frac{(n-m)!}{(n+m)!}(m^2)\cos(m(\phi_k - \phi))P_n^m(\cos\theta_k)P_n^m(\cos\theta) \right.
$$

$$
\left. -\sum_{n=0}^\infty c_n \hat{H}_n^{(2)}(kr)\sum_{m=0}^\infty \varepsilon_m \frac{(n-m)!}{(n+m)!}\cos(m(\phi_k - \phi))\frac{\partial P_n^m(\cos\theta_k)}{\partial\theta_k}\frac{\partial P_n^m(\cos\theta)}{\partial\theta} \right).
$$

$$(4.3.7)$$

Integrating over θ_k then ϕ_k reduces the above expression to the following form

$$
E^s_\phi = -2\pi \sin\xi \int_0^\infty dk\, k^{\mu+2} e^{-ka}\frac{E_0}{kr}\sum_{n=0}^\infty c_n \hat{H}_n^{(2)}(kr)P_n^1(\cos\xi)P_n^1(\cos\theta)
$$

$$(4.3.8)$$

Similarly, one can calculate the scattered magnetic field components; *viz.*,

$$
H^s_r = -\frac{E_0}{\mu\varepsilon\eta}\int_0^\infty dk \int_0^{2\pi} d\phi_k \int_0^\pi d\theta_k\, k^{\mu+2}\sin\theta_\zeta e^{-ka}\frac{k^2}{i\omega^2}\sum_{n=0}^\infty c_n\left(\frac{\partial^2 \hat{H}_n^{(2)}(kr)}{\partial r^2} + \hat{H}_n^{(2)}(kr) \right)
$$

$$
\times \sum_{m=0}^\infty \varepsilon_m \frac{(n-m)!}{(n+m)!}\frac{\partial P_n^m(\cos\theta_k)}{\partial\theta_k}P_n^m(\cos\theta)\cos(m(\phi_k - \phi))
$$

$$(4.3.9)$$

Performing the integrations over θ_k then ϕ_k gives

$$
H^s_r = i2\pi\frac{E_0}{\eta}\sin\xi \int_0^\infty dk\, k^{\mu+2} e^{-ka}\sum_{n=0}^\infty c_n\left(\frac{\partial^2 \hat{H}_n^{(2)}(kr)}{\partial r^2} + \hat{H}_n^{(2)}(kr) \right)P_n^1(\cos\xi)P_n^1(\cos\theta).
$$

$$(4.3.10)$$

124

$$H_\theta^s = \int_0^\infty dk \int_0^{2\pi} d\phi_k \int_0^\pi d\theta_k \, k^{\mu+2} \sin\theta_k \, e^{-ka} \delta(\theta_k - \xi)$$

$$\times \left(\frac{E_0}{\omega\mu r \sin\theta_k \sin\theta} \sum_{n=0}^\infty b_n \hat{H}_n^{(2)}(kr) \sum_{m=0}^\infty \varepsilon_m \frac{(n-m)!}{(n+m)!} (m^2) \cos(m(\phi_k - \phi)) P_n'''(\cos\theta_k) P_n'''(\cos\theta) \right.$$

$$\left. - \frac{E_0 k}{i\omega^2 \mu\varepsilon\eta r} \sum_{n=0}^\infty c_n \frac{\partial \hat{H}_n^{(2)}(kr)}{\partial r} \sum_{m=0}^\infty \varepsilon_m \frac{(n-m)!}{(n+m)!} \cos(m(\phi_k - \phi)) \frac{\partial P_n'''(\cos\theta_k)}{\partial\theta_k} \frac{\partial P_n'''(\cos\theta)}{\partial\theta} \right).$$

The integration over θ_k and ϕ_k yields

$$H_\theta^s = \frac{i 2\pi E_0}{\eta r} \sin\xi \int_0^\infty dk \, k^{\mu+2} e^{-ka} \frac{1}{k} \sum_{n=0}^\infty c_n \frac{\partial \hat{H}_n^{(2)}(kr)}{\partial r} P_n^1(\cos\xi) P_n^1(\cos\theta). \qquad (4.3.11)$$

Following similar steps, the ϕ component of the X-wave gives

$$H_\phi^s = 0. \qquad (4.2.44)$$

4.4 CONCLUDING REMARKS

In this chapter, a Mie series approach to the evaluation of the scattered X-wave from a conducting sphere has been used. This has been done by determining first the scattered field of a plane wave incident in a direction tilted at an angle θ_k with the z-axis. Subsequently, the azimuthal superposition over all plane waves making the same angle with the z-axis composes the incident X-wave. The scattered field can then be found by evaluating the azimuthal superposition of the scattered fields. The extension of this approach can be easily extended to the case of dielectric spheres. Further work should be undertaken to show that an approach analogous to the one used in Chapter 3 could be employed to determine the size and material of dielectric scatterers.
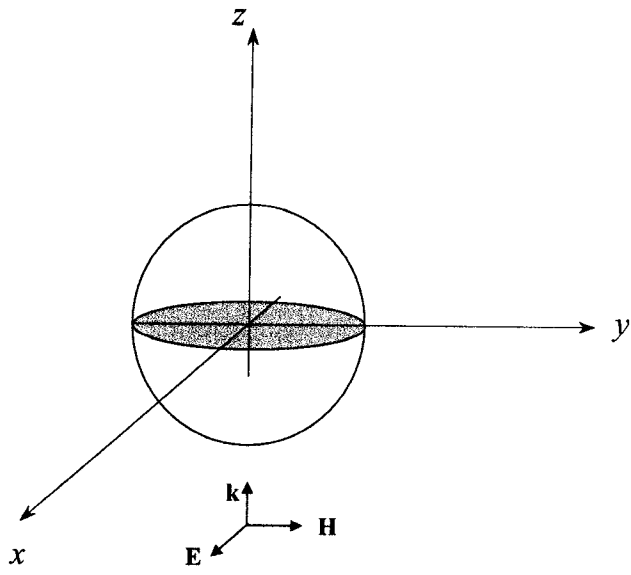
125

Figure 4.1 Electromagnetic plane wave incident on a perfectly conducting sphere.
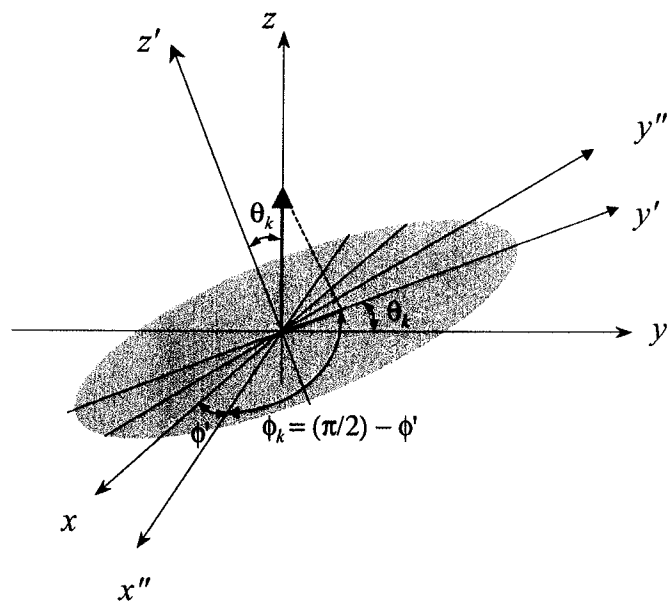
Figure 4.2 Rotations around the x and z' axes.

CHAPTER 5

CONCLUSION

In this work, we investigated thoroughly the scattering of X waves by spherical objects. We studied the scattering of acoustic X-waves from rigid and soft spheres. In both cases, we considered the possibilities that the X-wave is incident with its axis passing through the center of the sphere and off center. We extended our analysis to the case of an electromagnetic X-wave incident on a perfectly conducting sphere. From the analysis of the shapes of the spectra of the scattered fields, we suggested a new identification method by which one can specify the radii and materials of unknown spherical scatterers.

In Chapter 2, we derived the expression for the incident AXW from the scalar wave equation, and then we derived an expression for the scattered field due to on-center incidence. In addition, we also obtained the expression for the scattered pulse in case of off-center incidence. We investigated the effect of changing the parameters and variables appearing in the spectrum of the scattered pulse, which are θ, a, ξ, R and r determining the scattering angle, the pulse width, the apex angle of the spectral cone, the radius of the scattering sphere, and the observation distance, respectively. From our study to the effect of changing the scattered angle, we deduced that the backscattered spectrum is more useful for identification because it contains a number of peaks and dips that reflect specific information about the scattering spheres.

128

Regarding the effect of the pulse width, we verified that although the smaller the value of a the more details we can get from the backscattered spectrum, possible problems might arise because reducing the pulse width by more than five times the sphere radius causes the series solution to diverge. As for our study to the effect of changing the apex angle, we realized that, physically, the condition $\xi \leq 20°$ corresponds to operating within a paraxial regime, where all plane wave spectral components are coming in at small angle relative to the axis of propagation. Studying the effect of changing the radius of the sphere showed that as the radius of the sphere increases, the average spacing between the spectral dips decreases. Thus, following the method described by Power *et al.* [74], we suggested doing a calibration curve relating the radius of the scattering sphere to the average spacing of the dips. Such a calibration curve can be used in determining the radii of unknown spheres. Moreover, our investigation for the effect of changing the observation distance demonstrated that the pulse decays as $(1/r)$. Finally, we considered the case of off-center incidence. We obtained good results for shifts outside the sphere for up to about 40% of the observation distance. It appears that within this range of off-center shifts, we only have a slight shift in the positions of the peaks with minimal decrease in the amplitudes. However, for larger distances, the shift in peak positions increases causing high percentage error in the calculated radii of the spheres.

In Chapter 3, we considered the scattering of AXW by soft spheres. We used the same expressions for the incident pulse. The scattered fields were derived in a series form where the coefficients appearing in the series solution were derived using the appropriate boundary conditions. We verified that this coefficient is function of the

129

density of the surrounding medium and the material, and the speed of sound waves in the medium and the scattering sphere. As done in Chapter 2, we studied the effect of changing the scattering angle on the backscattered spectrum, and showed that the backscattered spectrum contains a number of peaks and dips that carry information describing the scattering material. Hence, it is more appropriate in the identification and characterization of the material of the scatterer. In addition, we established that the medium surrounding the sphere is the main reason for classifying the sphere as rigid or soft, depending on the ratio $\left(\rho_0 c / \rho_e c_e\right)$. For all the materials considered in our study, they are considered as soft spheres if immersed in water, but as rigid if placed in air. We also showed that the amplitude of the backscattered spectrum by soft spheres varies with the density of the material and contains pronounced peaks and dips in the high frequency range that are sensitive to any change in the speed of wave propagation inside the sphere. Moreover the average spacing of the spectral dips at low frequencies is susceptible to different sphere radii, and minimally affected by the speed of propagation inside the sphere. Consequently, we proposed that we could do an arbitrary calibration curve, which is independent of the material, between the average spacing between the spectral dips at low frequencies and the radius of the sphere. Besides, similar calibration curves are suggested between the amplitude and the density, and the average spacing of the dips of the entire spectrum with the speed, at different radii. Thus utilizing the previously mentioned curves we can extract the radius of the scatterer and estimate its density as well as the speed of wave propagation inside it; i.e. we identify its size and characterize its material. Yet, we have to bear in mind that since the amplitude of the backscattered spectrum is dependent not only on the density of the sphere, but also on the observation distance and the power of the source. As a result, we should calibrate our system in such a way

130

to include the information about the radiated power of the source and the approximate location of the scatterer. We extended our investigation to the off-center case. We demonstrated that for a pulse incident on center or off center but inside the sphere, the accuracy of the estimates of the radii is almost the same. On the other hand, the precision starts to decrease when the pulse is incident outside the sphere. As for the density and the speed, the accuracy of the results remains the same no matter the pulse is incident on center, off center but inside or outside the sphere.

In Chapter 4, we derived a Mie series solution for the scattering from an electromagnetic plane wave incident at a tilted angle with respect to the z-axis. This solution was then used in a superposition over all azimuthally symmetric plane waves tilted at the same angle relative to the z-axis. The result wavefield represented the field scattered due to an electromagnetic X-wave incident on a perfectly conducting sphere. In future work, this analysis should be extended to the case of dielectric spheres and a procedure similar to the one used for soft spheres could be developed to identify the size and material of the unknown scatterers.

REFERENCES

1. Brittingham, "Focus wave modes in homogeneous Maxwell equations: Transverse electric mode," J. Appl. Phys. **54**, 1179-1189 (1983).

2. T. T. Wu and R. W. P. King, "Comments on focus wave modes in homogeneous Maxwell equations: Transverse electric mode," J. Appl. Phys. **56**, 2587-2588 (1984).

3. T. T. Wu and H. Lehmann, "Spreading of electromagnetic pulses," J. Appl. Phys. **58**, 2064-2065 (1985).

4. T. T. Wu, "Electromagnetic missiles," J. Appl. Phys. **57**, 2370-2373 (1985).

5. T. T. Wu, R. W. P. King and H. M. Shen, "Spherical lens as a launcher of electromagnetic missiles," J. Appl. Phys. **62**, 4036-4040 (1987).

6. H. M. Shen, T. T. Wu and R. W. P. King, "Generalized analysis of spherical lens as a launcher of electromagnetic missiles," J. Appl. Phys. **63**, 5647-5656 (1988).

7. H. M. Shen, "Experimental study of electromagnetic missiles," Proc. SPIE **873**, 338-346 (1988).

8. T. T. Wu and H. M. Shen, "Radiation of an electromagnetic pulse from an open end of a circular waveguide," Proc. SPIE **873**, 329-337 (1988).

9. T. T. Wu, R. W. P. King and H. M. Shen, "Circular cylindrical lens as a line source of electromagnetic missile launcher," IEEE Trans. Antennas Propag. **37**, 39-44 (1989).

10. H. M. Shen and T. T. Wu, "The properties of the electromagnetic missile," J. Appl. Phys. **66**, 4025-4034 (1989).

132

11. C. Ruan and C. Wan, "Choice of excitation in electromagnetic missiles," Electronic Lett. **25**, 1321-1323 (1989).

12. A. D. Yaghijan and T. B. Hansen, "Time-domain far fields," J. Appl. Phys. **79**, 2822-2830 (1996).

13. B. Hafizi, "Effects of carrier and dispersion on propagation of a directed electromagnetic pulse," J. Appl. Phys. **73**, 513-521 (1993).

14. J. Zhan and L. Wan, "Electromagnetic missile launched from a uniform current sheet," IEEE Trans. Electromagn. Compat. **33**, 61-63 (1991).

15. Z. Du and C. Ruan, "Comments on electromagnetic missile launched from a uniform current sheet," IEEE Trans. Electromagn. Compat. **36**, 155-156 (1994).

16. J. Durnin, "Exact solutions for nondiffracting beams. I. The scalar theory," J. Opt. Soc. Am. A **4**, 651-654 (1987).

17. J. Durnin, J. J. Miceli, Jr. And J. H. Eberly, "Diffraction free beams," Phys. Rev. Lett. **58**, 1499-1501 (1987).

18. J. Durnin, J. J. Miceli, Jr. And J. H. Eberly, "Comparison of Bessel and Gaussian beams," Opt. Lett. **13**, 79-80 (1988).

19. H. E. Moses, "The time-dependent inverse source problem for the acoustic and electromagnetic equations in one- and three-dimensional cases," J. Math. Phys. **25**, 1905-1923 (1984).

20. H. E. Moses and R. T. Prosser, "Initial conditions, sources and currents for prescribed time-dependent acoustic and electromagnetic fields in three dimensions, part I: the inverse initial value problem. acoustic and electromagnetic bullets, expanding waves and imploding waves," IEEE Trans. Antennas Propagat. **34**, 188-196 (1986).

133

21. H. E. Moses and R. T. Prosser, "Acoustic and electromagnetic bullets. New exact solutions of the acoustic and Maxwell's equations," SIAM J. Appl. Math. **50**, 1325-1340 (1990).

22. H. E. Moses, R. J. Nagen and G. V. H. Sandri, "The general solution of the three-dimension acoustic equation and of Maxwell's equations in the infinite domain in terms of the asymptotic solution in the wave zone," J. Math. Phys. **33**, 86-101 (1992).

23. R. W. Ziolkowski, "Properties of electromagnetic beams generated by ultrawide bandwidth pulse driven arrays," IEEE Trans. Antennas Propagat. **40**, 888-905 (1992).

24. R. W. Ziolkowski, "Localized transmission of electromagnetic energy," Phys. Rev. A **39**, 2005-2033 (1989).

25. R. W. Ziolkowski, "Localized wave physics and engineering," Phys. Rev. A **44**, 3960-3984 (1991).

26. E. Heyman and L. B. Felsen, "Propagating pulsed beam solutions by complex parameter substitution," IEEE Trans. Antennas Propagat. **34**, 1062-1065 (1986).

27. E. Heyman and B. Z. Steinberg, "Spectral analysis of complex source pulsed beams," J. Opt. Soc. Am A **4**, 473-480 (1987).

28. E. Heyman, B. Z. Steinberg and L. B. Felsen, "Spectral analysis of focus wave modes," J. Opt. Soc. Am A **4**, 2081-2091 (1987).

29. E. Heyman and L. B. Felsen, "Complex-source pulsed-beam fields," J. Opt. Soc. Am. A **6**, 806-817 (1989).

30. E. Heyman, "Focus wave modes: A dilemma with causality," IEEE Trans. Antennas and Propagat. **37**, 1604-1608 (1989).

31. E. Heyman, B. Z. Steinberg and R. Iancunescu, "Electromagnetic complex source pulsed beam fields," IEEE Trans. Antennas and Propagat. **38**, 957-963 (1990).

32. P. L. Overfelt, "Bessel-Gauss pulses," Phys. Rev. A **44**, 3941-3947 (1991).

33. P. L. Overfelt, "Generation of Bessel-Gauss pulse from a moving disk source distribution," J. Opt. Soc. Am. A **14**, 1087-1091 (1997).

34. H. Sõnajalg and P. Saari, "Suppression of temporal spread of ultrashort pulses in dispersive media by Bessel beam generators," Opt. Lett. **21**, 1162-1164 (1996).

35. H. Sõnajalg, M. Rastep and P. Saari, "Demonstration of the Bessel-X pulse propagating with strong lateral and longitudinal localization in a dispersive medium," Opt. Lett. **22**, 310-312 (1997).

36. P. Saari and K. Reivelt, "Evidence of X-shaped propagation-invariant localized light waves," Phys. Rev. Lett. **79**, 4135-4138 (1997).

37. A. Sezigner, "A general formulation of focus wave modes," J. Appl. Phys. **57**, 678-683 (1985).

38. R. W. Ziolkowski, "Exact solutions of the wave equation with complex source locations", J. Math. Phys. **26**, 861-863 (1985).

39. P. A. Belanger, "Packetlike solutions of the homogeneous wave equation," J. Opt. Soc. Am. A **1**, 723-724 (1984).

40. P. A. Belanger, "Lorentz transformation of the particlelike solutions of the homogeneous wave equation," J. Opt. Soc. Am. A **3**, 541-542 (1986).

41. P. Hillion, "Spinor focus wave modes," J. Math. Phys. **28**, 1743-1748 (1987).

42. P. Hillion, "Spinor fields with zero mass in unbounded isotropic media," Int. J. Theor. Phys. **27**, 57-71 (1988).

43. R. W. Ziolkowski, D. K. Lewis and B. D. Cook, "Experimental verification of the localized wave transmission effect," Phys. Rev. Lett. **62**, 147-150 (1989).

44. R. W. Ziolkowski and D. K. Lewis, "Verification of the localized wave transmission effect," J. Appl. Phys. **68**, 6083-6086 (1990).

45. A. M. Shaarawi, R. W. Ziolkowski, and I. M. Besieris, "On the evanescent fields and the causality of the focus wave modes," J. Math. Phys. **36**, 5565-5587 (1995).

46. A. M. Shaarawi, S. M. Sedky, R. W. Ziolkowski and I. M. Besieris, "The spatial distribution of the illumination of dynamic apertures and its effect on the decay rate of the radiated localized pulses," J. Phys. A: Math. Gen. **29**, 5157-5179 (1996).

47. A. M. Shaarawi, I. M. Besieris, R. W. Ziolkowski, and S. M. Sedky, "Generation of approximate focus wave mode pulses from wide-band dynamic Gaussian aperture," J. Opt. Soc. Am. A **12**, 1954-1964 (1995).

48. S. M. Sedky, *Generation of localized waves using dynamic apertures*, M.Sc. Thesis, Cairo University, Giza, Egypt (1995).

49. A. M. Shaarawi, S. M. Sedky, R. W. Ziolkowski and F. M. Taiel, "Effect of the switching pattern of the illumination of dynamic apertures on the ranges of the generated waves," J. Opt. Soc. am. A **13**, 1712-1718 (1996).

50. A. M. Shaarawi, S. M. Sedky, F. M. Taiel, R. W. Ziolkowski and I. M. Besieris, "Spectral analysis of time-limited pulsed Gaussian wavefields," J. Opt. Soc. Am. A **13**, 1817-1835 (1996).

51. S. M. Sedky, A. M. Shaarawi, F. M. Taiel and I. .M. Besieris, "On the diffraction length of localized waves generated by dynamic apertures," J. Opt. Soc. Am. A **13**, 1719-1727 (1996).

52. J. E. Hernandez, R. W. Ziolkowski and S. Parker, "Synthesis of the driving functions of an array for propagating localized waves," J. Acoust. Soc. Am. **92**, 550-562 (1992).

53. F. Gori, G. Guattari and C. Padovani, "Bessel-Gauss beams," Opt. Commun. **64**, 491-495 (1987).

54. I. Vicari, "Truncation of nondiffracting beams," Opt. Commun. **70**, 263-266 (1989).

55. M. Zahid and M. S. Zubairy, "Directionality of partially coherent Bessel-Gauss beams," Opt. Commun. **70**, 361-364 (1989).

56. P. L. Overfelt and C. S. Kenney, "Comparison of the propagation characteristics of Bessel, Bessel-Gauss and Gaussian beams diffracted by a circular aperture," J. Opt. Soc. Am. **8**, 732-745 (1991).

57. Z. L. Horvath, M. Erdelyi, G. Szabo, Zs. Bor, F. K. Tittel and J. R. Cavallaro, "Generation of nearly nondiffracting Bessel beams with a Fabry-Perot interferometer," J. Opt. Soc. Am. A **14**, 3009-3013 (1997).

58. A. J. Cox and D. C. Dibble, "Nondiffracting beams from a spatially filtered Fabry-Perot resonator," J. Opt. Soc. Am. A **9**, 282-286 (1992).

59. R. Armito, C. Saloma, T. Tanaka and S. Kawata, "Imaging properties of axicons in a scanning optical system," Appl. Opt. **31**, 6653-6657 (1992).

60. P. Vahimaa, V. Kettunen, M. Kuittinen, J. Turunen and A. T. Friberg, "Electromagnetic analysis of nonparaxial Bessel beams generated by diffractive axicons," J. Opt. Soc. Am. A **14**, 1817-1824 (1997).

61. J. Turnen, A. Vasara and A. T. Friberg, "Holographic generation of diffraction-free beams," Appl. Opt. **27**, 3959-3962 (1988).

62. A. J. Cox and D. C. Dibble, "Holographic reproduction of a diffraction-free beam," Appl. Opt. **30**, 1330-1332 (1991).

63. L. Niggel, T. Lanzl and M. Maier, "Properties of Bessel beams generated by periodic grating of circular symmetry," J. Opt. Soc. Am. A **14**, 27-33 (1997).

64. D. K. Hsu, F. J. Margetan and D. O. Thompson, "Bessel beam ultrasonic transducer: Fabrication method and experimental results," Appl. Phys. Lett. **55**, 2066-2068 (1989).

65. J. Y. Lu and J. F. Greenleaf, "Ultrasonic nondiffracting transducer for medical imaging," IEEE Trans. Ultrason. Ferroelec. Freq. Contr. **37**, 438-447 (1990).

66. J. Y. Lu and J. F. Greenleaf, "Nondiffracting X waves - exact solutions to free space scalar wave equation and their finite aperture realization," IEEE Trans. Ultrason. Ferroelec. Freq. Contr. **39**, 19-31 (1992).

67. J. Y. Lu and J. F. Greenleaf, "Experimental verification of nondiffracting X waves," IEEE Trans. Ultrason. Ferroelec. Freq. Contr. **39**, 441-446 (1992).

68. R. Donnelly, D. Power, G. Templeman and A Whalen, "Graphic simulation of superluminal acoustic localized wave pulses," IEEE Trans. Ultrason. Ferroelec. Freq. Contr. **41**, 7-12 (1994).

69. A. M. Attiya, *Transverse (TE) Electromagnetic X-waves: Propagation, Scattering, Diffraction and Generation Problems*, Ph. D. Thesis, Cairo University, May 2001.

70. J. Y. Lu, M. Fatemi and J. F. Greenleaf, "Pulsed-echo imaging with X wave," Acoust. Imag., P. Tortoli and L. Masotti, Eds., **22**, 191-196 (1996).

71. J. Y. Lu, H Zou and J. F. Greenleaf, "Biomedical beam forming," Ultrasound Med. Biol. **20**, 403-428 (1994).

72. J. Y. Lu, "Producing bowtie limited diffraction beams with synthetic array experiment," IEEE Trans. Ultrason. Ferroelec. Freq. Contr. **42**, 893-900 (1996).

73. J. Y. Lu, "Designing limited diffraction beams," IEEE Trans. Ultrason. Ferroelec. Freq. Contr. **44**, 181-193 (1997).

74. D. Power, R. Donnelly and R. MacIsaac, "Spherical scattering of superpositions of localized waves," Phys. Rev. E **48**, 1410-1417 (1993).

75. D. Mugnai, A. Ranfagni, and R. Ruggeri, "Observation of superluminal behaviors in wave propagation," Phys. Rev. Lett. **84**, 4830-4833 (2000).

76. A. M. Shaarawi, I. M. Besieris, A. M. Attiya and E. A. El-Diwany, "Acoustic X-Wave Reflection and Transmission at a Planar Interface: Spectral Analysis," J. Acoust. Soc. Am., vol. 107, pp. 70-86 (2000).

77. A. M. Attiya, E. A. El-Diwany, A. M. Shaarawi and I. M. Besieris, "Reflection and Transmission of X-waves in the Presence of Planarly Layered Media: The Pulsed Plane Wave Representation," Progress in Electromagnetics Research (PIER) **30**, pp. 191-211 (2000).

78. A. M. Shaarawi, I. M. Besieris, A. M. Attiya and E. A. El-Diwany, "Reflection and Transmission of an Electromagnetic X-wave Incident on a Planar Air-

dielectric Interface: Spectral Analysis," Progress in Electromagnetics Research (PIER) **30**, pp. 213-250 (2000).

79. A. M. Attiya, E. A. El-Diwany and A. M. Shaarawi, "Transmission and Reflection of TE Electromagnetic X-wave Normally Incident on a Lossy Dispersive Half-Space," Proceedings of the 17th National Radio Science Conference, NRSC'2000, Minufiya University, Egypt, pp. B11.1-12 (2000).

80. C. A. Balanis, *Advanced Engineering Electromagnetics*, John Wiley and Sons, New York, 1989.

81. H. C. van de Hulst, *Light Scattering by Small Particles*, Dover Publications, New York, 1981.

82. P. M. Morse, *Vibration and Sound*, McGraw Hill, New York, 1948.

83. A. M. Shaarawi, "Comparison of two localized wave fields generated from dynamic apertures", J. Opt. Soc. Am. A **14**, pp. 1804-1816 (1997).

84. G. b. Arfkin, *Mathematical Methods for Physicists*, Academic Press, San Diego, 1995.

85. M. Abramowitz and I. A. Stegun, *Handbook of Mathematical Functions*, Dover Publications, New York, 1965.

86. C. Kittel, *Introduction to Solid State Physics*, 7th edition, John Wiley, New York (1996).

87. H. Goldstein, *Classical Mechanics*, Addison-Wesley, Reading, Massachusetts (1981).